Study of Inclusive and Correlated Particle Production in Elementary Hadronic Interactions

Ph.D Thesis

Dezső Varga

Doctorate School of Physics
Head: Dr. Zalán Horváth

Particle Physics and Astronomy Program
Head: Dr. György Pócsik

Supervisor: Dr. György Vesztergombi

Department of Atomic Physics
Eötvös Loránd University
Budapest, July 2003.

Contents

1. Introduction

The subject of this thesis is the experimental study of elementary soft hadronic interactions. This field has been extensively studied over the last three decades, but due to the lack of clear theoretical understanding, the experimental efforts have turned from the soft sector (low momentum transfer processes) to the hard domain (high momentum transfer, where perturbation theory is applicable). On the other hand, the study of soft hadronic nucleus+nucleus collisions is still strongly evolving, initiated by the search for a QCD phase transition expected in the high density environment of heavy ion interactions.

The presented experimental work aims to provide *credible and precise* data, which besides adding to the large amount of existing measurements, contributes to the inclusive measurements with new results in terms of coverage, different projectiles and different targets. The studies also try to open up the way towards the *sub-inclusive level*, which could provide decisive new information both for comparisons with phenomenological models and for model-independent argumentations.

1.1 The theory of strong interactions: QCD

The Standard Model of particle physics includes Quantum Chromodynamics (QCD), the theory of strong interactions, which, to our current knowledge, correctly describes all hadronic processes. QCD has developed from the quark model of Gell-Mann and Zweig, when the concept of "color" quantum number has been introduced to solve simultaneously the difficulties related to the spin-statistics of baryons, the negative results of experimental searches for free quarks and the production rate of hadrons in e^+e^- annihilations. The existence of quarks has been confirmed by measurements of deep inelastic $e + p$ scattering, proving the presence of pointlike scattering centers inside the proton.

QCD is a quantum field theory with local gauge symmetry, ensuring the consistency (renormalizability) of the theory. The gauge group is color-SU(3). The interactions between the $q(x)$ fermion fields, called quarks, are mediated by the $A_\mu(x)$ vector fields of gluons. The quarks are in the triplet representation of SU(3), the gluons are in the adjoint octet representation. The Lagrangian can be written in the following form:

$$L_{\mathrm{QCD}} = -\frac{1}{2}\mathrm{Tr}G_{\mu\nu}G^{\mu\nu} + \sum_{j=1}^{n_f} \bar{q}_j(i\gamma^\mu D_\mu - m_j)q_j$$

where $A_\mu = A_\mu^a \frac{1}{2}\lambda^a$, with λ^a being the Gell-Mann matrices; $G_{\mu\nu} = \partial_\mu A_\nu - \partial_\nu A_\mu - ig[A_\mu, A_\nu]$ is the field strength tensor, $D_\mu = \partial_\mu - igA_\mu$ is the covariant derivative and n_f is the number of quark flavours. The coupling between quarks and gluons is hidden in the covariant

derivative with coupling constant g.

Up to now, exact solutions of QCD processes are not available. QCD calculations can be performed in a form of an expansion in powers of the coupling constant g, referred to as perturbative QCD (pQCD). The calculations lead to divergences, which have to be subtracted by renormalization. Renormalization theory suggests that the coupling constant, defined as the "strength" of the interaction vertex, depends on the momentum scale of the interaction (where the scale may be the typical momentum transfer). The calculation shows, that the dependence of the strong coupling constant $\alpha_s = g^2/4\pi$ on the μ momentum scale can be expressed as

$$\alpha_s(\mu) = \frac{4\pi}{(11 - \frac{2}{3}n_f)\ln(\mu^2/\Lambda^2_{QCD})}$$

in the first order of the perturbative expansion. Here Λ_{QCD} is the "strong interaction momentum scale", determined to be $\Lambda_{QCD} \approx 200$MeV from experimental study of pQCD processes; n_f is the number of fermion flavours. The equation shows the property of asymptotic freedom of QCD: at high momentum transfer, when $\mu \to \infty$, $\alpha_s \to 0$, ensuring the applicability of pQCD in this domain. On the other hand, at low momentum transfer, α_s diverges, which means that all the higher orders of the expansion become relevant, or in other words, non-perturbative effects will dominate the process.

The property of asymptotic freedom is a consequence of the non-Abelian structure of SU(3), in contrast to the U(1) symmetry of Quantum Electrodynamics. A further consequence is that the gluons interact with each other. Their contribution in the denominator of the expansion of $\alpha_s(\mu)$ appears with positive sign (11) and leads to asymptotic freedom. Confinement of color charges is qualitatively explained by the formation of a tube of color flux between the static sources: experimentally free quarks could not be observed, but only color-neutral bound states of quark pairs or triplets.

Historically, the perturbative and the non-perturbative domains are distinguished as "hard" and "soft" hadronic physics. In the soft domain, due to the lack of theoretical background, phenomenological models have been developed. The aim of these models is to pin down the relevant mechanisms active in the process, e.g. the reflection of valence quark structure, resonant excitation or parton (constituent quark or gluon) scattering.

Recent theoretical developments, improvement of numerical techniques and computing hardware allow non-perturbative QCD calculations to be performed on a space-time lattice. These calculations suggest that a QCD phase transition might occur at temperatures in the order of 200 MeV. The search for the predicted phase transition boosted the development in the field of Heavy Ion Physics.

1.2 Phenomenological models

The experimental study in the early 70-ies revealed the basic properties of soft hadronic interactions, which could not be explained by a simple generalization of QED. This can be summarized in a few "rules":

- At high energies, the total cross section of hadronic interactions weakly depends on energy, rather only slowly increases.
- The transverse momenta (p_T) of the produced particles are restricted: above the mean value of 0.3-0.6 GeV, the yield is damped exponentially.
- The mean multiplicity of hadronic collisions increases logarithmically with interaction energy.

The energy and transverse momentum dependence of particle production can be discussed within the framework of Regge theory. Regge theory predicts that the total cross section of a specific process behaves as $\sigma \propto s^{\alpha(t)-1}$ where $\alpha(t) = \alpha(0) + \alpha' t$ is the Regge trajectory with $\alpha(0)$ intercept. The increase of $\sigma(pp)$ with s means that the dominating exchanged particle, the Pomeron is described by $\alpha(0) > 1$. The observed p_T behavior is recovered by the t dependence of $\alpha(t)$. Regge theory describes the behavior of total cross sections and particle production in the diffractive region.

Before the QCD era and the appearance of parton models, further phenomenological models were introduced to explain the particle production in hadronic collisions; a review of these can be found in [6]. Multiperipheral models assumed that the particle production is dominated by a "ladder" graph of an effective field theory; this could explain the observation that pions are populating the central region of the collision such that the pion density is to first order flat in rapidity ("pionization"). The nova models started out with the assumption that the particles are produced by a subsequent decay of a resonance excited by the collision. The inputs of this model are the $\rho(M^2)$ nova excitation function and the mean q value of the decay (momentum of the emitted particles in the center of mass system of the resonance). $\rho(M^2)$ must behave to first order as $1/M^2$ to reproduce the observed proton spectrum in single-diffractive collisions. The versions which allowed resonance masses up to 4-5 GeV could grossly recover the measured proton and pion distributions.

The success of the parton model and hard QCD in deep inelastic scattering and high-p_T hadron production motivated the application of parton models for soft hadronic physics; an early review can be found in [7]. In deep inelastic scattering, the virtual photon scatters off a constituent (parton) of the proton: on the analogy of this, in the parton models, the basic process is the parton-parton interaction.

The parton models generally assume that the hadron+hadron interactions can be described in three steps. First, the colliding hadrons are resolved into their parton substructure, and yield the initial parton distribution. In the second step, gluon-exchange parton-parton interactions take place, which are assumed to be incoherent. The last step is the hadronization of both the strings (string fragmentation, e.g. corresponding to the fragmentation functions in $e^+ + e^-$) and the emerging partons. Some models may assume in addition final state interactions.

The models must explain the leading baryon effect, i.e. the observation that at high momentum the yield of baryons is higher than that of mesons. This motivated the postulation of a diquark within the hadron: the diquark has stiffer parton distribution, therefore it carries a large momentum fraction and also the baryon number of the initial hadron.

The phenomenological models have a number of free parameters, corresponding to each steps mentioned above, adjusted to fit the datasets relevant to the model.

Most of the recent models are available in the form of event generator codes, which simplifies the direct crosscheck of the experimental observations and predictions. In the course of this thesis, comparisons to the VENUS and the HIJING/B$\bar{\text{B}}$ models will be presented.

In the VENUS code [9], string fragmentation and hadronization proceeds such, that strings break up to substrings, and hadrons (or resonances) are created if the mass of the string decreases below a predefined limit.

The HIJING/B$\bar{\text{B}}$ Model [10] has recently included the "junction" mechanism [11], which relates the baryon number to a non-perturbative configuration of the gluon field within the baryon.

1.3 Experimental study of soft hadronic interactions

The bulk of the experimental information on soft hadronic interactions dates back to the seventies. This section gives a brief overview of the experimental efforts.

The bubble chambers have the advantage of full coverage for charged particles and low background, since the interaction vertex is directly visible. The principle of the bubble chamber is that a chain of bubbles emerges along the path of a particle, if the traversed liquid medium is overheated for a short period of time. The chamber is exposed to a beam of particles, which interact within the detector volume. From the photographs taken, the multiplicity and the momenta of the produced particles are reconstructed. Particle identification is restricted to low momentum protons via the high bubble density on the track due to higher ionization. On the other hand, particles decaying via the weak interaction (Λ^0,K^0_S) can be identified and measured by the displaced secondary vertex of the decay. Bubble chambers were operated at lower energies (12-24 GeV) [1] at CERN, and at higher

energies between 70-200 GeV at NAL [2] and Serpukhov [3]. The further evolution went towards the high statistics, large chambers and "hybrid" systems with external identification, but in parallel with the loss of (theoretical) interest towards soft physics, the research turned in the direction of "rare" phenomena, neutrino and charm physics.

Counter experiments were operating with electronic detectors, trigger system and data acquisition. The tracks of the produced particles were reconstructed from hits in wire chambers (e.g. drift chambers), whereas particle identification was achieved with Cherenkov counters.

The small aperture single or double arm devices could perform inclusive measurements. The point-by-point setting of the spectrometer arms had the disadvantage of varying systematic error sources. Fixed target experiments at CERN and Fermilab operated at 100-400 GeV beam energy ($\sqrt{s}$=14..27 GeV). Collider experiments at CERN ISR [4] reached up to $\sqrt{s}$=63 GeV.

The large aperture electronic devices (Omega, SFM, EHS) were approaching the bubble chambers in terms of coverage, but have never collected a high statistics sample in the minimum bias regime: the largest sample of 400k event in p+p was taken by EHS[1] (European Hybrid Spectrometer [5]). This should be seen in contrast to e.g. LEP, where 16 M events of hadronic final states on the Z^0 peak were collected, completely unparalleled in hadronic reactions.

Colliders in the TeV range were devoted to hard processes, which became the basis of the success of perturbative QCD and the Electroweak Theory. The research in the soft sector was restricted to diffractive phenomena.

Generally the experimental status of soft hadronic physics is rather unsatisfactory: the existing inclusive datasets are mostly incomplete and insufficient for detailed argumentations. The field is "abandoned": the recent experimental efforts are dominated by research of A+A interactions. The present thesis aims to improve on this misbalanced situation.

1.4 Nuclear interactions and Heavy Ion Physics

Experimental studies of nuclear interactions (see e.g. [12]) have revealed basic systematic features and differences compared to elementary processes in h+A collisions. The baryon stopping phenomena [13], which is the decrease of the mean baryon momentum on the projectile side, is of special interest within the framework of this thesis. A rich phenomenology of nuclear collisions have been developed (see e.g. [7]) to account for these differences.

The straightforward generalizations of the parton models to nuclear interactions sig-

[1]It is interesting to note that EHS included a small, rapid cycle bubble chamber as a vertex detector.

nificantly underestimates the baryon stopping and strangeness production. Recent phenomenological models had to include additional mechanisms to improve the description of the measurements.

In the VENUS Model [9], the interaction between strings is invoked, which is relevant for nuclear collisions. In case of the junction picture within the HIJING/B$\bar{\text{B}}$, the Lorentz-contracted nucleus can be viewed as a "gluon filter", holding back the junction, while the valence quarks fly through: this generates higher baryon stopping.

Over the past two decades, the general loss of interest towards soft hadronic physics held back the research in the field of h+A interactions, but on the other hand, the field of nucleus-nucleus interactions has been strongly evolving, motivated by the search for a possible QCD phase transition.

QCD at high temperature and density may be studied in heavy ion collisions. A series of dedicated machines came into operation: starting from AGS at Brookhaven ($\sqrt{s}$ = 3 to 5 GeV) and the CERN SPS accelerator ($\sqrt{s}$ = 6 to 20 GeV), very high energy collisions are studied currently at RHIC in Brookhaven (up to $\sqrt{s}$ = 200 GeV). Further facilities are in preparation, the ALICE detector at CERN LHC operating in the TeV range and the High Intensity Ion Beam Complex at GSI Darmstadt, which aims to reach very high baryon density at reduced energies.

Lattice QCD calculations suggest that besides the ordinary phase of hadron gas, where quarks are confined into normal massive hadrons, a different phase could exist, the so called "quark-gluon-plasma" (QGP). In this phase quarks and gluons are deconfined and chiral symmetry is restored. Recent calculation with $n_f = 2 + 1$ dynamical staggered quarks [14] on a lattice of $L_t = 4$ determined the phase diagram of QCD in the temperature – bariochemical potential (T – μ_B) plane, shown in Figure 1.

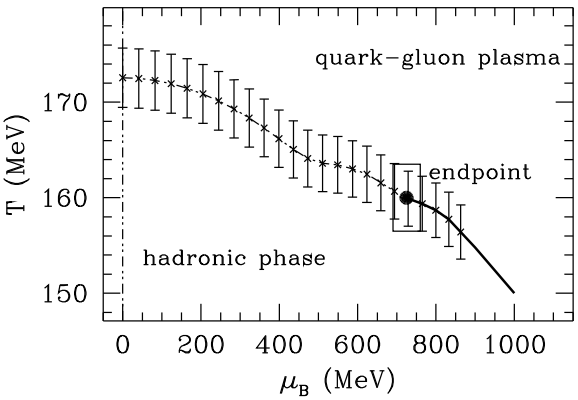

Figure 1: Phase diagram of QCD from [14]

According to this result, a first order phase transition is predicted at high μ_B (corresponding to baryon density) and finite T, and a crossover-type transition at small μ_B and finite T. This means that the endpoint of the phase transition is a critical point, where a second order phase transition takes place. The qualitative features of the phase diagram is crucial from the point of view of experimental search for QGP.

Experimentally, the second order phase transition would provide an unambiguous signature: the region of the critical point is characterized by fluctuations of long wavelength, leading to fluctuations on the level of the observable final state hadrons. On the other hand, if the critical point is missed from the low μ_B side, the smooth crossover transition may suppress the observable signatures.

Further signatures were predicted [15] to prove the creation of the QGP phase:

- Strangeness enhancement: in the QGP, the threshold of strange quark production reduces compared to normal hadron gas, which enhances the yield in a thermalized system.

- J/ψ suppression: the $c\bar{c}$ bound state created in the deconfined QGP phase has a high probability of breaking up and turning up as D mesons after hadronization, which leads to the suppression of charmonium yield.

- Jet quenching: recent measurements at RHIC [16] [17] have shown that the high-p_T meson production in Au+Au collisions is strongly suppressed compared to p+p interactions, which means that the jets may lose (radiate) a considerable fraction of their energy while passing through the matter created in the nuclear collision.

The interpretation of all these signatures has to rely on comparisons to elementary interactions, which suggests that the experimental investigation of elementary interactions is mandatory. At the same time, the model dependence of the comparison has to be reduced, which can be achieved by the test of the models through the widest possible range of hadronic interactions.

The natural scheme for the progress of the studies seems to be the sequence h+p $\rightarrow$ h+A $\rightarrow$ A+A interactions, where the hadron+nucleus interactions play the role of experimental link between the elementary and the complex nuclear reactions: p+A interactions can reveal nuclear effects without the expected thermalization of A+A collisions. The results of this thesis are expected to contribute to the understanding of this experimental link.

1.5 Experimental possibilities of NA49

The NA49 Experiment is a large acceptance hadron detector, which has the chance to study the experimental questions addressed in the previous sections. The features of the experiment providing decisive gain over the previous detectors can be summarized as follows.

- *Wide range of studied reaction types.* Measurements are available with different projectiles (p, π, n) on different targets (proton and nuclei) to get hold of the dependence

on the valence quark structure and isospin of the projectile and to see the evolution with the complexity of the system.

- *Large acceptance.* The detector has continuous coverage of nearly the complete forward hemisphere, which is needed to get a global and detailed view of the inclusive distributions. The charged particle tracking is completed with neutral particle detection. The large acceptance is especially important for correlation studies.

- *Particle identification.* For charged particles, identification is available, which is again of key importance both for inclusive and correlation measurements.

- *High statistics.* The Experiment has collected more than 20 M events in elementary and nuclear collisions, which is a unique data sample in soft hadronic physics. Some examples of event numbers of the available datasets which are relevant to the thesis, are given in the following tables[2]:

p + p	5.8 M
$\pi^{\pm}$ + p	1.6 M
n + p	0.3 M

p + Pb	3.8 M
$\pi^{\pm}$ + Pb	1.4 M
Pb + Pb	5 M

1.6 Objectives of the presented studies

The study, which concentrates on *elementary interactions*, may be regarded as a part of a long term physics project pursued at the NA49 Experiment. This section gives a brief overview of the objectives of the present thesis.

The motivation of the thesis is twofold.

- The interpretation of possible new phenomena in heavy ion collisions relies on comparisons with elementary interactions, therefore the experimental study of the latter is mandatory at a comparable quality as the former. This also includes constraining the phenomenological models which are applied to make predictions from elementary interactions.

- Improvements of the experimental techniques over the last decades allow the detailed study of elementary interactions with high quality and statistical accuracy, over a large kinematical range and with particle identification. To date, the number of mutually contradicting phenomenological models describe the gross inclusive features of the datasets: even if these models can be tuned to fit the precise results, detailed

[2]Only the data taken with 158 GeV beam is shown

measurements on the sub-inclusive level can provide a wide range of tests and hope to falsify some of the model classes.

In order to ensure the reliability and precision of the results, considerable effort has to be devoted to the development of data extraction, calibration and normalization. The control over the systematic errors is of key importance, therefore the internal consistency of the data must be checked whenever possible.

Besides the inclusive measurements, the study of internal correlations of elementary collisions is aimed at finding regularities which could shed more light on the particle production mechanisms and constrain possible phenomenological descriptions.

The discussions of the previous sections motivated the establishment of links between the elementary and complex interactions involving nuclei.

In the course of this thesis, the above mentioned objectives will be exemplified on two levels. Baryon number transfer in elementary interactions is studied, suggesting a factorizing two component picture of baryon number transfer, one of them connected to the target, the other one to the projectile. Independent evidences are found supporting the arguments, both from inclusive measurements and correlations. The study of internal correlations in elementary interactions involving pions leads to a model-independent prediction for the observed pion density in nucleus-nucleus collisions, assuming that nucleus-nucleus collisions can be approached with weighted superposition of elementary interactions.

1.7 Outline of the thesis

This thesis presents an experimental study of elementary collisions with an outlook on possible model independent predictions for nuclear collisions.

Chapter 2. gives a brief description of the NA49 experiment.

The detection and identification of charged particles in the TPC (Time Projection Chamber) system is discussed in Chapter 3.

Chapter 4. describes the measurement of neutron production with the Ring Calorimeter of the experiment.

Chapter 5. presents the construction of a new additional TPC, and the forward proton detection with this device is discussed in Chapter 6.

In Chapter 7. the absolute normalization and the necessary corrections are described which lead to the final results on particle yields.

The results are presented in the last two Chapters, discussing the results on particle spectra and correlations in elementary collisions.

Finally, two important technical issues are described in detail in Appendix 1. and 2.

2. Description of the NA49 detector

2.1 Overview

The NA49 Experiment is a large acceptance hadron detector [18], for the study of elementary and nuclear interactions. The NA49 is located in the North Experimental Area of the SPS accelerator (Super Proton Synchrotron) at CERN (European Organization for Nuclear Research). The basic motivation of the construction was the experimental investigation of high energy nucleus+nucleus (A+A) collisions, since in the energy range of the SPS (158 GeV/nucleon Pb beam), the transition of the hadronic matter to the Quark Gluon Plasma phase was expected to occur. The detector setup is optimized for the study of event-by-event fluctuations, which characterize the second order phase transition.

Over the years, the scope of the experimental program widened up, and besides the p+p, p+Pb and Pb+Pb interactions, it included interactions of different nuclei (C+C, Si+Si), elementary collisions with various beams ($\pi^{\pm}$, n) and the energy dependence of observables in nuclear collisions.

In this chapter, the NA49 detector will be described, with emphasis on those components that are relevant to the present thesis. The detector is built around a large acceptance magnetic spectrometer, with particle tracking and identification in a set of Time Projection Chambers (TPC-s). The system is completed by calorimeters and Time of Flight (ToF) detectors. The outline of the Experiment is shown in Figure 2.

The beam enters from the left of the Figure, and after passing through beam counters, falls on a target (marked with a large X). The actual target and trigger setup is different for A+A, h+p and h+A interactions (inserts marked with a, b and c). The emerging particles are deflected by two magnets (Vertex Magnets, VTX-1 and VTX-2). The particle trajectories are recorded in the four TPC-s: two Vertex-TPC (VTPC-1 and VTPC-2) and the two Main TPC-s (MTPC-L and MTPC-R). The ToF walls are placed behind the TPC system. The forward particles or fragments are detected in the Veto Chambers (VPC) and the calorimeters (RCal and VCal).

The center of the NA49 coordinate system is in the middle of VTPC-2, with the z axis pointing downstream in the beam direction (therefore, the target is at about z=-581 cm). The positive x direction points horizontally to the left (upwards in Figure 2, towards the MTPC-L side).

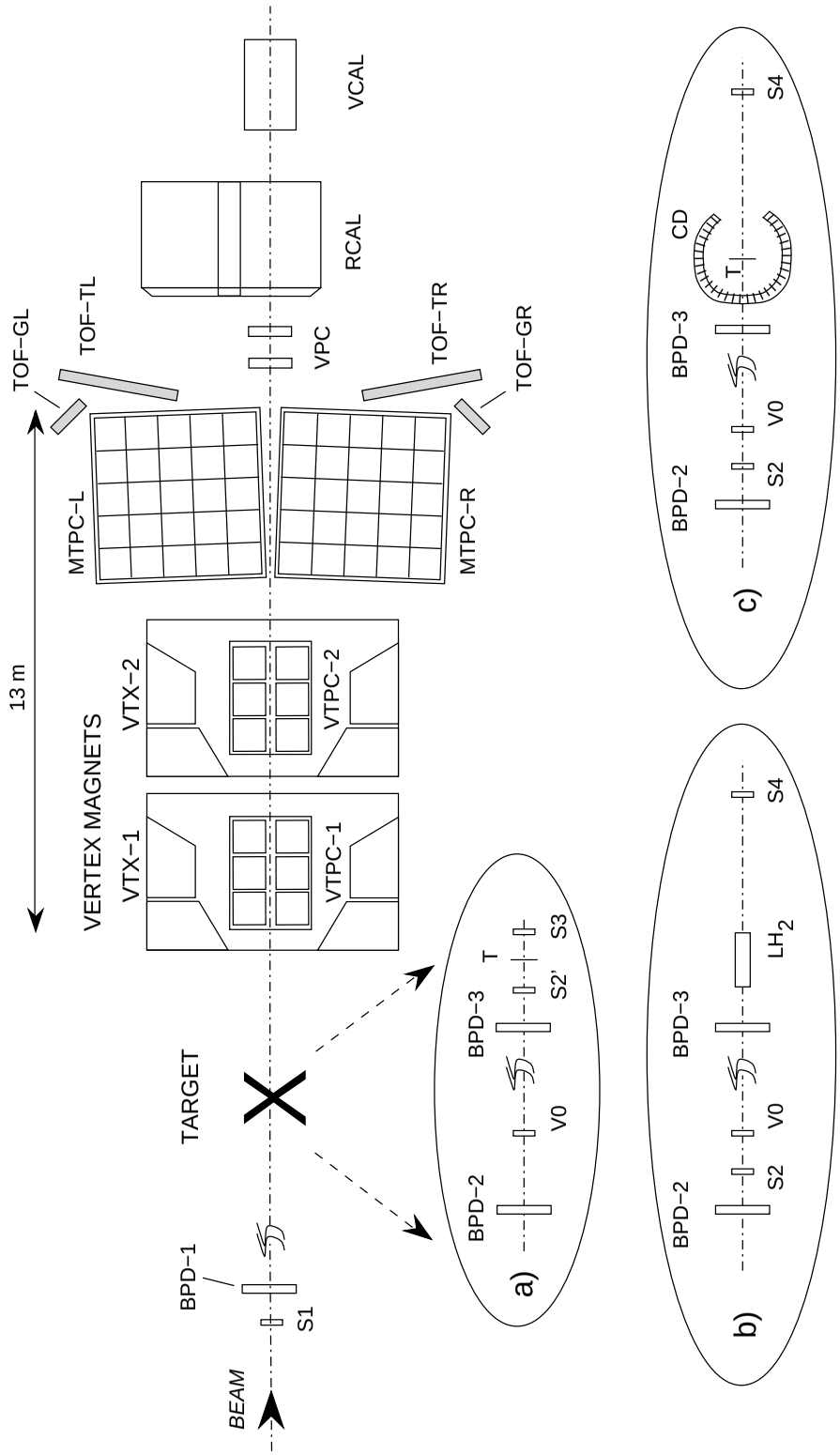

Figure 2: Layout of the NA49 detector system

2.2 Beam counters and Beam Position Detectors

The incident particle beam originates from the SPS, which in case of Pb beam arrives directly from the accelerator to the experiment; in the other cases, including hadron beams and nuclear fragments, a secondary beam is created on a production target far upstream. The secondary beam contains a mixture of particle types. The purpose of the beam counters is to tag the presence of the valid beam particle and to provide a precise timing information.

The S1 counter is placed 34 m upstream from the target. This counter defines the timing of the experiment. For proton beam, the 5 mm thick scintillator is equipped with four photomultipliers to improve the time resolution; for Pb beam, the scintillator is replaced by a thin quartz wafer.

The S2 is a 2 mm thick scintillator, 10 m upstream from the target. For Pb beam, it is replaced by a helium Cherenkov counter, S2'.

A threshold-Cherenkov counter (CEDAR) is applied to select the required particle type in case of secondary hadron beams.

The beam definition is completed by V0, a scintillator with a hole in the middle, required to be in anticoincidence with S1, S2 and the CEDAR. This counter eliminates upstream interactions. The V0 is located close to S2.

The Beam Position Detectors (BPD-s) are small, 3×3 cm proportional chambers with cathode strip readout, which measure the position of the beam particle in the transverse plane. The three counters are placed 33, 11 and 1 m upstream from the target (in the NA49 coordinate system, at z=-3879, -1647 and -689 cm; BPD-3 is the closest). The position resolution is 170 μm for proton beam (40 μm for Pb beam). The BPD-s are discussed in further details in connection with the normalization scheme.

2.3 Target setup

The interaction target may be proton or various nuclei. The proton target is liquid hydrogen, contained in a Mylar cylinder of 3 cm diameter and 20 cm length. The container sits in vacuum for heat insulation. During the design, special care was taken to minimize the material that the produced particles have to cross. The container is as thin as 50 μm, the outer window holding the vacuum is 100 μm. For h+Pb interactions, the target is a lead foil, surrounded by the Centrality Detector (CD). The CD consists of a set of proportional tubes with segmented cathode readout of altogether 256 independent elements. The device is designed to detect the number of "grey protons", knock-on nucleons in the laboratory momentum range of 0.15 to 1.2 GeV, the number of which is correlated to the centrality of the h+Pb collision (a recent review can be found in [19]). The output signal is discriminated:

the higher cutoff of the desired momentum range is adjusted by requiring high ionization of the slow grey proton, which progressively eliminates the protons above about 0.8 GeV, whereas the lower cutoff is ensured by an absorbing copper foil of 200 μm in front of the proportional tubes. For Pb beam, the Pb target is again a thin foil, in a setup adopted for the trigger system.

All the target systems mentioned above offer the possibility to measure in "empty target" mode, when all the support structure is intact, only the target is removed from the beam (or the liquid hydrogen is emptied from the container). Data taken in this mode allows the measurement of the background from interactions outside the target volume. The related issues are discussed in Appendix 1.

2.4 Trigger system

The purpose of the trigger system is to tag the events in which the beam particle interacted and eventually select the events of a desirable centrality. The term "minimum bias" stands for the weakest possible condition.

In hadron beams, e.g. p+p, π+p or minimum bias p+Pb, a small cylindrical counter (S4) is placed 4 m downstream from the target between the two vertex magnets, centered on the beam. The interacted beam particle has a high probability to miss this 2 cm diameter scintillator, therefore the trigger condition is the requirement of a valid incoming beam and no hit in S4.

In case of hadron+nucleus interactions, the Centrality Detector offers the possibility of on-line triggering on the number of hits to enrich the high centrality p+A sample.

The centrality of nucleus+nucleus interactions is controlled by the zero-degree (Veto-) calorimeter (VCal), 20 m downstream from the target. The detector measures the energy of the nuclear fragments from the interacting Pb ion; the higher centrality is characterized by less of these fragments and therefore lower energy deposit in the VCal.

A trigger setup was proposed to select proton spectators in d+p interactions [20] in order to perform a high statistics n+p measurement. The system is forseen to be used for the first time in the autumn running period of 2003.

2.5 Magnets

The momenta of the produced particles are measured from the deflection of the trajectories in the magnetic field. NA49 has two superconducting magnets (Vertex 1 and 2), with 1.5 and 1.1 Tesla field. The high overall bending power of 9 Tm is needed to gain acceptance in the forward region, but at the same time the high field allows precise momentum determination

up to the kinematic limit in p+p interactions.

The time stability of the magnetic field is controlled over the run periods with Hall probes. The field is not homogeneous: a field map is available in the reconstruction software, from the combination of a detailed measurement and numerical calculations.

The Vertex TPC-s are placed inside the aperture of the magnets with the advantage that the curvature of the track is directly measurable. The Main TPC-s are outside the magnetic field.

2.6 The TPC (Time Projection Chamber) system

2.6.1 Overview

The charged particles produced in hadronic interactions are measured and identified in the TPC system of NA49. Figure 3 gives an example of a p+p event, where the dots are the measured spacepoints, the continuous lines are the fitted tracks.

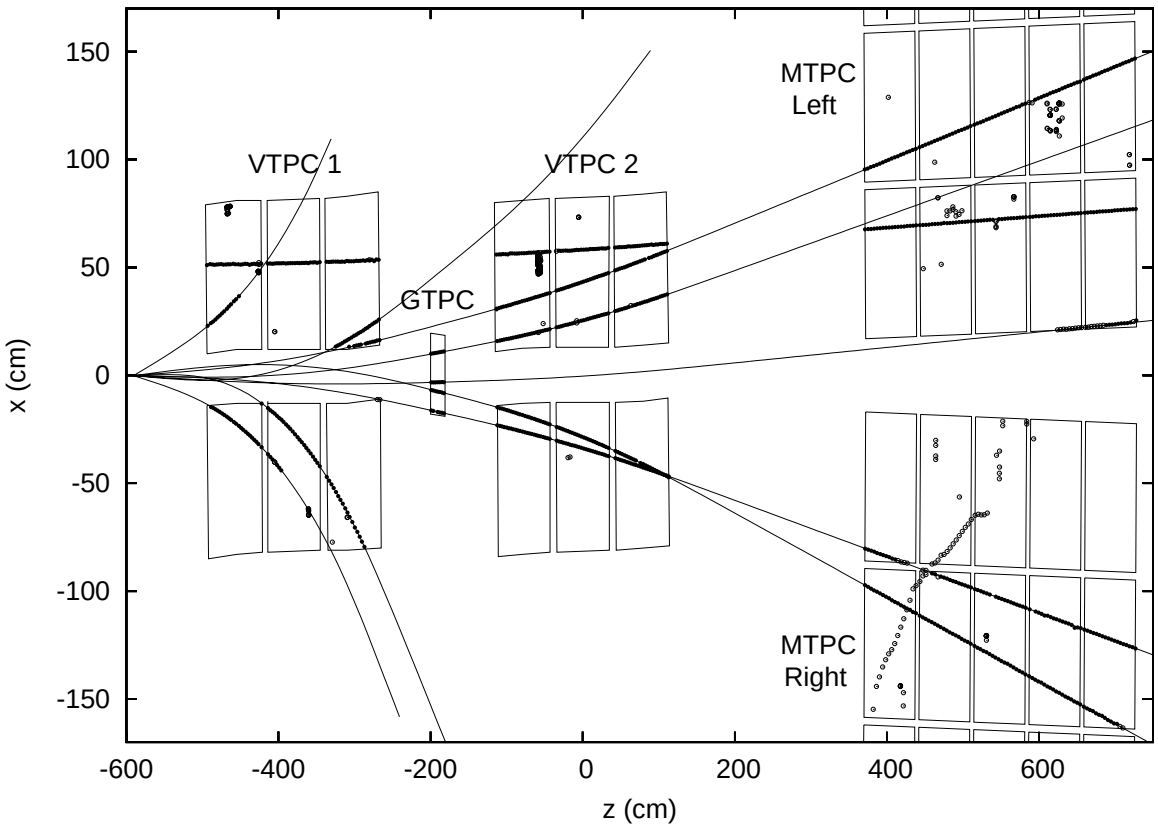

Figure 3: Two dimensional projection of an event, including the Gap-TPC. Note the enlarged scale in x (horizontal) compared to z (longitudinal) direction.

The NA49 TPC-s are designed to cope with the high multiplicity (up to 2000 detected particles) and track density of the Pb+Pb environment. The gas choice, electronic response and readout structure is optimized to achieve a good two-track resolution. The other major concern was the particle identification by ionization measurement, which requires track length of several meters. The NA49 experiment has huge TPC-s: the total sensitive volume of the detector system is more than 45m^3.

The stable performance of the system requires temperature control, gas monitoring and precise detector alignment. The temperature is kept stable to a precision of $\pm 0.1^oC$ within the air conditioned huts housing the TPC-s, and monitored continuously with 60 sensors. The gas system is responsible for the purity and stability of the gas composition within the chamber volumes, which is Ne/CO_2 (90/10) in the VTPC-s and $Ar/CH_4/CO_2$ (90/5/5) in the MTPC-s, with oxygen content on the level of 2-4 ppm.

The detector alignment is determined by a number of independent ways which are shown to be consistent. The external optical survey provides a precision better than 0.2 mm in relation to the SPS beam coordinates. In the configuration with magnetic field off, straight tracks of muons from the beam halo or particle tracks from interactions are used to adjust the TPC-s with respect to each other.

The Pb ion beam is highly ionizing (6×10^3 times the minimum), therefore a gap had to be formed in the TPC volume along the beam path. For this reason the two Main TPC-s are pulled apart; in the VTPC-s, separate field cages are constructed for the two (horizontal) halves. This gap has several disadvantages: besides the difficulties at detecting neutral weak decays for which the secondary vertex is outside the sensitive volume, the acceptance for fast particles is also limited. In case of proton beam, the beam could pass through a chamber volume: in 2001, the TPC system has been completed with the Gap-TPC (GTPC) placed between the two VTPC-s. The GTPC extends the acceptance considerably and improves the primary vertex determination. The author contributed to the mechanical construction and the reconstruction software, and performed the physics analysis, therefore these issues will be discussed in more detail in Chapter 5. and 6.

2.6.2 The operation of the TPC

The principle of the TPC operation and the basic structure is shown in Figure 4. The detector consists of two main parts: the sensitive volume and the readout chamber.

The particles pass through the sensitive volume and create clouds of ionization electrons along their trajectories. Inside the sensitive volume, a homogeneous electric field is built up (in the order of 150-200 V/cm) by the High Voltage Plate and the Field Cage. This latter structure is a set of conducting strips stretched around the side walls of the gas volume, and

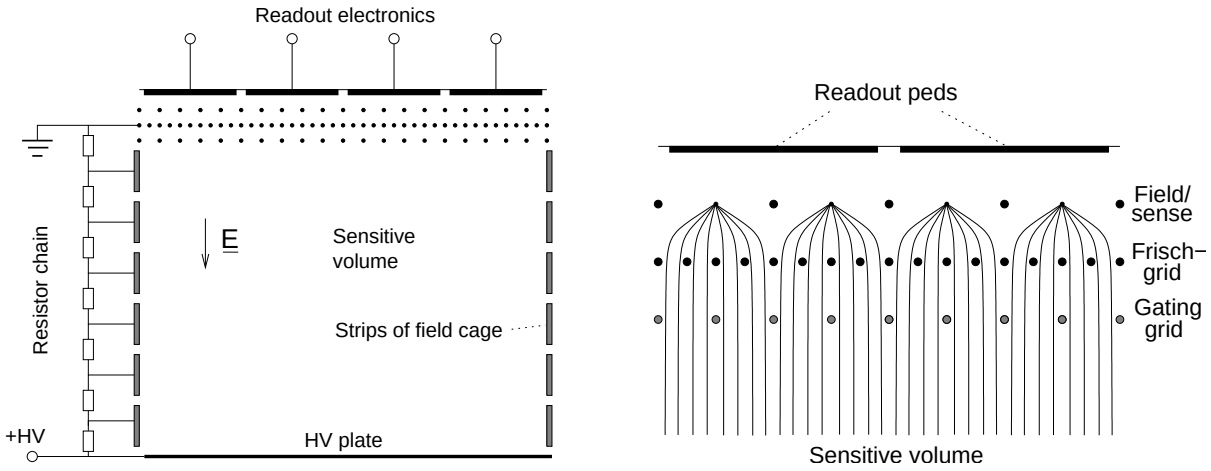

Figure 4: Structure of the TPC; the general layout is shown on the left. The ionization electrons drift through the sensitive volume and reach the readout chamber on the top. On the right panel, details of the readout chamber are shown. The continuous lines represent the field lines along which the electrons drift.

a voltage divider chain ensures the constant gradient of the potential. The electrons drift through the volume in the electric field and reach the readout chamber.

The readout chamber is constructed from layers of wires. The electrons first drift through the gating grid and the Frisch grid, the latter defining the ground potential of the drift volume. The gas multiplication takes place close to the thin (20μm diameter) sense wires in the third wire layer, which are connected to a high positive potential. The field wires in this layer are on ground. The sense wires are capacitively coupled to the pads from which the signal is read out.

The pads cover the two dimensional horizontal surface of the top plate of the chamber. The drift velocity of the electrons is precisely controlled, therefore the arrival time of the electric pulse measures the position in the vertical direction. The pads are 4-6 mm wide, 1.5-4 cm long. The drift velocity inside the TPC-s varies from 1.5 to 2.4 cm/μs. The particle tracks are measured with a precision of a few hundred μm.

The pads are organized in rows (padrows) in the x direction; these padrows are closely perpendicular to the beam. The number of detected points is determined by the number of the padrows that the track crosses; this amounts to a maximum of 72 in each VTPC-s and 90 in the MTPC.

2.6.3 Readout and Data Acquisition (DAQ)

The TPC can be regarded as a detector which records the three dimensional image of the particle trajectory by providing the digitized amplitude of the deposited ionization charge on a three dimensional grid. In the NA49 experiment, this corresponds to nearly 10^8 8-bit numbers for every recorded event. In order to handle this huge data output, a progressive sequence of data reduction is realized by the Data Acquisition system and the reconstruction software.

The signal is picked up by the front-end cards, mounted directly on the readout chambers to minimize the electronic noise. After amplification and shaping, the signal is digitized. For each pad, the time structure of the signal is sampled in 512 time buckets and therefore recovers the timing information needed to determine the vertical position of the track. The digital information arrives to the Control- and Transfer (CT) boards, which transfer the information from the readout chamber to the control room via an optical fiber link (768 channels are multiplexed onto one fiber).

The VME-based receiver boards perform noise rejection and zero suppression by rejecting the digitized numbers falling below a predefined threshold. This way the data is compressed from 100 Mbyte per event to about 8 Mb for a central Pb+Pb collision (1-1.5 Mb for p+p interaction). The data is then transferred to the central DAQ to be recorded on Raw Data Tapes.

Most of the recorded data volume originates from the TPC system, therefore the data taking speed is determined by the data recording and processing speed of the TPC readout. The DAQ is optimized for the SPS spill of 2.4-4 seconds in 14-16 s cycles. In one spill, 20-33 events are recorded, which correspond to more than a million recorded events in a week.

2.6.4 Track reconstruction

In the reconstruction phase, the raw data is analyzed with a dedicated software chain, resulting in measured tracks. The reconstruction software of NA49 is a complicated system, which evolved over ten years. The main steps are the following:

- Cluster finding. The ionization charge, even if it is deposited by a pointlike source, will be smeared due to diffusion and detector response. This means that the points of the particle track will appear as a cluster of high ADC values. These clusters are identified, the geometrical center and the total charge is determined, resulting in measured space points.

- Distortion correction. In the presence of inhomogeneous magnetic field, the diffusion of electrons does not follow the electric field, therefore the measured trajectory will be

distorted. The distortion can reach several cm in certain corners, which is corrected out.

- Local tracking. The space points found by the cluster finder algorithm are linked up to form track pieces within the detector unit.
- Global tracking. Track pieces from the same particle in different detectors (e.g. VTPC2 and MTPC, or VTPC1 and VTPC2) are merged together, to form a global track.
- Main vertex finding. A dedicated algorithm searches for the most probable location of the primary interaction (Main vertex). The closest approach of the tracks are searched for, sequentially rejecting the outlier tracks (which are mostly from background, partially from weak decays).
- Search for weakly decaying particles.
- Momentum fitting. With the constraint that the tracks are originating from the Main vertex, the track trajectories are fitted and their momenta are determined. Tracks which are inconsistent with the Main Vertex assumption are rejected.

The output of the reconstruction software is written to Data Summary Tapes. The reconstruction usually takes a couple of weeks on a computer farm for a complete run period.

2.6.5 Acceptance and efficiency

The geometrical acceptance of the detector for charged particles is shown in Figure 5, where the black shading corresponds to 100% accpetance and the white shading is of no acceptance. The acceptance of the original setup (shown in the left panel) is weak above 100 GeV momentum. The inclusion of the Gap-TPC increases the acceptance decisively in this forward region, as it is demonstrated on the right panel of Figure 5.

The tracking efficiency is estimated from a combination of eyescan studies and Monte-Carlo simulation of the detector. The eyescans of event displays have shown that the detection inefficiency is below the percent level for track elements with a minimum of about 8 points. Inefficiencies may arise in the high track density of PbPb interactions, when the close-by tracks overlap: the losses, which depend on the cuts of the track selection, are estimated from detector simulation. In case of p+p, p+A or nucleus-nucleus interactions of small nuclei, these losses are negligible.

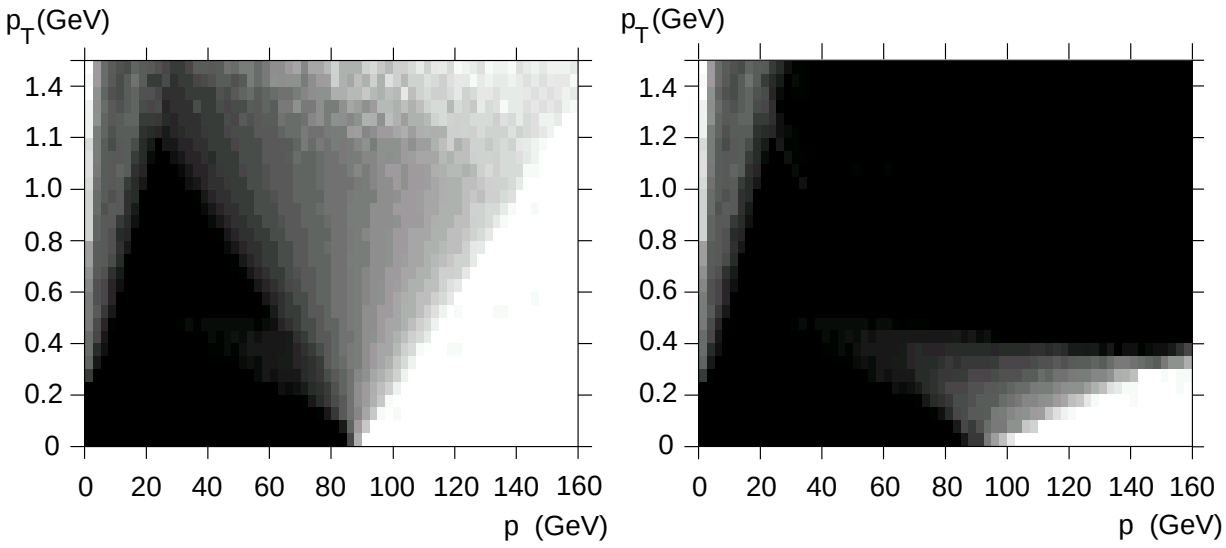

Figure 5: The acceptance of the TPC system. The original setup shown on the left, the extended acceptance with GTPC+VPC tracks on the right.

2.7 Time of Flight detectors

The particle identification capabilities of NA49 are completed with Time of Flight (ToF) detectors, in the range of 2-10 GeV: even though the dE/dx can be used down to 3 GeV for pion identification, protons and kaons can not be separated below 4.5 GeV. The time resolution of the ToF system is in the order of 70 ps, which allows the separation of protons from kaons and pions for the complete range of acceptance. Two detectors are installed behind each MTPC-s: a pixel scintillator system (marked with TOF-TL and TOF-TR in Figure 2) and a grid scintillator system (TOF-GL and TOF-GR). The grid ToF system was designed and built by the Budapest Group of the NA49 Experiment; for further details see [21] [22]. The ToF walls cover a total of 5.6 m^2 surface, and detect approximately 7% of all the produced charged particles.

2.8 The Ring Calorimeter and the Veto Chambers

The Ring Calorimeter (RCal) [23] is far downstream, 20 m from the target. This is probably the oldest component of the detector, constructed more than 25 years ago [24]. Originally it was designed for the NA5 experiment to measure hadron jets [25], later inherited by the NA35 Collaboration, and subsequently used for E_T measurements in Pb+Pb interactions [26].

The RCal is a barrel shaped sampling calorimeter with two parts (sections): in the front

the photon part which measures the energy of electromagnetic particles, and the hadron part behind. The outer diameter of the detector is 3 m, the inner diameter is 60 cm. In the original setup, it was used without spectrometer magnets in a symmetric position so that the beam passed through the center.

Starting from 1999, the Calorimeter found its new application, which is neutron detection in p+p and p+A interactions, where the low multiplicity allows the single particle detection. It was displaced to an asymmetric position (see figure 2) to cover the area of the highest neutron density around the beamline.

The neutron detection requires the tagging of neutral particles which initiate the energy deposit. Since the fast charged particles escape through the gap between the MTPC-s, a veto counter had to be designed to cover this area: the two Veto Proportional Chamber (VPC) walls. These are classical proportional chambers with cathode-strip readout, placed in front of the Calorimeter. With their width of 80 cm and height of 160 cm they close the gap and ensure the hermeticity of the detector.

The performance of the Ring Calorimeter and the Veto Chambers will be discussed in connection with the measurement of neutron production in Chapter 4.

With the inclusion of the GTPC, the precise momentum determination of the fast forward tracks became possible through the combination of the GTPC and VPC information. The procedure will be presented in Chapter 6.

3. Particle identification with the TPC system

3.1 Particle identification via the specific ionization

The ionization of the particles at a given momentum depends on the particle mass. This effect can be used to identify particles, since the ionization is measured in the TPC system. The dependence of the ionization on the momentum of the particle (called the *Bethe-Bloch function*) is known only approximately; a possible parametrization is given by:

$$\frac{\mathrm{d}E}{\mathrm{d}x} = B(\beta\gamma) = \frac{2\pi N e^4}{m_e c^2 \beta^2}\left(\ln\frac{2m_e c^2\beta^2\gamma^2 E_{\max}}{I} - 2\beta^2 - \delta(\beta)\right)$$

where N is the electron density of the material, m_e is the electron mass, I is the average ionization energy, $E_{\max}$ is the maximum energy transfer in the ionization process, and β is the velocity of the particle. The function $\delta(\beta)$ describes the shadowing effect of the polarization in the material. It is important to note that the ionization is a function of only the particle velocity, or the momentum/mass ratio ($\beta\gamma$).

The Bethe-Bloch function for different particles is shown in Figure 6. The general feature is that the ionization decreases as $1/\beta^2$ at low momentum, then after reaching a minimum, keeps rising ("relativistic rise") up to the saturation region ("plateau").

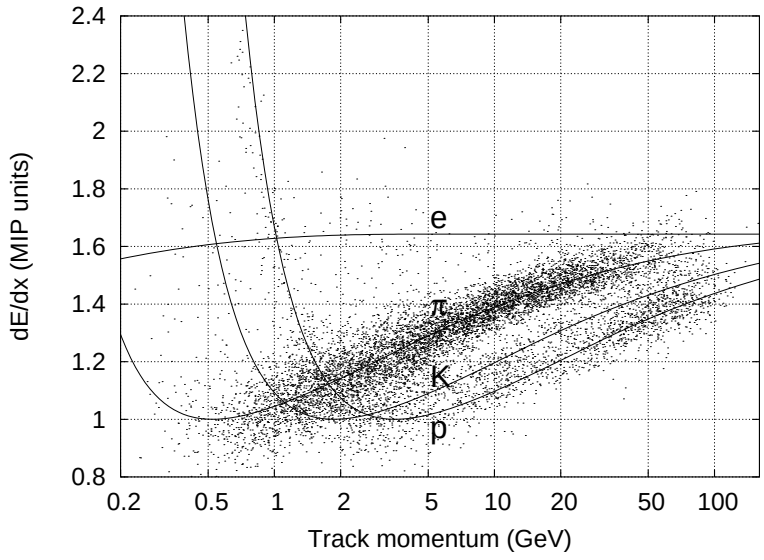

Figure 6: Bethe-Bloch curves: ionization as a function of momentum. The ionization is measured relative to the minimum ionizing particle (MIP).

The ionization of a particle is determined from the measured charge deposit of its space-points, each spacepoint corresponding to a few cm of path length. The charge distribution

over this short path is non-Gaussian, but rather described by the Landau-distribution, which has a long upper tail (the reason for the effect is that the energy distribution of the primary ionization is polynomial, extending to high energy transfers). In order to achieve the best resolving power for particle identification, the straightforward mean of the charges is not the optimum choice due to this tail: instead, the "truncated mean" is calculated for each track, which is the mean of the lower 50% of the charges. The procedure introduces a non-linear distortion of the Bethe-Bloch function, which is taken into account.

In practice, the parametrization of the Bethe-Bloch function has to be determined precisely, and involves a complicated calibration procedure, including the correction for the detector response and track geometry. The procedure in its present form has been developed by G. Veres. For an extensive discussion of the question, see [27].

The precision of the dE/dx measurement depends on the total length of the trajectory within the TPC volume, therefore the clean particle identification is achievable only for reasonably long tracks. The tracks in the momentum region of p<3 GeV tend to be shorter (for the reason that due to the deflection, the tracks do not reach the Main TPC-s), and at the same time, the Bethe-Bloch curves overlap (as seen in Figure 6). This means that the unambiguous particle identification is restricted to the laboratory momentum range p>3 GeV (region of the relativistic rise), with the exception that at low momentum (p<0.9 GeV) the protons become highly ionizing and can be separated even for short tracks.

3.2 Fit of the dE/dx spectra

The particle identification, i.e. the determination of the yields of individual particle species is achieved by the fit of the dE/dx distribution for a small region of momentum. In the Collaboration many different fitting algorithms have been developed [28], [27], [29], [30] and based on these experiences, the Author has developed his own approach. In this section, this procedure will be discussed in detail.

The major steps are the following:

- Track selection.
- Construction of the response function.
- Iterative fitting.
- Error calculation.

The fit is performed in a small range (bin) of the total momentum (p) and the transverse momentum (p_T). The inclusive production cross section is independent of the azimuthal

angle (ϕ), which means that the range can be adjusted desirably for any bin of p and p_T. An important feature of the approach is that *the ϕ-range is adjusted such that in the corresponding bin the acceptance is full and the track-length distribution is reasonable.* "Reasonable" means, that the distribution is not very wide and does not have a long tail towards low number of points, which would worsen the dE/dx resolution. An example is given in Figure 7, where the distribution of the number of track points is shown for two different ϕ ranges. In this way, the analysis is restricted to a fiducial volume of the detector.

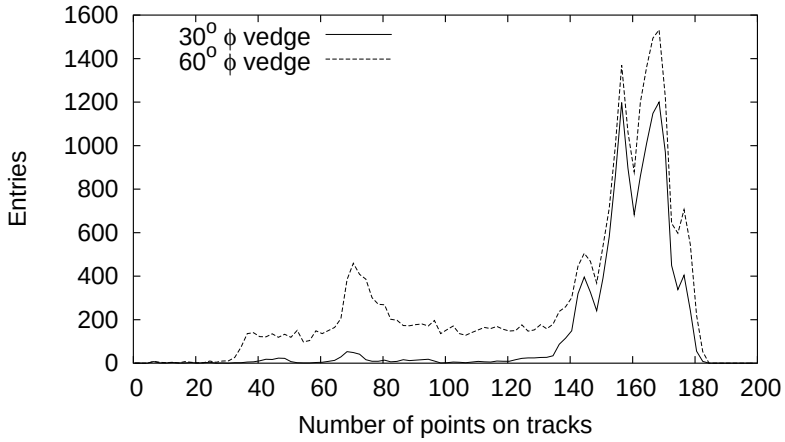

Figure 7: Distribution of the number of points on tracks, for tracks with x_F=0 and p_T=0.6 GeV. For dE/dx analysis, the $\pm 30^o$ wedge is used.

First the ionization values of the selected tracks are filled in a histogram to be fitted. In the second step, the response function, the "lineshapes" of the individual particle species are determined. For a track of a given length, the distribution of the ionization (denoted by x) is to a good approximation Gaussian:

$$G(x, x_0, \sigma) = \exp(-(x - x_0)^2/2\sigma^2)/\sqrt{2\pi}\sigma \tag{1}$$

where x_0 is the mean ionization, closely the value of the Bethe-Bloch function; the deviation is treated as a fit parameter. The width of the distribution, σ, is a function of the track length and the mean ionization x_0, approximately given by

$$\sigma(x_0, N) = \sigma_0 \frac{1}{\sqrt{N}} x_0^{0.625}$$

where N is the number of measured points of the tracks and σ_0 is a constant parameter. For the precise determination of the σ, we refer to [27]. Technically, the approximate value of σ is given by the calibration procedure for each track, and the small relative change is treated as a fit parameter.

The track sample within a bin contains tracks of different track length, therefore the final lineshape is expressed as a sum of Gaussians given by Eq. 1.

The complete fit has nine parameters: the yields of the four particle species (p, K, π, e), the four ionization values (the small shifts compared to the Bethe-Bloch) and the relative change of σ. An example of the dE/dx distribution and the corresponding fit is shown in Figure 8.

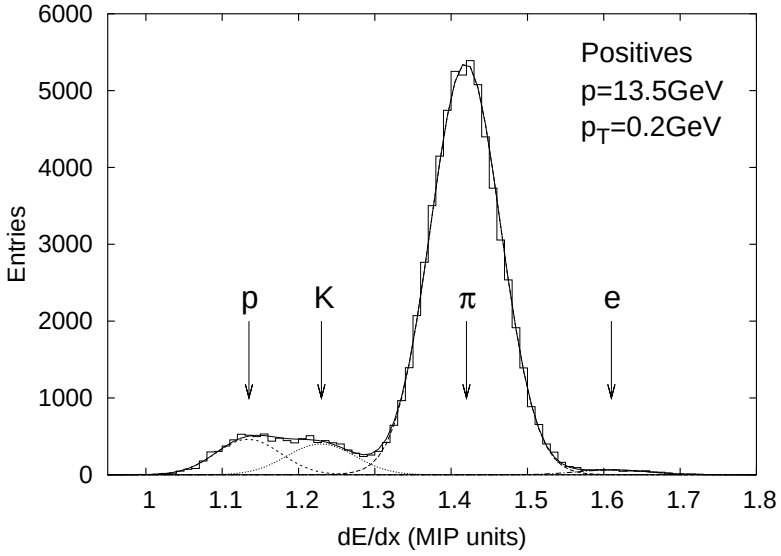

Figure 8: Fit of the dE/dx spectra

In the following step, an iterative fitting over the nine parameters is performed by minimizing the χ^2 of the fit to find the optimum description of the dE/dx histogram. The χ^2 as a function of the fit parameters A^k (k=(1..9)) can be expressed as:

$$\chi^2 = \sum_i \frac{(m_i - T_i)^2}{\sigma_i^2}$$

here i runs over the bins of the dE/dx histogram, m_i is the measured number of entries in the bin, σ_i is the error of the bin content (approximately $\sqrt{m_i}$) and T_i is the fit function determined by the parameters.

The above expression is valid only if the number of entries in the bins is large ($m_i \gg 1$). If the bins contain few (or even zero) entries, the following formula is valid:

$$\chi^2 = 2\sum_i (T_i - m_i + m_i \ln(m_i/T_i)) \tag{2}$$

The minimization is performed by the simple Hessian method. For simplicity, let us assume that the minimum of the χ^2 is at zero parameter value. In this case, close to the

minimum, the χ^2 can be approximated by:

$$\chi^2 = \chi_0^2 + A^k M^{kl} A^l$$

(k and l runs over the nine parameters). In the minimum the first derivative of χ^2 with respect to A^k must vanish:

$$\frac{\partial \chi^2}{\partial A^k} = M^{kl} A^l = 0$$

This derivative can be calculated from the expression (2) of the χ^2:

$$V^k = \frac{1}{2}\frac{\partial \chi^2}{\partial A^k} = \sum_i \frac{T_i - m_i}{T_i} F_i^k \qquad F_i^k \equiv \frac{\partial T_i}{\partial A^k} \tag{3}$$

Similarly the second derivative:

$$M^{kl} = \frac{1}{2}\frac{\partial^2 \chi^2}{\partial A^k \partial A^l} = \sum_i \left(\frac{m_i}{T_i^2} F_i^k F_i^l + \left(1 - \frac{m_i}{T_i}\right) \frac{\partial F_i^k}{\partial A^l} \right) \approx \sum_i \frac{1}{T_i} F_i^k F_i^l \tag{4}$$

The above calculation gives an algorithm to search for the minimum. In the first step, the starting values of the parameters are chosen, and the T_i and F_i^k are calculated. The first and second derivative of the χ^2 is calculated from Eq. 3 and 4. Then the matrix equation $M^{kl} A^l = V^k$ is solved for A^l, resulting in a better estimate of the parameters. This procedure is repeated until the minimum is reached; the convergence requires 5-6 iterative steps.

The errors can be calculated as the diagonal elements of the inverse of the second derivative matrix M^{kl}: the error squared of parameter A^k is $(M^{-1})^{kk}$. This statement can be intuitively understood: the χ^2 may be seen as a probability variable with a normal distribution (provided that there are many entries in the whole histogram). In the parameter space (A^k) the *contours* of constant χ^2 can be defined; the contour which is one unit above the minimum encircles the true parameter value with 68% probability. The maximum width of this contour is given in any parameter direction by $(M^{-1})^{kk}$.

3.3 Fits in the low-momentum (backward) region

In the NA49 experiment, the particle identification is optimized for the region of the relativistic rise (p>3 GeV). At low momentum however, despite the short tracklength, protons can be separated by their high ionization. In this region, the mean ionization varies rapidly with the momentum, so appropriately small bins must be used.

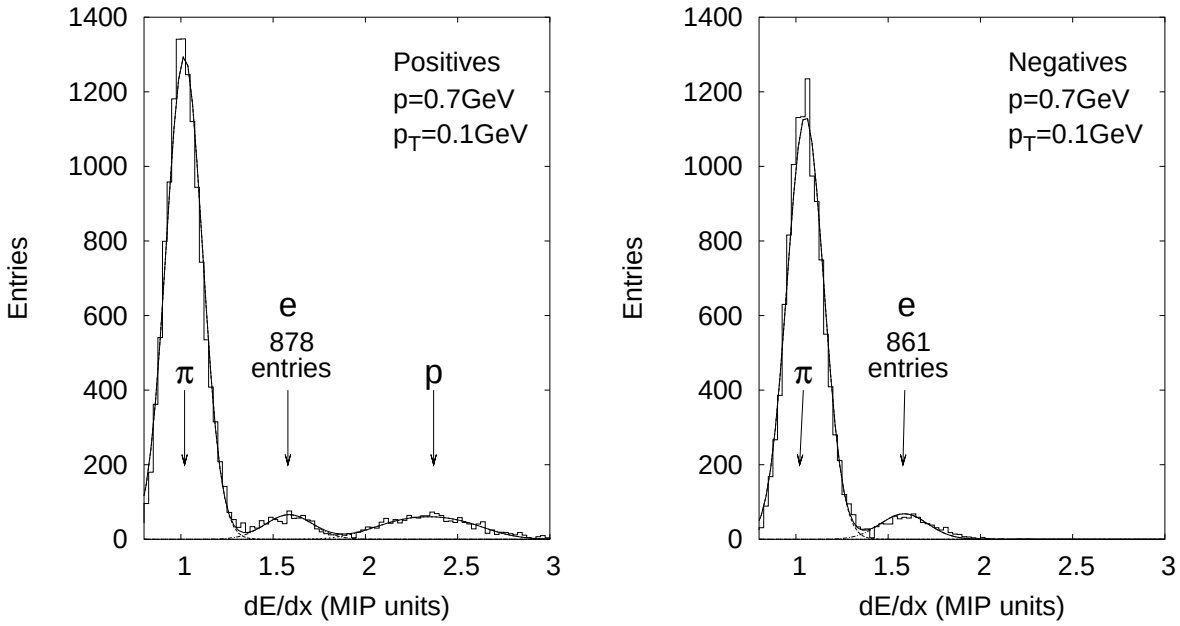

Figure 9: Fits in the backward region: the same bins of positive and negative charges. The protons are well separated. There are no antiprotons in this region. Note that the number of positrons and electrons is the same.

A typical example of the dE/dx distribution in this region is shown in Figure 9. Pions and kaons are close to the minimum, protons has the highest ionization and the electrons sit in between.

A specific problem in this region is that the protons may overlap with the electrons (the complete overlap takes place at about 1GeV). This can be circumvented by the assumption, that the *number of electrons and positrons is equal*. The reason for that is that the main sources of electrons and positrons in hadronic interactions are symmetric for the two charges: the Dalitz-decay of π^0 as well as the gamma conversions into electron-positron pair. With this assumption, the fits and the individual tagging of protons are feasible for the complete range of p<1.3GeV (see Figure 6).

4. Measurement of neutron production

4.1 Experimental setup

The forward neutrons produced in hadronic interactions are detected in the Ring Calorimeter [23]. The Calorimeter is placed 18m downstream from the target with a fiducial area of about 1 m^2 (which is about 15% of the total surface, the rest being shadowed by detector components). The geometrical acceptance corresponds to a p_T cutoff of about 1GeV at $x_F = 0.2$ (35 GeV energy).

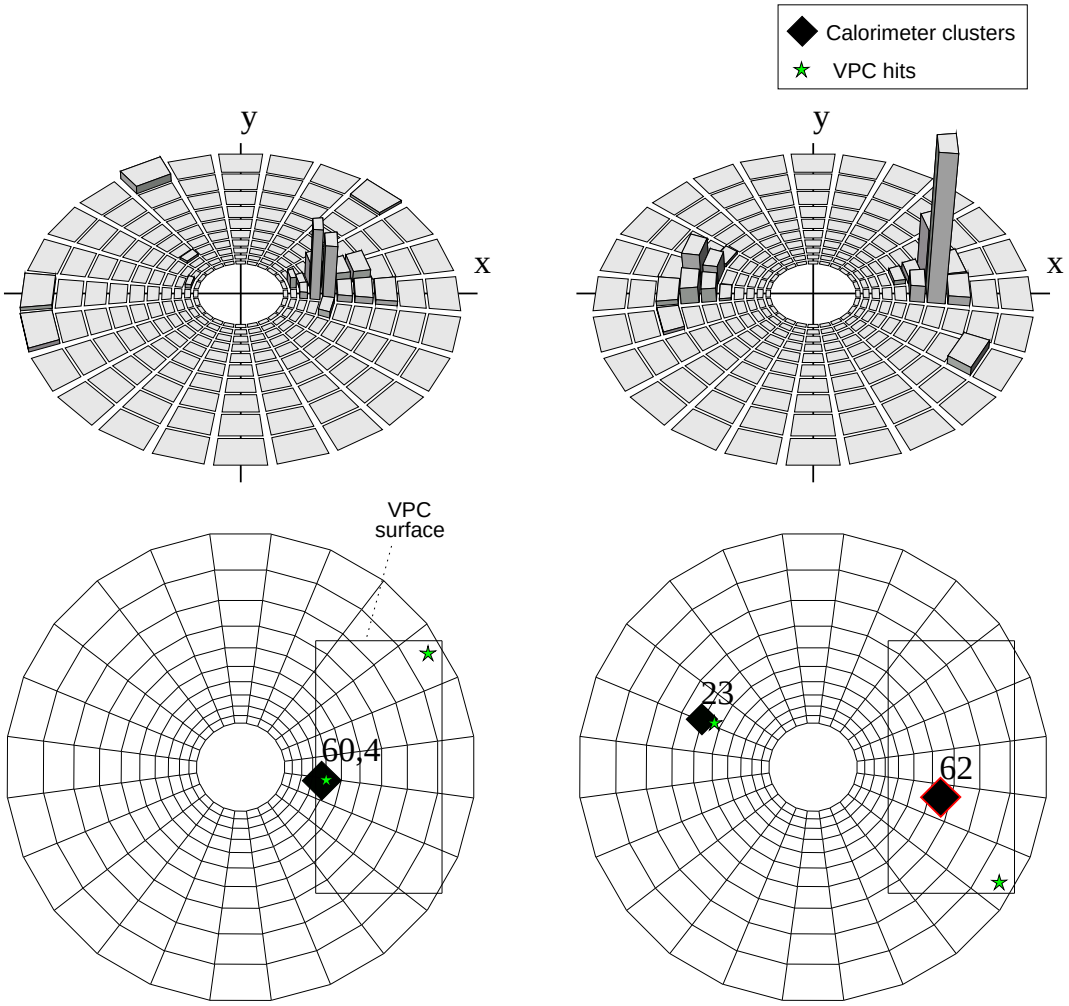

Figure 10: Events in the Calorimeter and VPC-s. Calorimeter energy deposit (clusters) on the top, with the projection of the VPC to the Calorimeter surface in the bottom. On the left, the cluster in the Calorimeter is tagged by a hit in the Veto Chamber. On the right, there is no hit in the VPC-s, so the Calorimeter cluster is identified to be a neutral particle.

The majority of the neutrons and the fastest charged particles travel through the gap between the Main TPC-s. In order to discriminate between neutral and charged particles, the two Veto Proportional Chambers (VPC) were constructed and placed behind the Main TPC-s. In this way, the clusters of energy deposit in the Calorimeter can be tagged if a corresponding hit is present in the VPC-s.

Two examples of typical events are given in Figure 10. The bottom panels show the clusters and the VPC-s projected on the Calorimeter surface. The energies of the clusters is also marked in units of GeV.

The Calorimeter and VPC setup detects all the high momentum particles which escape through the gap in the middle of the TPC system. Since the TPC-s have a large acceptance for charged particles, the detector complex ensures hermeticity in the forward direction. This is demonstrated in Figure 11: the sum of the energies stored in charged and neutral particles approach the incoming beam energy (the loss is mainly due to the π^0-s passing outside the acceptance of the Calorimeter). The figure contains p+p events at 158 GeV beam momentum without any selection.

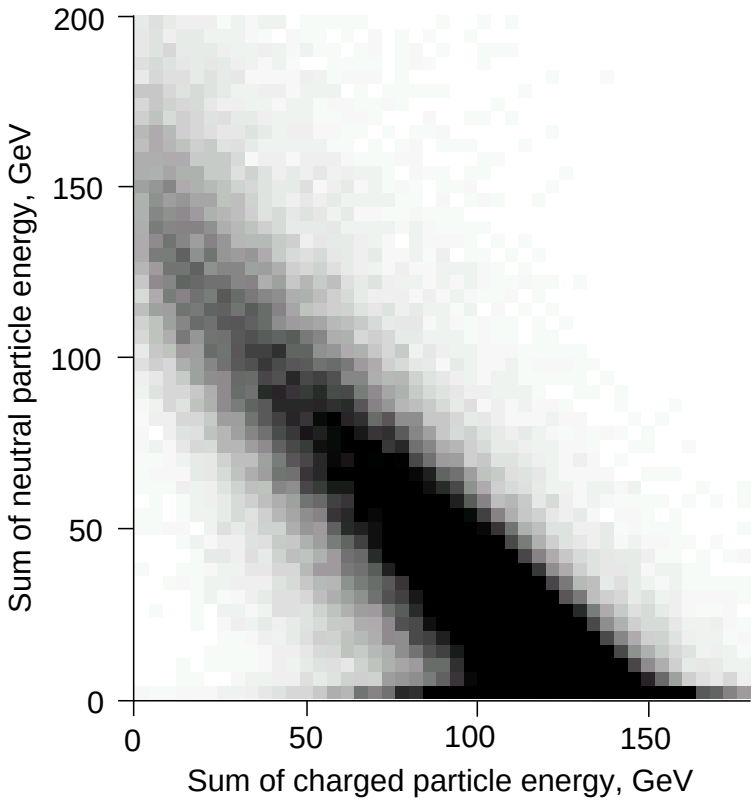

Figure 11: Hermeticity in forward direction: the sum of the energies of charged and neutral particles add up to about 85% of the beam energy.

4.2 Performance of the Ring Calorimeter

The perspective view of the Ring Calorimeter is shown in Figure 13, taken from [23]. The barrel-shaped Ring Calorimeter is divided into ten rings and 24 radial sectors, defining 240 cells. Each cell is built up from two parts: the electromagnetic (photon) part in the front and the hadronic part behind. The electromagnetic part contains layers of lead as absorber between the scintillator sheets and adds up to about 20 radiation length of material. The hadronic part has 4 interaction length in total, with steel absorber layers. The two parts are read out independently by a lightguide rod running through the cell. The electromagnetic shower initiated by the incoming photon or electron is contained in the electromagnetic part, and therefore it can be distinguished from the hadronic showers of larger size.

The energy deposit appears in the Ring Calorimeter as a cluster, restricted to a few neighbouring cells, as it is shown in Figure 10. The number of available cells is relatively small, which means that single particle detection is only achievable in the low multiplicity environment (p+p, p+A interactions). A simple cluster finding algorithm has been developed, which searches for a large integrated energy deposit in a limited geometrical region.

The Calorimeter response was studied in detail in 1999. The observations were compatible with the results of earlier, very extensive studies [23]. Since then, the calibration of the Calorimeter is checked or repeated in the beginning of each run period.

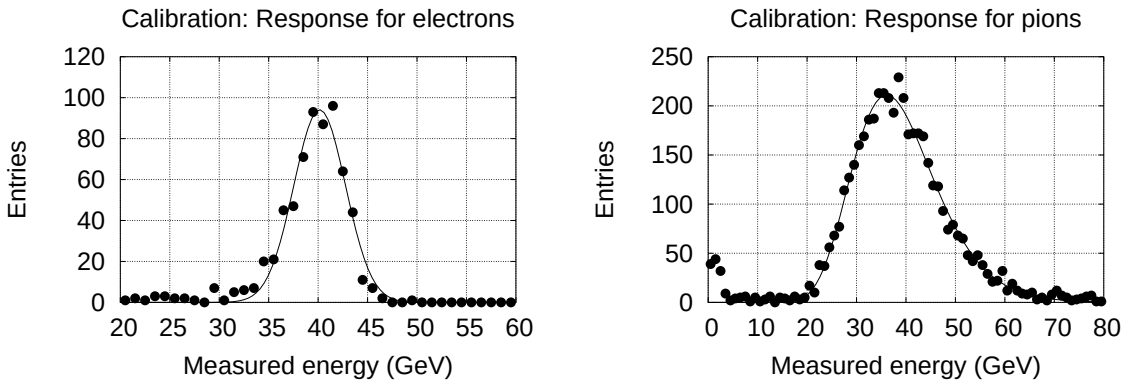

Figure 12: Energy response of the Calorimeter in a calibration run

The energy response of the Calorimeter for hadronic (π^-) and electromagnetic (e^-) particles is shown in Figure 12 in a calibration run at 40 GeV beam momentum. For e^-, the distribution is Gaussian; on the other hand, for π^- the distribution is skewed and the resolution is much worse. The unfolding of the energy resolution relies on the precise shape of this curve, which was described by a lognormal distribution (continuous line in Figure 12). The energy resolution of the Calorimeter was parametrized in the following way:

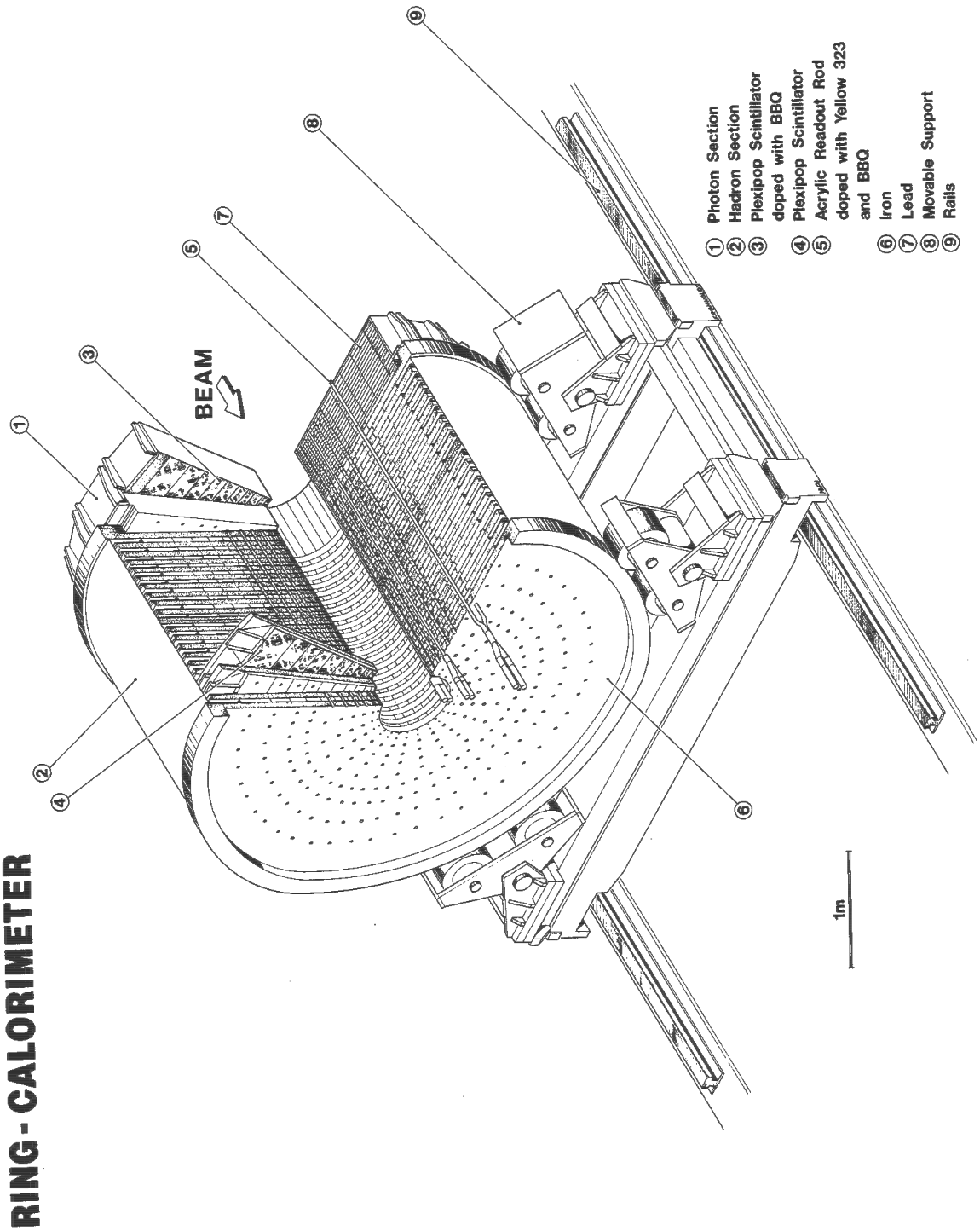

Figure 13: View of the Ring Calorimeter from [23].

$$\sigma(E)/E = \sqrt{(0.9 \pm 0.1)/E + (0.02 \pm 0.005)} \quad (5)$$

where the constant term appears due to the non-uniformity of the Calorimeter.

The distinction between hadronic and electromagnetic particles is based on the fraction of energy deposited in the corresponding part of the Calorimeter. The response of the Calorimeter for 40 GeV calibration beam is shown in Figure 14.

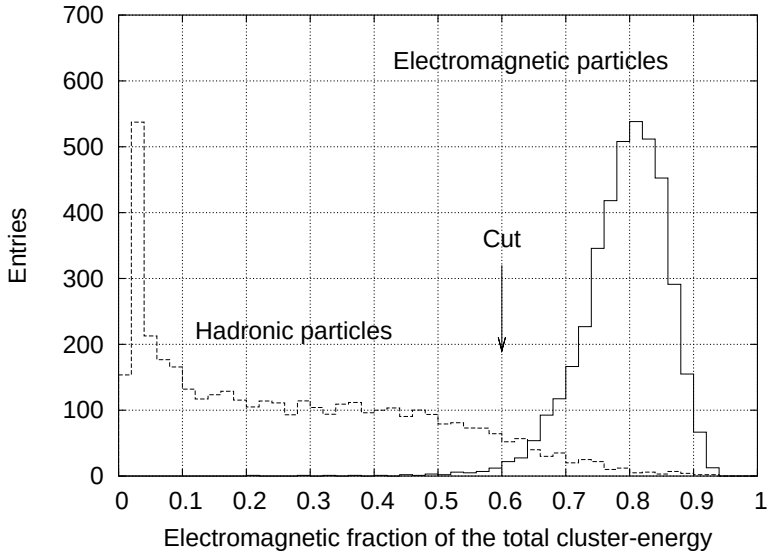

Figure 14: Response for electromagnetic and hadronic particles in a calibration run: the fraction of energy deposited in the electromagnetic part characterizes the two types of showers

The electromagnetic particles can be rejected from the sample by placing a cut on the electromagnetic fraction of the measured energy. In the analysis, clusters with this fraction below 60% were defined as hadronic clusters. This cut rejects about 98% of electromagnetic particles (mostly gammas from π^0 decay). The loss due to the cut as a function of particle energy can be determined from calibration with beams of different momenta and also by matching the tracks in the TPC system and the corresponding Calorimeter clusters in the region of common acceptance. The loss is shown in Figure 15.

4.3 Performance of the Veto Proportional Chamber

The two walls of Veto Proportional Chambers (VPC-s) are placed in front of the Ring Calorimeter to provide a charged particle veto. As it was mentioned, geometrically the VPC-s cover the gap between the two Main TPC-s. This requires a large sensitive area, which

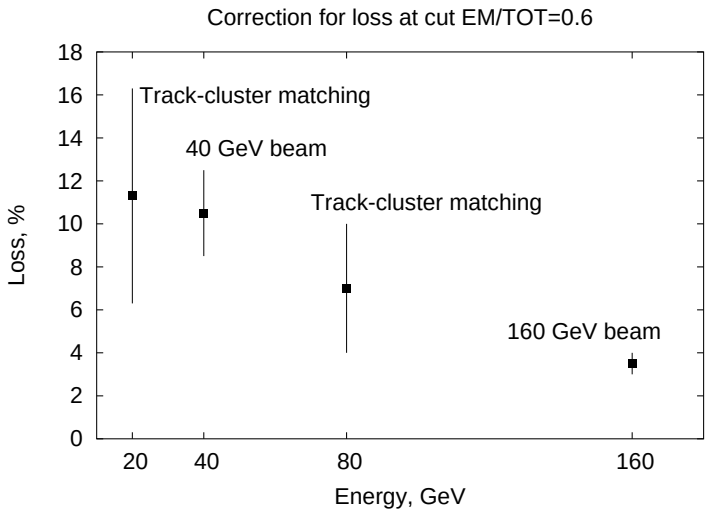

Figure 15: Efficiency of neutron detection: loss due to the cut on electromagnetic fraction

had to be reached without an excessive number of electronic channels. The construction had to be simple and cheap. The system was completed in three months, with a number of students involved at all stages of the construction.

The device is a classical proportional chamber with strip readout. The signal is created on the horizontal wires which is capacitively coupled to the *planes of cathode strips on both sides*. The structure of the strips is shown in Figure 16. The strips are inclined in the opposite direction on the two sides, and the intersection of the firing strips defines the two dimensional position of the hit. The four strip planes contain altogether 320 channels of electronics with CAMAC readout.

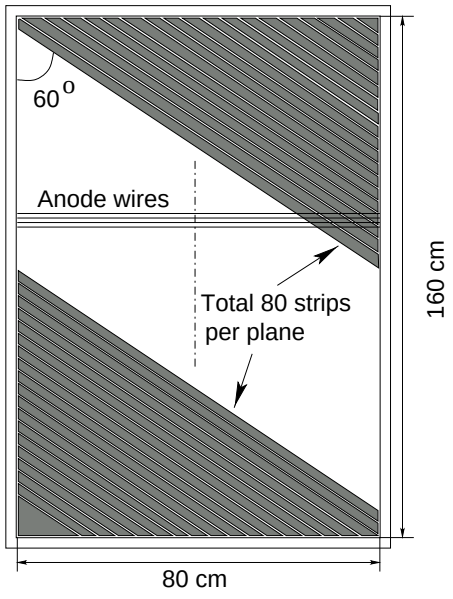

Figure 16: Cathode strips of the VPC. The readout strips are inclined at 60^o, opposite direction on the two sides.

A typical event is shown in Figure 17 with one particle in the chamber. The hit appears in all the four planes. Due to the capacitive coupling, the charge deposit (pulseheight) from the same hit has to be closely the same on both sides, since the same avalanche induces the signal on the strips.

The initial steps of data reduction are the baseline correction, crosstalk correction and gain calibration. The examples shown in Figure 17 already contain these corrections.

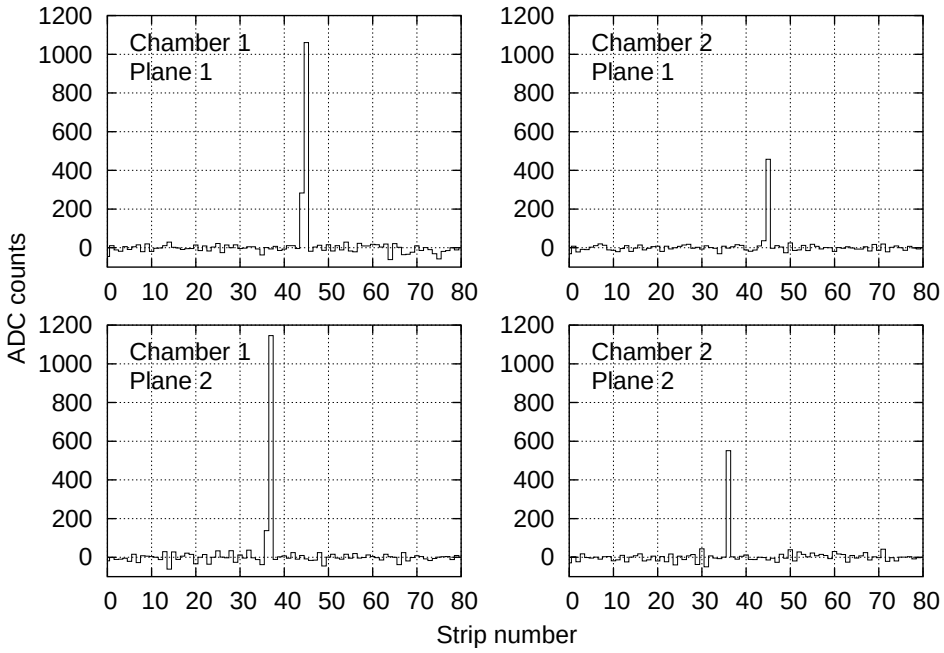

Figure 17: Event in the VPC with one particle. The hit appears in all the planes, and the charge (pulseheight) is closely the same on the two planes of the chambers.

The baseline correction adjusts the baseline event by event, which fluctuates due to the pickup-noise; the source of this noise was not investigated, since it stayed at an acceptable level over all the run periods. The baseline can also vary due to a high charge deposit in the chamber, which induces a signal simultaneously on all strips.

The strips are capacitively coupled to each other, which causes crosstalk. The crosstalk between neighbours was found to be about +10%, which is corrected for. The crosstalk between second- or further neighbours are neglected.

The gain calibration is performed via an iterative process, which in each step adjusts the gains so that the mean charge ratio for the two hits of the same particle approaches 1. The gain has a channel by channel variation of 20% and is found to be stable over each run period.

The detector has high efficiency, as it is usual for proportional chambers: the efficiency was found to be higher than 99% from the analysis

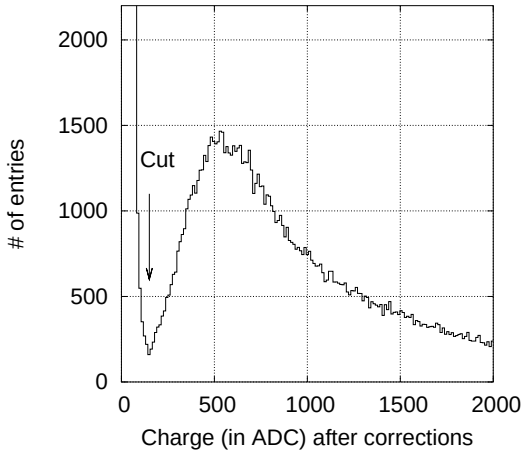

Figure 18: Charge deposit distribution in the VPC, initiated by muons.

of data taken with muon trigger. The charge distribution for this dataset is shown in Figure 18. The signal is clearly separated from the noise, and the cut limit of accepting hits is so low that it ensures high detection efficiency.

If a single particle hits the chamber, the intersection of the firing strips on the two planes defines the hit position. If a double (or multiple) hit appears from two particles, there may be ambiguous intersections. These fake combinations can be rejected by observing the deposited charge on the two sides, which has to be closely the same. This advantage permits to unfold the ambiguous patterns.

The difference of the charges on the two planes from the same hit in VPC1 is shown in Figure 19. At large pulseheights, the difference approaches about 6% of the charge, at low pulseheights this is added up to the electronic noise of the readout.

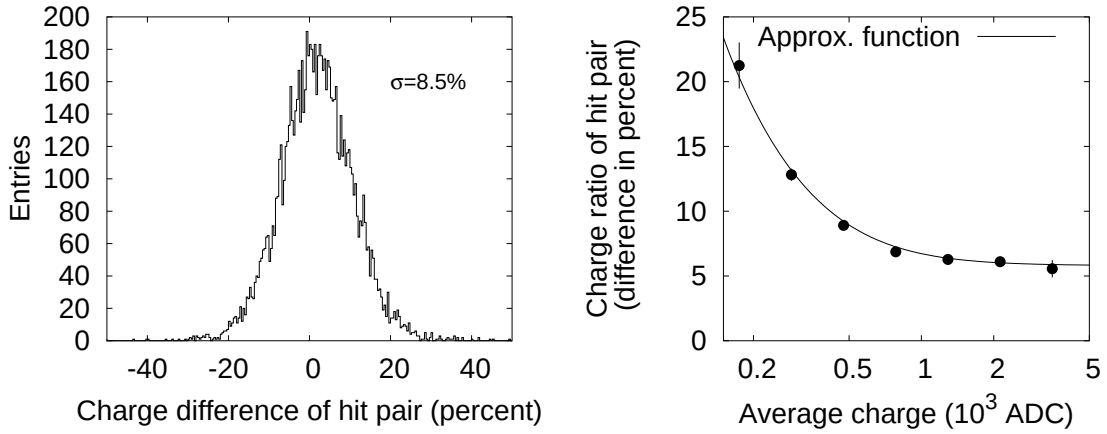

Figure 19: Charge difference on the two planes of VPC1 for a single hit. On the left, the charge difference of hits around the mean pulseheight (ADC≈500) is shown. The distribution is closely Gaussian. On the right, the charge dependence of the sigma of the distribution is shown

A pattern recognition algorithm was developed and shown to be reliable up to 3-4 hits (the probability of finding 5 or more hits is below 4%). In this algorithm, the probability of each possible pattern is determined using this charge dependence, and the most probable pattern is chosen.

The position resolution is defined by the geometry of the strips. The strips are wide compared to the gas gap of 6 mm between the cathode and the anode wires, therefore a hit fires only two strips. The strips of 2.5 cm width could provide a position resolution of 2 mm, which is reached by taking into account the charge deposited in two adjacent strips in the same hit. The resolution in the horizontal direction is slightly worse (determined by the inclination angle of the strips). The actual values are measured from the analysis of TPC

tracks passing through the VPC-s: this is shown in Figure 20.

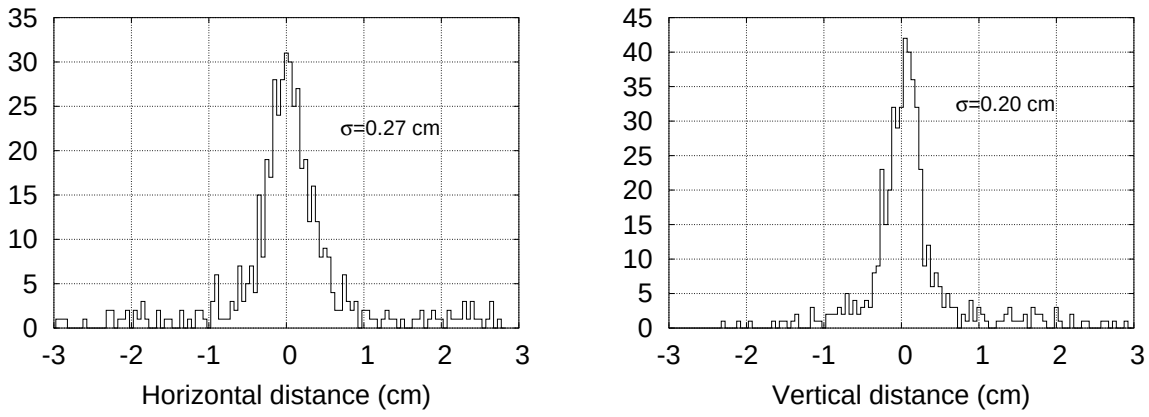

Figure 20: Position resolution of the VPC measured by the difference of the actual VPC hit and the extrapolation of TPC tracks to the VPC surface

4.4 Unfolding of the neutron energy distribution

The last phase of the analysis is the unfolding of the neutron spectra for the energy resolution of the Calorimeter and the overlap of clusters. Based on earlier works [31], a Monte Carlo simulation has been developed, which includes acceptance, energy resolution and possible overlap of clusters (i.e. if two particles falls close to each other in the Ring Calorimeter and appear as a single cluster). The neutron spectrum is the input parameter of the simulation, and by adjusting the simulated distribution to the measured raw energy distribution, the neutron spectrum is determined. The raw and the unfolded spectra is shown in Figure 21.

The adjustment is performed via an iterative process, similarly to the method of dE/dx fitting described in Chapter 3., taking the yields in each bin of the spectrum as parameters.

The raw and the unfolded spectra falls relatively close to each other, which demonstrates that the energy resolution of the Calorimeter is not so weak that it would distort the shape of the distribution: a large difference between the raw and unfolded spectra would indicate that the result strongly depends on the details of the Calorimeter response. The excess of the raw measured energy above the kinematic limit is explained by energy resolution.

The performance of the Monte Carlo simulation was verified in two ways. The cluster shape assumed in the simulation was compared to the cluster shape measured in beam trigger events or calibration runs. A further crosscheck was performed to assess the reliability of the predicted overlap probability using event mixing technique. In this method, the raw ADC values from two subsequent events were added up, and were analyzed with the normal

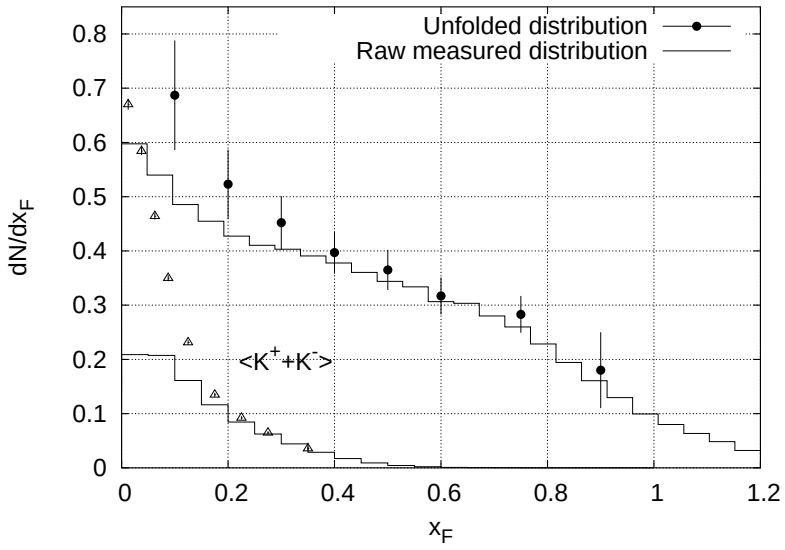

Figure 21: Unfolding of the neutron distribution.

cluster finding algorithm. The deviation in such a sample from the sum of the distributions in the original events is due to cluster overlap. The simulation could reasonably predict the deviations.

The hadronic clusters from neutral particles include neutrons, antineutrons and long-lived kaons (K_L^0). The K_L^0 contribution has been subtracted (shown in Figure 21 assuming that the K_L^0 distribution can be approximated by the mean of charged kaons measured in the TPC system). The final result is the sum of neutron and antineutron.

4.5 Assessment of the systematic errors

The error on the neutron yield is dominated by systematics. The most important error sources are the following:

- Calibration of the Calorimeter.
- Efficiency and losses due to cuts in the Calorimeter.
- Unfolding of the energy resolution.
- Misidentification due to ambiguous patterns in the VPC-s.

The other error sources are negligible (e.g. inefficiency of the VPC, acceptance).

The systematic errors were estimated by varying the corresponding parameters and performing the unfolding with these changed values.

The error on the energy calibration is about 5-6%, which in the high momentum region reflects in a 10-15% error on the yield.

The results are weakly sensitive to the parameters of the energy response (see formula (5) in Page 35), in the sense that the corresponding systematic error is much below the contribution from other sources. Changing the parameters, the shape is invariant, only the description of the raw spectrum above the kinematic limit changes.

The final results are presented in Section 8., taking into account the proper normalization and feeddown from weak decays.

5. The Gap-TPC

In 2001 the NA49 TPC system has been extended with a small-size chamber, the Gap-TPC (GTPC). The device is placed between VTPC1 and VTPC2, such that the beam passes through the sensitive volume. This means that all high momentum charged particles which up to then escaped the detector through the gap between the TPC-s are now detected on a short piece of their trajectory.

The achievements of the GTPC are the following:

- Detection of the very forward particles (protons). GTPC track-pieces matched with the hits in the Veto Chambers extend the acceptance in the forward region where the tracks miss the MTPC-s.
- Improved V0 detection. The improved track extrapolation provides more precise invariant mass measurement for weakly decaying particles (provided that the track pairs detected also in other parts of the TPC system) since the position of the decay point is better defined.
- Improved main vertex resolution. All the high momentum tracks now have a short, well measured piece closer to the target which improves the track extrapolation to the main vertex.
- Cleanup of the MTPC-only tracks. Tracks appearing only in the MTPC may be electrons produced in downstream gamma conversions, and since these tracks are not detected in the magnetic field, they may fake a high momentum hadron. Now all the tracks of this class receive some points in the GTPC and therefore the electrons can be rejected.

In the 2001 and 2002 proton run periods, data was taken with proton beam on proton and nuclear targets, including the GTPC in the readout.

5.1 Construction of the Gap-TPC

The GTPC closes the gap between the other TPC-s of NA49, so the beam passes through the sensitive volume. This requires a special design to avoid unreasonably increased background from secondary interactions and conversions: the guiding principle of the construction was to put as little amount of material as possible in the beamline.

The outline of the GTPC is shown in Figure 22. The device is a classical TPC where the electrons from the primary ionization drift through the gas volume in a uniform electric field and detected in the readout chamber.

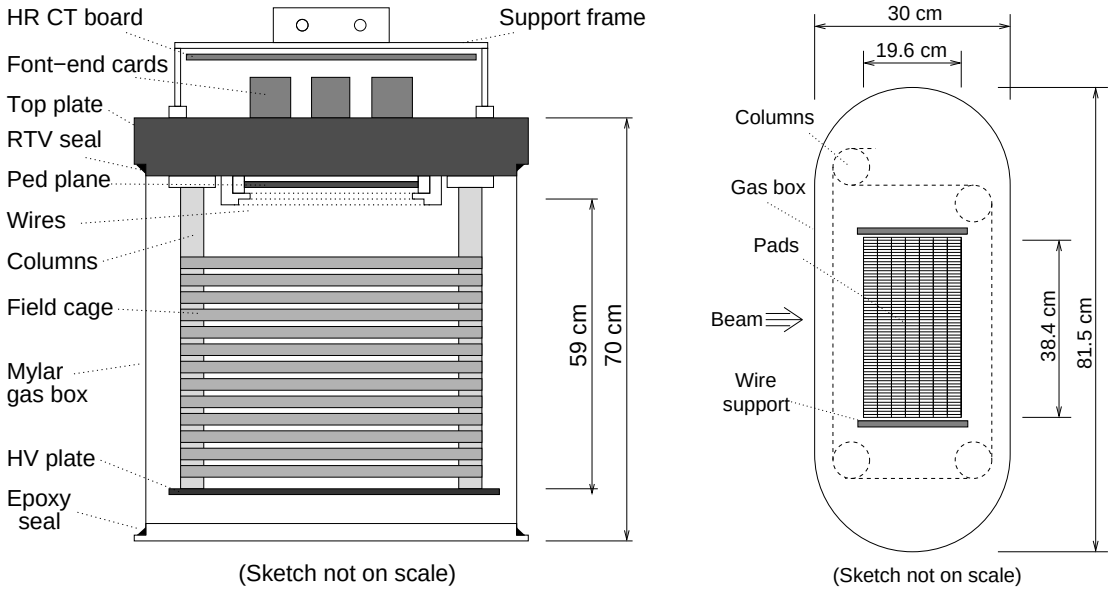

Figure 22: Outline of the GTPC, front view from the beam direction (left) and view from the bottom (right).

The electric field in the drift volume is defined by the field cage, which is built up from aluminized Mylar strips, connected to a resistor chain. The drift voltage is 11.3 kV over a drift length of 59 cm, providing a drift time of about 50 μs. The Mylar strips are supported by glassepoxy columns, tubes with wall thickness as small as 100 μm, which is a key invention in order to reduce the material that the particles have to cross. The complete drift volume is enclosed by a gasbox made of Mylar. The overall thickness of the detector, assuming that the particle passes through the gasbox, the gas volume and one column is about 0.15% radiation length and 0.05% interaction length.

The principle of operation of the TPC-s were discussed in Chapter 2. The pads are 28 mm long and 4 mm wide (similarly to VTPC2), ordered in 7 rows with 96 pads in each row. The gas composition is Ne/CO_2, similarly to the VTPC-s.

The construction had two further aspects besides the little amount of material to be used: this is cost effectiveness and simple inclusion in the NA49 DAQ (Data Acquisition) system. Cost effectiveness, similarly to the Veto Chambers, was achieved by careful design using commonly available materials and involvement of students in the actual handiwork. For the electronics of the device, spare parts of the huge NA49 TPC system were used, which meant a sizeable reduction of the cost. This also allowed the straightforward inclusion of the electronics in the DAQ by defining new readout channels.

The construction started in February 2001 and in September the first data was taken

with the GTPC. During the 2002 Running Period, nearly 3 million p+p events were taken. This dataset has been reconstructed and processed, and became the basis of the present thesis.

5.2 Local and global track reconstruction in the GTPC

The inclusion of the GTPC in the NA49 track reconstruction chain consists of the following steps: cluster finding, local tracking and global tracking.

The cluster finding, which builds up single spacepoints from the two dimensional clusters of ADC counts for each padrow, is common with the algorithm of the other TPC-s. In this case the technical problem of pad geometry, detector geometry and proper ordering of the data had to be solved.

The local tracking is optimized for short straight tracks: in the low magnetic field of the GTPC, this assumption is reasonable. In Figure 23, a typical event in the GTPC is shown.

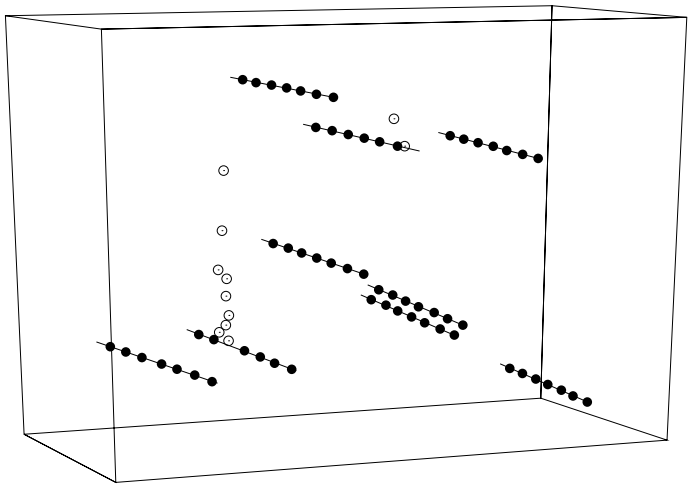

Figure 23: Perspective view of an event in the GTPC. The points on tracks (full dots) fall close to the straight line assumption. The empty dots show points not on tracks (background).

The tracking algorithm searches for sets of points which fall within a thin straight cylinder with a radius of 0.5 cm. This value is an optimum between losing points which fell far from the track on a statistical basis (outliers), and picking up background or even points from other tracks. The tracking inefficiency is below the percent level, which can be estimated from the point loss of global GTPC tracks. The number of point distribution is shown in Figure 24; the probability of losing two points from the possible seven points is less than 1%, and tracks with 4 points are still used in the analysis.

The last step of track reconstruction is the global tracking, which is the matching of the GTPC tracks with tracks in the other TPC-s. The matching is decided upon geometrical distance: the GTPC track-piece has to fall within an elliptical region around the extrapolated track trajectory (the region is wider in the horizontal direction, as the extrapolation error is larger in the bending plane). Relying on the full local tracking efficiency of the GTPC, the tracks are required to have points in the GTPC if the extrapolated trajectory passes through the fiducial volume of the chamber.

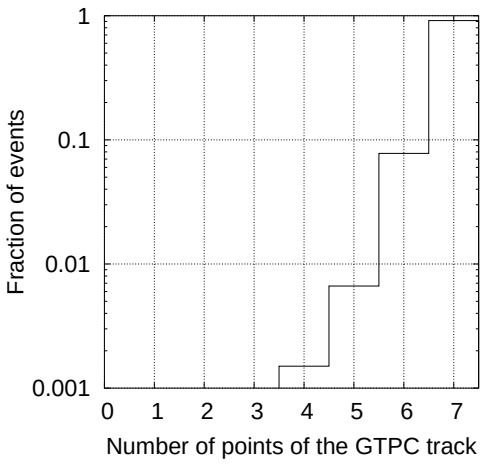

Figure 24: Distribution of the number of points for local GTPC tracks.

6. Forward proton detection with the GTPC+VPC

The acceptance of the original NA49 detector setup cuts off for high momentum particles at about x_F=0.6 (or about 100 GeV momentum), because the bending magnets can not bring the trajectory inside the sensitive volume of the MTPC. These tracks are detected in the Veto Chambers (VPC-s), but there the position resolution is not sufficient to determine the momentum of the particle. With the inclusion of the GTPC, a reasonable momentum measurement is achievable by the combined GTPC+VPC reconstruction. The improvement of the acceptance is demonstrated in Figure 5.

6.1 Experimental setup

The particles originating from the Main vertex (primary interaction) are detected in the GTPC and the Veto Chambers. These three sets of points are sufficiently far from each other to provide a reasonable lever arm for momentum measurement. The sketch of the experimental setup is shown in Figure 25.

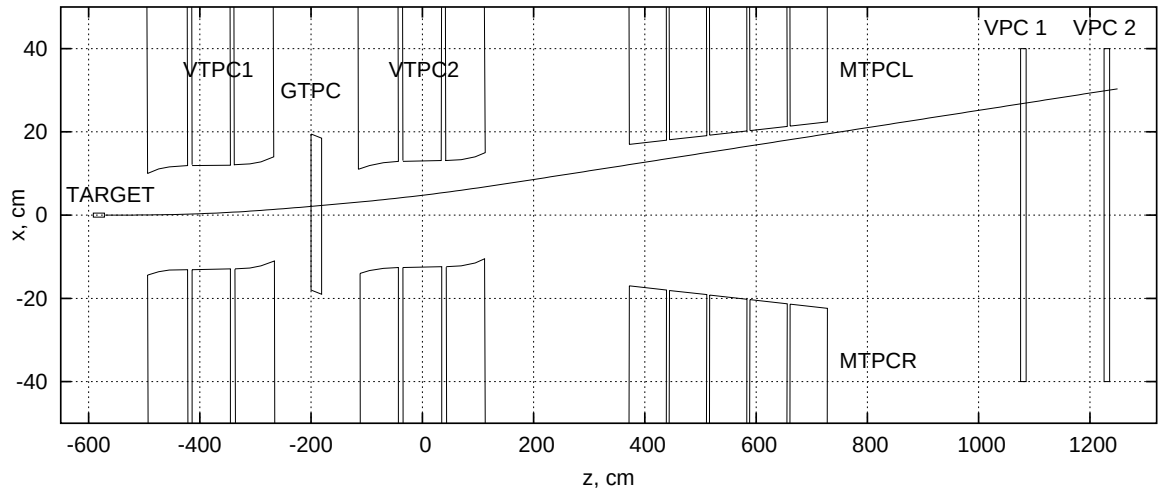

Figure 25: Forward proton detection with the GTPC and the VPC-s: the trajectory of a 110GeV particle is shown. The scale is extended in the x direction.

6.2 Combined GTPC and VPC track reconstruction

The track reconstruction proceeds with the following steps:

- Matching of the GTPC track piece and the hit in the VPC.

- Determination of the χ^2 referring to the goodness of the match. Candidates with high χ^2 are rejected.
- Momentum fitting.

The starting point of the track is assumed to be the Main Vertex, determined by the Beam Position Detectors (BPD-s), which means that the trajectory is defined by the 3 momentum components as parameters. From the GTPC, the spatial position and elevation angles of the track piece are measured; each of the two VPC-s provide the position information, so altogether 8 numbers are measured for the track. The corresponding fit has a reasonable redundancy with 5 being the number of degrees of freedom.

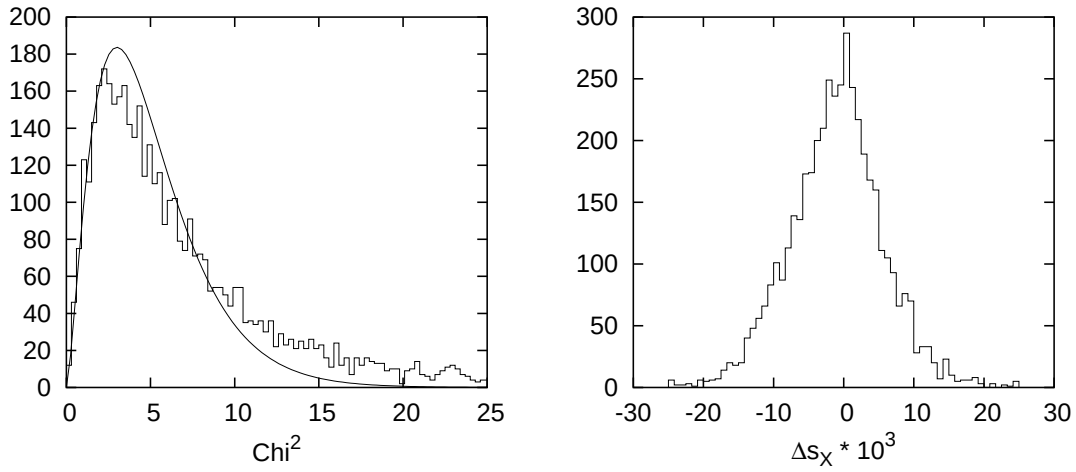

Figure 26: Distribution of χ^2 of the momentum fit and the distribution expected for $n_{\mathrm{DOF}} = 5$ (left panel). The deviation of the horizontal slope measured in the GTPC from the fitted track trajectory (right panel; see explanation in the text).

The χ^2 distribution is shown shown in Figure 26. The χ^2 definition is based on the distance between the measured points and the fitted trajectory, which requires the knowledge of the individual errors of the measured points. The position errors were determined in the following way: the tracks were fitted with leaving out one of the position informations (e.g. the horizontal track angle of the GTPC, shown on the right panel of Figure 26) and the deviation of this quantity from the fitted track was measured. The procedure is only a first order approximation, but the analysis has shown that the final result of the momentum fit is largely independent of the actual parameters of the χ^2 definition.

The reconstruction procedure was checked with beam trigger data, when the non-interacted beam particles pass through the detector system. The momentum components of the reconstructed tracks are shown in Figure 27. The p_x and p_y distribution is centered

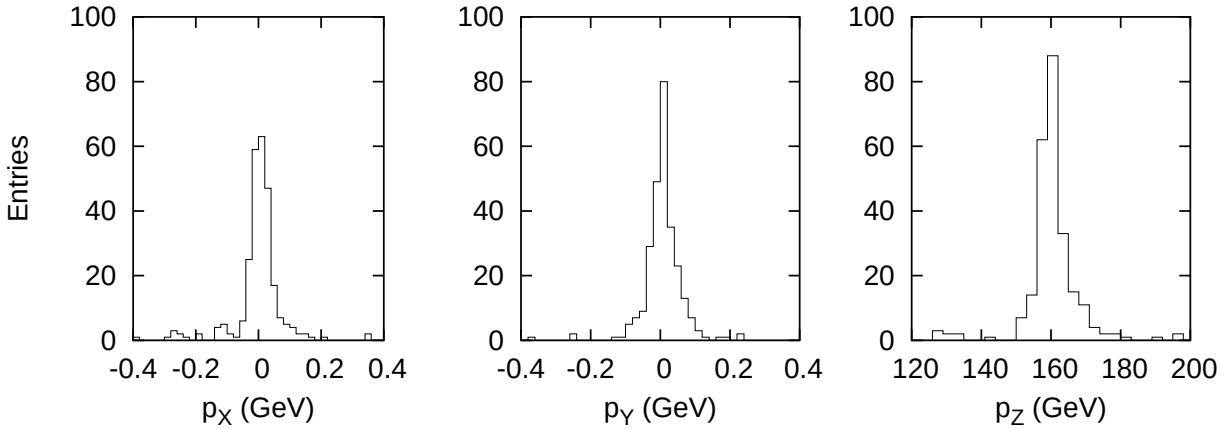

Figure 27: Measured momentum components of beam trigger tracks

around zero; the p_z scatters around the nominal beam momentum of 158 GeV. The fact that p_x and p_y is centered provides a very strong constraint on the detector alignment: up to now, the overall detector geometry could only be checked with external survey. From the actual data, the alignment is shown to be better than 150μm both horizontally and vertically.

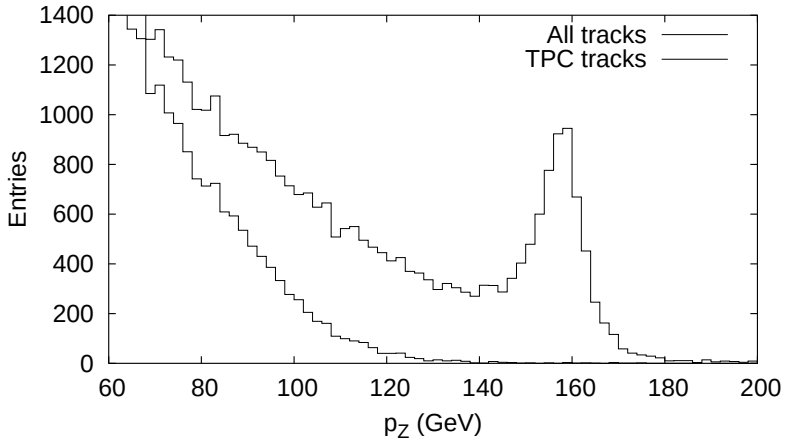

Figure 28: Raw p_z distribution in p+p interaction. The diffractive peak is clearly visible.

The longitudinal momentum resolution is estimated to be approximately

$$\frac{\Delta p_z}{p_z} \approx 0.025\% \times p_z(\mathrm{GeV})$$

and the error is dominated by the VPC position resolution. The transverse momentum resolution is

$$\Delta p_t \approx 2 \times 10^{-4} p_z$$

dominated by the GTPC and vertex resolution. The corresponding 25 MeV uncertainty at p_z=160 GeV is small enough to allow the extraction of transverse momentum distributions up to the kinematic limit.

The raw p_z distribution of reconstructed tracks in p+p collisions is shown in Figure 28. The plot demonstrates the increased acceptance: even the diffractive peak is visible.

The production cross section of forward protons was determined using the GTPC+VPC tracks in p+p interaction. The results are discussed in Section 8.

7. Normalization and corrections

7.1 Inclusive cross section

The interaction cross section is generally defined as the number of interactions per unit time $\mathrm{d}N_{int}/\mathrm{d}t$ within a volume element $\mathrm{d}V$ of two intersecting particle beams:

$$\mathrm{d}N_{int}/\mathrm{d}t = \sigma_{int} n_1 n_2 (v_1 - v_2)\mathrm{d}V$$

where n_1 and n_2 are particle densities within the beam. In the fix-target setup, the beam collides with the target at rest. Under this condition, the integration over the volume can be performed: the integration over the surface perpendicular to the beam gives the total beam intensity, in the parallel direction results in the target length λ. The interaction cross section is thus determined by the target geometry and the interaction rate:

$$\sigma_{int} = \frac{1}{n_2 \lambda} \frac{N_{int}}{N_{beam}}$$

where N_{int} is the number of interactions and N_{beam} is the number of incoming beam particles. The meaning of the above formula is that the cross section of a specific observable process ("interaction") is expressed in terms of the target geometry and the occurrence rate of the process per incoming beam particles. In a practical experiment, only those events are recorded, "triggered", when the beam particle did not pass through the target without any interaction. The cross section of the specific process in question can be determined from the collected event sample. Here one has to assume that the collected sample contains all occurrences of the specific process, or in other words, the trigger is bias free[3]: then one gets

$$\sigma_{int} = \frac{1}{n_2 \lambda} \frac{N_{trigger}}{N_{beam}} \frac{N_{int}}{N_{trigger}} = \sigma_{trigger} \frac{N_{int}}{N_{trigger}}$$

The trigger cross section, $\sigma_{trigger}$, involves the trigger rate $N_{trigger}/N_{beam}$ besides the target geometry. The $N_{int}/N_{trigger}$ is determined by the physics analysis of the process within the collected data sample. The trigger cross section for each run period was calculated by Ondrej Chvála; the procedure is described in detail in [39].

The above formula is also valid for differential cross sections. The Lorentz-invariant cross section is calculated as:

$$\sigma^{inv} = E \frac{\mathrm{d}^3\sigma}{\mathrm{d}p^3} = \sigma_{trigger} E \frac{N_{obs}}{(\Delta p)^3}$$

[3]Generally there is a loss due to the trigger condition, which has to be corrected for, as it is discussed in Section 7.3

here N_{obs} is the number of particles over the reasonably small region of momentum space of $(\Delta p)^3$ volume.

The differential cross section can be expressed as a function of appropriate sets of kinematical variables. Two of the most common parameterizations are (x_F, p_T, ϕ) and (y, p_T, ϕ). p_T is the transverse momentum, the momentum component perpendicular to the axis defined by the beam particle. ϕ is the azimuthal angle around this axis. The Feynman-x variable x_F is the longitudinal momentum fraction of the particle compared to the maximum allowed momentum $x_F = p_L/p_L^{max}$ in the center of mass frame of the interaction. The rapidity y is defined as

$$y = \frac{1}{2} \ln \left(\frac{E + p_L}{E - p_L} \right)$$

Under Lorentz-boost in the longitudinal direction, the rapidity variable transforms additively.

The invariant differential cross section can be expressed in terms of these variables, assuming that the particle production is symmetric under rotations around the beam axis (independent of ϕ):

$$E\frac{\mathrm{d}^3\sigma}{\mathrm{d}p^3} = \frac{1}{2\pi}\frac{E}{p_T p_L^{max}}\frac{\mathrm{d}^2\sigma}{\mathrm{d}x_F \mathrm{d}p_T} = \frac{1}{2\pi p_T}\frac{\mathrm{d}^2\sigma}{\mathrm{d}y \mathrm{d}p_T}$$

In some cases it is convenient to restrict the double differential cross section (depending on e.g. x_F and p_T) to the longitudinal variable by integrating over p_T. Throughout of the present work, the *p_T-integrated number density* is defined as:

$$\frac{\mathrm{d}N}{\mathrm{d}x_F} = \frac{1}{\sigma^{inel}} \int \frac{\mathrm{d}^2\sigma}{\mathrm{d}x_F \mathrm{d}p_T} \mathrm{d}p_T$$

where σ^{inel} is the total inelastic cross section of the interaction. The number density has a simple meaning: the integral of the distribution is the mean number of particles produced in an inelastic event; for example, the baryon number conservation implies that the integral of the number densities for all baryons adds up to 2 in p+p interaction.

7.2 Full-target and Empty-target subtraction scheme

The ideal cross section measurement, as it was discussed in the previous section, involves a target irradiated by a beam of particles. In reality, the target is surrounded by the material of the target holder, the beam counters and the structural elements of the detector: the beam particles can initiate interactions in this extra material. In order to estimate the background, the "empty target" contribution is measured: the target is removed from the

target holder and data is taken with the same trigger setup. This contribution has to be subtracted from the data taken with "full target", and the difference gives the physics result corresponding to interactions in the real target volume (referred to as "hydrogen events").

From the point of view of the precision of the physics results, the method has two aspects:

- The *statistical significance* improves if the empty target contribution is reduced. This reduction can be achieved in the off-line analysis: the events which are corresponding more probably to empty-target contribution can be rejected.
- The rejection of events from interactions inside the target volume may cause bias. This can be corrected for, but the corresponding *systematic error* has to be carefully estimated if the rejection rate is not negligible [39].

The present work uses the conservative approach: the off-line rejection of empty target events *must not cause bias*, i.e. the hydrogen events are not allowed to be rejected. The full-empty target subtraction scheme involves a considerable amount of technical problems, which are discussed in detail in Appendix 1.

7.3 Correction for the trigger losses

The NA49 experiment applies a "bulls-eye" trigger for data taking with hadron beams: 4 m behind the target, a 2 cm diameter scintillator disk is placed in the path of the beam. The interaction is triggered if no charged particle hits the counter. The trigger setup accepts approximately 85% of the total inelastic cross section in case of p+p interactions; the major fraction of the 15% loss comes from the low multiplicity diffractive component with a fast proton (this proton hits the counter and the event is vetoed).

In the present work, a correction is applied for the trigger loss. The correction is evaluated by the off-line variation of the diameter of the interaction trigger counter: the measured cross sections exhibit a smooth dependence on the size, therefore an extrapolation to zero size is feasible. The correction amounts to about 5% on the particle yields at midrapidity and decreases fast in the forward region. The details of the procedure are presented in Appendix 1.

7.4 Feeddown correction

The track extrapolation has measurement uncertainty, therefore it is possible that such a track is assigned to the Main vertex which originates from a secondary vertex of a weak decay (Λ^0, K^0_S, $\Sigma^{\pm}$). In the bubble chamber experiments, the secondary vertices were

unambiguously resolved; in the counter experiments, all the weak decay products were accepted, since these detectors did not have primary vertex reconstruction. In both cases, the correction is to first order independent of the detector setup. The NA49 experiment has the property that the probability of finding a weak-decay track on primary vertex varies strongly in different regions of momentum space, therefore a precise estimate of the corresponding correction has to be determined.

The correction requires the knowledge of the yield and the distribution of the parent particle. For protons, the Λ^0 and Σ^+ particles contribute, for neutrons also the Σ^- has to be added up. The yield of Λ^0 particles are well measured (see e.g. [32] [33] [35] and an extensive discussion in [34]) in proton-proton interactions; the $\Sigma^{\pm}$ is much less known ([36] [37]). The following table shows the estimated total yields of the strange baryons contributing to proton, antiproton or neutron yields.

Particle	Λ^0	Σ^+	Σ^-	$\bar{\Lambda}^0$	$\bar{\Sigma}^-$
Yield / event	0.116	0.042	0.020	0.013	0.005

The x_F distribution of the Λ^0 particle is precisely known; for the Σ^+, a similar, but a little bit flatter distribution was suggested by [36]. The assumed distribution is shown in Figure 29. For the antibaryons, an x_F distribution was assumed which has a shape similar to that of the antiproton, as suggested by the measurements on the shape of $\bar{\Lambda}^0$ x_F distribution.

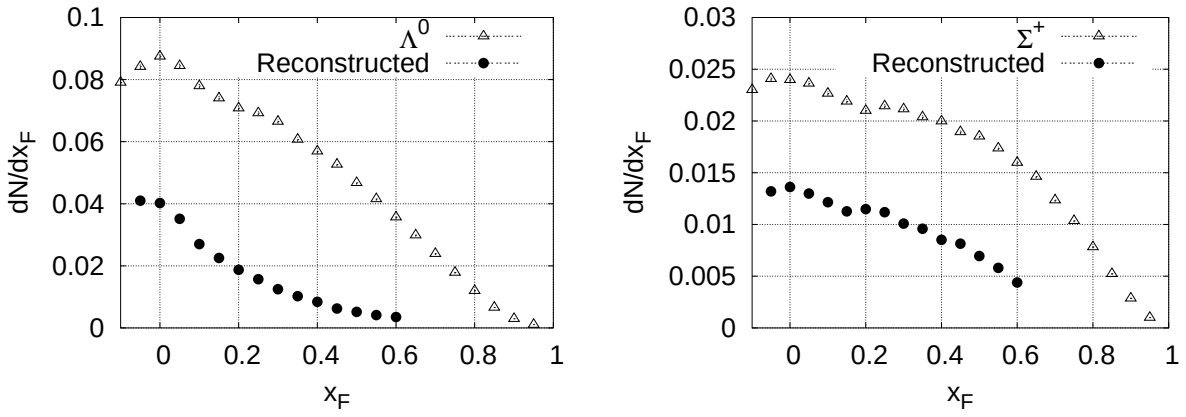

Figure 29: Estimated Λ^0 (left) and Σ^+ x_F (right) distributions, and the corresponding feeddown correction for protons

In the second step, the detection efficiency of the decay products is determined. The emitted particles are tracked through the GEANT simulation of the NA49 detector, and the correction is determined using the tracks reconstructed on Main vertex; the procedure was

performed by Michal Kreps and it is described in [38]. The reconstructed daughter proton distribution is also shown in Figure 29.

In case of the VPC+GTPC protons, a simplified, stand-alone Monte-Carlo was constructed by the Author, taking into account the geometry of the setup and the measured space resolution of the detector elements.

8. Results on particle spectra

In this chapter, a variety of results are presented on inclusive particle distributions in elementary interactions. This concerns mostly baryon production, protons and neutrons, whereas the pion production receives less weight. The basic motivation is the study of baryon number transfer: what experimental conclusions can be drawn by comparing different reactions, and whether it is possible to introduce and experimentally confirm an underlying physics picture.

In the first section, the proton results are presented along with a comparison to existing data in different energy ranges. In the following part the neutron results are shown and the experimental consistency is verified on the basis of the test of baryon number conservation. The conclusions of the comparison of pion and proton beam measurements will lead to the confirmation of a factorizing two component picture of baryon number transfer.

8.1 Results on protons in p+p

The complete set of measurements on differential cross section of proton production in p+p interactions is presented in Figure 30. The values are shown as a function of x_F, at different p_T values starting from 0.1GeV to 1.2GeV, as marked. The full dots correspond to the results from dE/dx identification, the empty circles are from the GTPC+VPC analysis. In the overlap region, the results are consistent within errors. It is important to note that in the GTPC+VPC analysis the particles are not identified, therefore the pion and kaon contamination had to be subtracted, which was estimated from the dE/dx analysis and from earlier measurements; this presents a systematic error. The contamination is about 20% at x_F=0.5 and decreases to 5% at x_F=0.7. The errorbars represent the combined statistical and estimated systematic errors. The overall normalization uncertainty presents an additional 4% error on the results.

The p_T integrated yield of protons in p+p interactions at 158GeV beam is presented in Figure 31. The distribution is flat to first order, with a strong diffractive peak above $x_F = 0.9$. There is a wide enhancement around $x_F = 0.4$, and a maximum at midrapidity ($x_F = 0$), which is a reflection of the antiproton distribution. The errorbars represent the statistical errors (including the uncertainties of the dE/dx extraction, as discussed in Section 3.); the systematic error is dominated by the overall normalization error. At high x_F (above 0.65) earlier measurements were used to extrapolate to low p_T where NA49 has no acceptance.

A number of earlier measurements are existing on proton production in p+p interactions in the energy range of the SPS. The measurements at different energies fall approximately

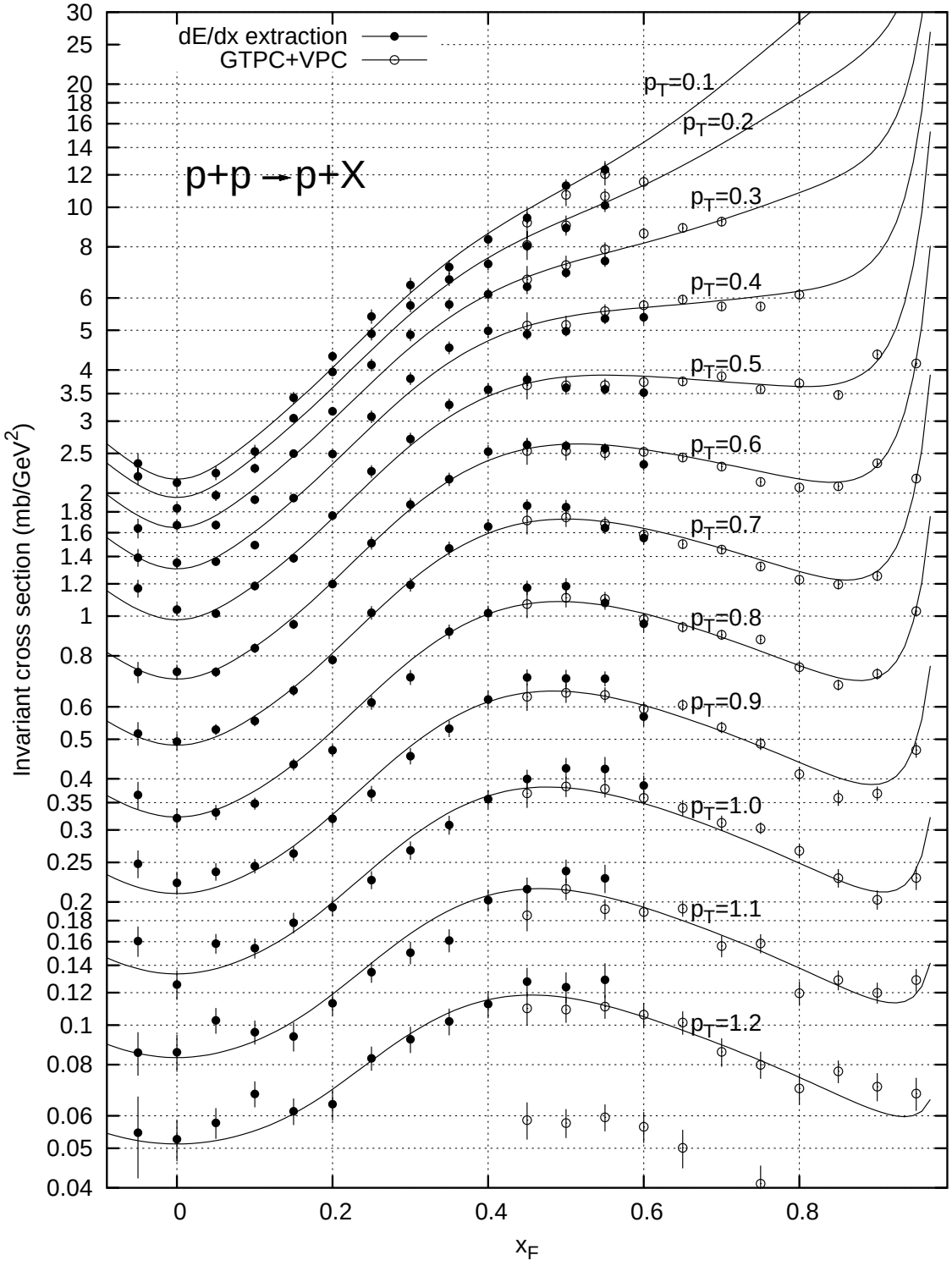

Figure 30: Complete set of measurements on proton production in p+p interactions, in bins of p_T from 0.1GeV to 1.2GeV. The lines are drawn to guide the eye.

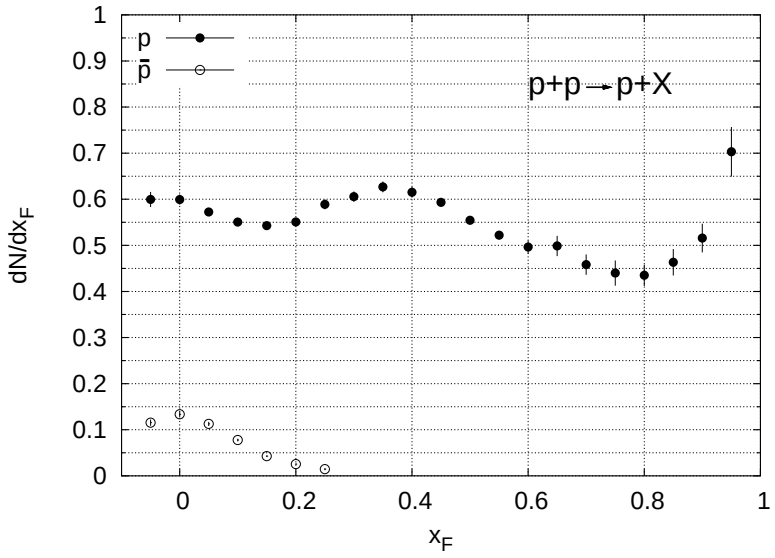

Figure 31: p_T integrated number density of protons and antiprotons in p+p interaction.

on the same curve as a function of x_F for $x_F > 0.3$, in coincidence with Feynman's scaling prediction [40]. A collection of these results is shown in Figure 32.

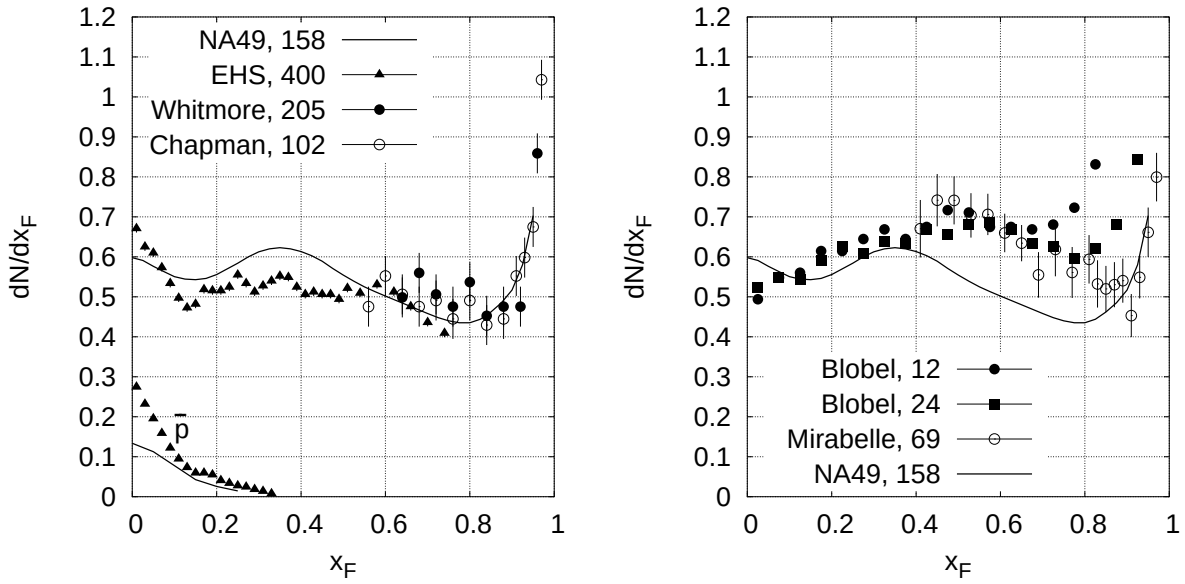

Figure 32: Comparison of the proton x_F distribution with earlier measurements. The beam energy in GeV is marked after each experiment. The line shown is the NA49 measurement from Figure 31.

The NAL 30-inch bubble chamber was exposed to 102 and 205 GeV (and later also 300 and 400 GeV) proton beam. The measurements have a full coverage over the whole p_T range,

therefore a reliable integrated yield can be extracted in the high x_F range of $x_F > 0.6$ using the bubble density for particle identification. The results (Chapman [42] and Whitmore [41]) has some overlap with the NA49 measurement, and the data are consistent with each other within the large statistical errors.

The measurements from the European Hybrid Spectrometer (EHS) [5] cover the x_F range from 0 to 0.7, at a beam energy of 400 GeV. The spectrometer setup is built up from proportional chambers and Cherenkov counters for particle identification. The errors on the datapoints are purely statistical, and no estimate is given concerning the systematic errors. The total trigger cross section of the experiment was 25.5 mb, which is about 20% smaller than the total inelastic p+p cross section, and a correction via weight factors are introduced, depending on the measured charged particle multiplicity. The results are slightly below the NA49 results, except for the $x_F < 0.1$ region: close to the center, the proton density is higher due to the increased baryon pair production at higher beam energy. The increased antiproton production is also shown in Figure 32.

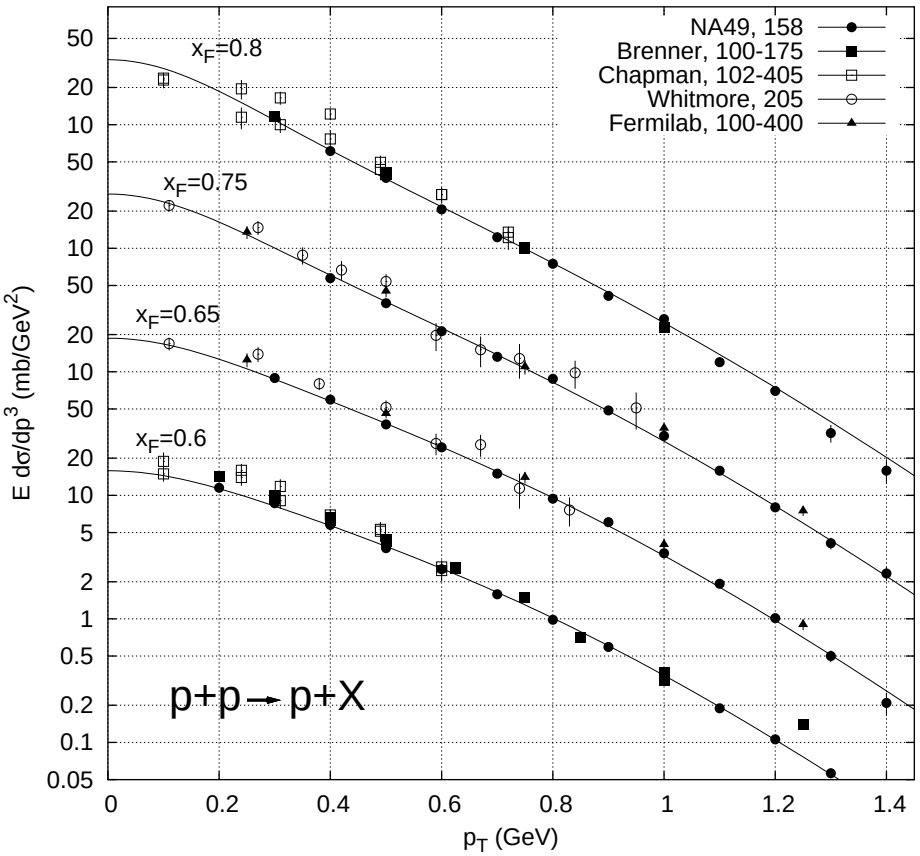

Figure 33: Comparison of the proton invariant cross section with earlier measurements: p_T dependence at fixed values of x_F.

A further comparison to earlier measurements is shown in Figure 33, namely the p_T dependence of the differential cross section at fixed values of x_F. Besides the experiments mentioned above, datasets from two spectrometer detectors are shown.

Brenner et al. [43] at the Fermilab Single Arm Spectrometer measured p+p interactions at 100 and 175 GeV beam. The datapoints are generally higher than the NA49 measurements by about 10%. In the publication, the authors present a p_T integrated yield, but the assumed simple exponential or Gaussian p_T shape does not describe the actual curve (which is more like Gaussian at low p_T and becomes exponential at higher p_T), therefore the published integrated yields were disregarded at the comparison.

An other experiment at Fermilab (Johnson [44]) measured p+p interactions at beam energies of 100, 200 and 400 GeV. The datapoints shown in Figure 33 are the average of the results from the three energies: the averaging can be performed under the assumption of Feynman scaling, which, as it was mentioned, predicts an energy-independent cross section as a function of x_F.

The above comparison has shown, that the NA49 results are compatible with the existing measurements, and the comparison of the results from different energies show that the Feynman-scaling is valid for the SPS energy range. The approach towards the scaling can be studied in a comparison with lower beam energies: measurements at 12 and 24 GeV (Blobel [1]), shown in the right panel of Figure 32, fall higher than the NA49 results. The scaling limit is therefore approached from above.

The Mirabelle bubble chamber [3] at the Serpukhov accelerator operated at 69 GeV beam energy. The proton spectra is again slightly higher than the NA49 results at 158 GeV, which is partially due to energy dependence, and partially due to measurement uncertainty. Unlike the NAL results, the identified particle yields were extracted with a sophisticated Monte-Carlo-based method relying on the forward-backward symmetry of the collision, where the measured asymmetry in the laboratory frame appears due to the particle mass.

Measurements on proton production were performed at the ISR (Albrow [45] [46]) at $\sqrt{s}$ between 23 and 63 GeV, and the results revealed the s independence (scaling) in this range. The measured cross sections are comparable to that from NA49 (see Figure 34). Generally one can conclude that the proton production shows a scaling behaviour in the range of SPS energies and above. The ISR yield is on average higher than the NA49 result by about 10%, which can be systematic uncertainty, but can also be an image of the increased p+p total cross section: experimentally it is not clear, whether the invariant cross section, or the integrated yield (i.e. the production cross section divided by the *total cross section*) is the Feynman-scaling quantity[4].

[4]The baryon number conservation naturally suggests that the yield is invariant, otherwise the central

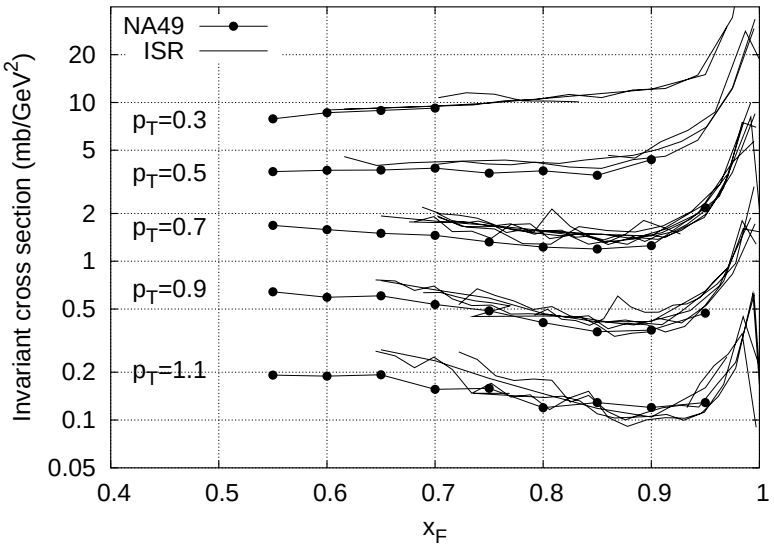

Figure 34: The NA49 proton cross section compared to ISR results: the ISR measurements range from $\sqrt{s}$=23 to 63 GeV. The data points are connected with lines.

In conclusion, what NA49 gained over the previous measurements are precise data with controlled systematic errors, and the dense and nearly complete coverage of the momentum space within the same detector.

8.2 Neutron production in p+p

The x_F distribution of neutrons is shown in Figure 35. The distribution steepens up compared to the flat distribution of protons and does not have a diffractive peak (which, if it existed, could still be resolved with the Calorimeter).

The Figure shows the comparison of the shape of the neutron and Λ^0 x_F distribution (the Λ^0 distribution is extensively discussed in [34]), where the Λ^0 distribution is scaled up so that it is equal to the neutron distribution at x_F=0.4. The Λ^0 distribution is considerably steeper, which can be explained by the difference in the production mechanism: fast neutrons can be created via the low mass diffraction from an excited nucleon, whereas Λ^0 must appear together with an associated kaon, which increases threshold for the corresponding excitation.

In the energy range of the SPS, two earlier measurements are existing on neutron production in p+p interactions, a fixed target spectrometer experiment at 400 GeV beam at

yield should increase to balance the increased total cross section. This expectation is supported by the fact that the total p+p cross section increases by about 10% between SPS and ISR energies, as does the measured cross section. On the other hand, results form the SPS Collider [47] indicate that the invariant cross section is constant.

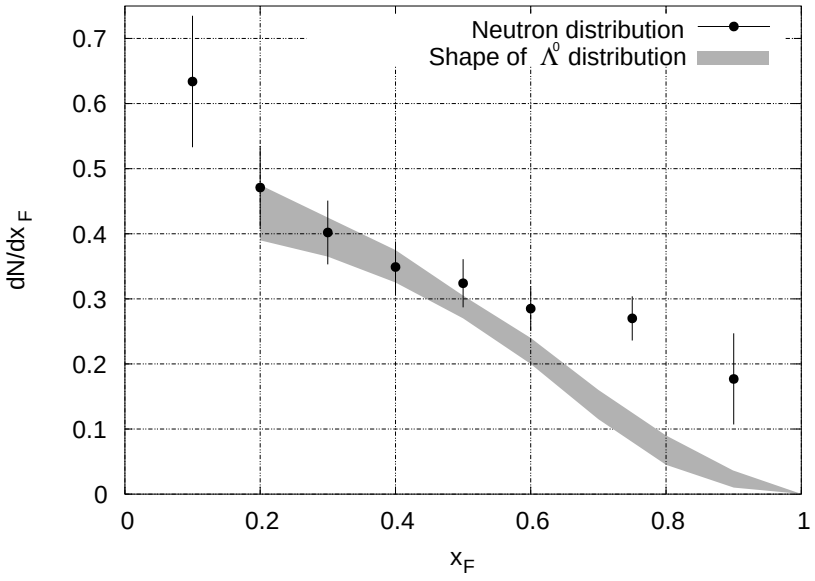

Figure 35: Neutron spectra in p+p interaction. The result is compared to the shape of the Λ^0 distribution

Fermilab [48] and a measurement from the ISR [49]. The comparison to the NA49 results is shown in the left panel of Figure 36.

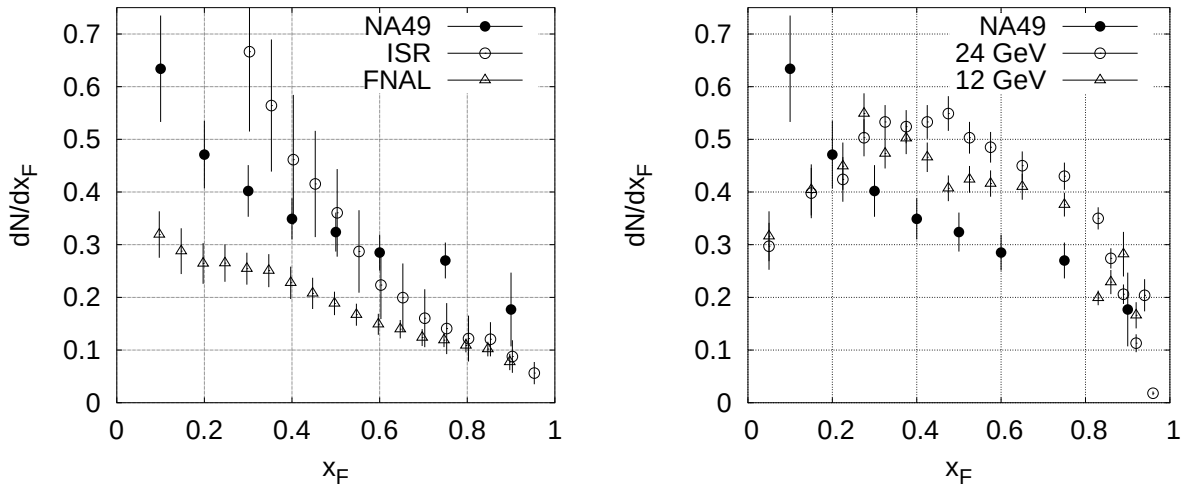

Figure 36: Neutron distribution, compared to earlier measurements

The ISR measurement suggests a steep x_F distribution for the neutrons. The total integrated yield is considerably larger than the NA49 yield, indicating difficulties with baryon number conservation. Concerning the p_T shape, according to the results the mean p_T of

neutrons would be much smaller than that of protons, which means that the neutrons would behave differently from all the other baryons (proton, Λ^0 and cascade [34]). The neutron spectra at p_T=0 were measured with a refined experimental setup [50], where the same authors remark that the original results could be affected by secondary interactions in the ISR beampipe: the interactions reduce the mean neutron momentum and therefore the distribution steepens up.

The x_F shape of the Fermilab measurement is similar to the NA49 result, but the measured yield falls much below: the total yield would again contradict the baryon number conservation. This measurement suggests that protons and neutrons have a similar p_T distribution.

At lower beam momentum, neutron yield extracted from bubble chamber measurements exist [32] at 12 and 24 GeV. The comparison to the NA49 result is shown in the right panel of Figure 36. The shape is similar, but the yield above x_F=0.3 is higher, which corresponds to the proton behaviour: Feynman scaling is approached from above. The slight increase of the total yield can be partially attributed to the lack of strange baryons at low energy (larger amount of the baryon number has to be carried by neutrons).

In conclusion, the earlier measurements on neutron production are contradictory in the SPS energy range, and the NA49 results can not confirm any of them. In this situation, an experimental consistency check of the present result is crucial. The actual consistency was tested in three independent ways: on one hand, the total momentum carried by neutrons (neutral particles) and charged particles sum up closely to the beam momentum, as it was shown in Figure 11.

On the other hand, the reactions p+p→n+X and p+n→p+X can be compared (also discussed in [51]), where the production cross section should be the same due to isospin symmetry. The result is shown in Figure 37, which confirms the expectation[5].

A further check of consistency is the experimental test of *baryon number conservation*, which restricts the total yield of the baryons. This question will be discussed in the following chapter.

8.3 Experimental check of the baryon number conservation

The conservation of baryon number in hadronic interactions is a prediction of QCD, following from the quark confinement. The experimental test requires precise measurement of the total yields of all baryons, which was not feasible up to now due to the large systematic errors. The NA49 experiment has a number of advantages which make it well suited for

[5]Neutron beam was produced from a deuteron beam with proton spectator tagging: d+p→X+(spectator proton) is interpreted as n+p interaction. The experimental method is described in [52].

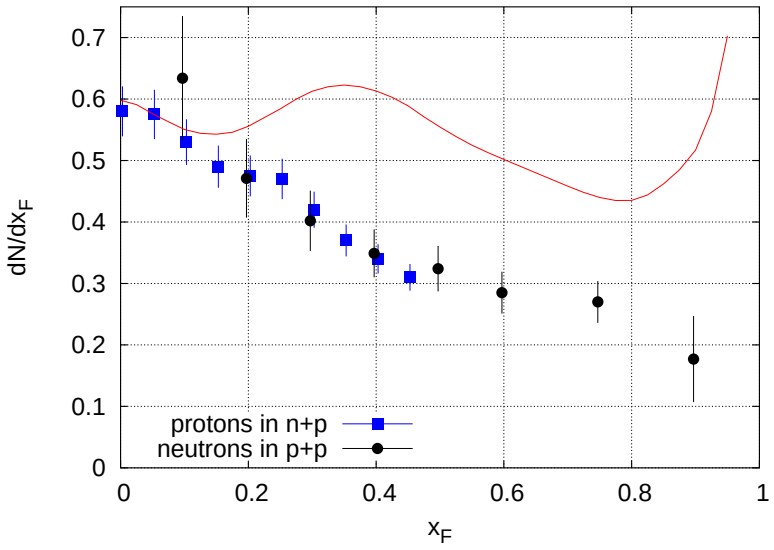

Figure 37: Comparison of the neutron yield from p+p and the proton yield from n+p interactions (the continuous line shows the proton distribution)

the study of baryon number conservation: particle identification over a large momentum space, hermeticity, neutron detection, and all the measurements being done at the same experiment, which considerably reduces the systematic errors.

The total yields of baryons and antibaryons in the forward hemisphere in p+p interactions are presented in the following table:

Particle type	yield
proton	0.582 ± 0.03
neutron	0.370 ± 0.045
Λ^0	0.058 ± 0.007
Σ^+	0.021 ± 0.004
Σ^-	0.010 ± 0.005
$\bar{p}$	0.018 ± 0.003
$\bar{n}$	0.022 ± 0.005
$\bar{\Lambda}^0 + \bar{\Sigma}^{\pm}$	0.010 ± 0.004
Sum:	$\mathbf{0.991 \pm 0.061}$

The majority of baryon number is contained in the non-strange baryons, proton and neutron, which are both measured at the NA49 experiment. The most frequent strange baryon, the Λ^0 is also measured at NA49 ([53], [34]); for the sigma baryons, assumptions had to be made in order to extrapolate the yield to our energy range (see the discussion in

Chapter 7.). Since the total yield of strange baryons is less than 10% of the total baryon yield, the error of the sum is still dominated by the proton and the neutron uncertainty.

The antibaryons, subtracted from the baryon yield, amounts to about 5% of the total yield, therefore the corresponding error contribution is very small. The estimate on the anti-neutron yield is discussed in [27] [54].

The sum, within error, confirms the baryon number conservation, and at the same time, confirms the consistency of the extracted yields.

8.4 Comparison of pion and proton beams: factorization of baryon production

In the previous sections, the basic features of baryon production in elementary interactions were discussed. The aim of the further studies is to get insight to the properties of baryon number transfer: how does the baryon number of the projectile translate to the baryon density of the final state?

The comparison of protons from n+p interaction and neutrons from p+p interaction provides the first hint: in the forward region, due to isospin symmetry, the yields are the same (as it was discussed in connection with Figure 37). In fact, this isospin argument is correct under the strong assumption, that *isospin symmetry holds separately for the forward hemisphere:* the isospin rotation of $p + p \to n$ is $n + n \to p$. In other words, the production on the forward region depends only on the projectile, and not on the target

The independence of the particle production from the target type in the projectile fragmentation region is predicted both by Regge calculus (see e.g. [6] [55]) and parton models [7], and is usually referred to as factorization of the two hemispheres. Tentatively this picture can be extended to the central region, assuming that the baryon number density has two components, associated to the target and the projectile. This scenario is illustrated in the left panel of Figure 38, where the net proton density $(p - \bar{p})$ in p+p is separated to two (at the moment, hypothetical) components.

The factorization assumption suggests that using *baryon number free* projectile, the target component can be measured, as illustrated in the right panel of Figure 38. The consistency of the factorizing two component picture suggest two predictions for the ratio of the proton density measured in π+p and p+p:

- In the backward region, the ratio has to approach 1
- By symmetry, the ratio must be 1/2 in the center, x_F=0

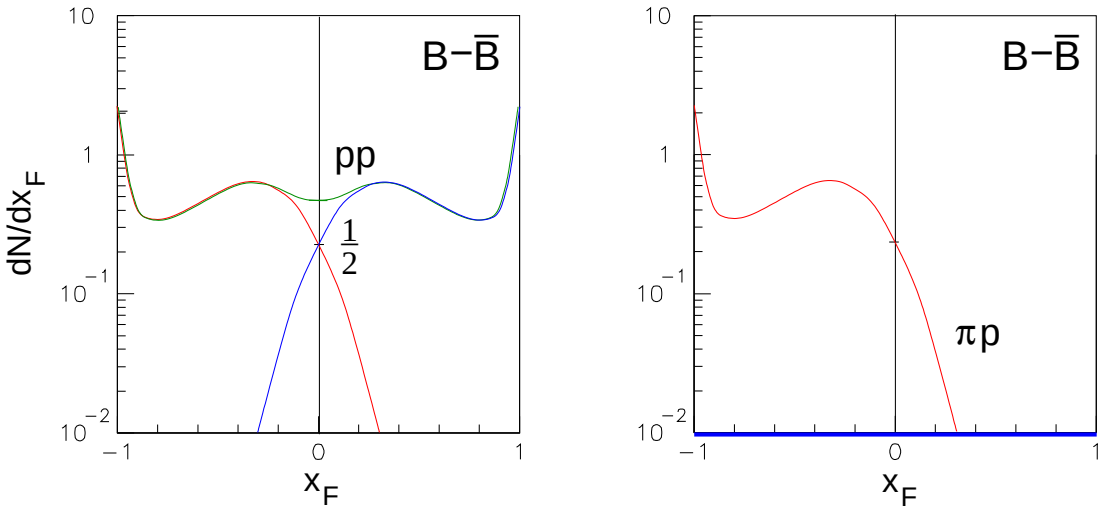

Figure 38: Two component picture: the target and projectile component of the proton density in p+p interactions (left) can be separated by the measurement of the proton density in π+p collisions (right).

The ratio of the proton density measured in isospin averaged π+p and p+p interactions is shown in Figure 39. The predictions mentioned above are fulfilled within errors. In the backward region, the NA49 results are complemented with bubble chamber measurements on π^++p reaction (Azhinenko [56], Whitmore [2]).

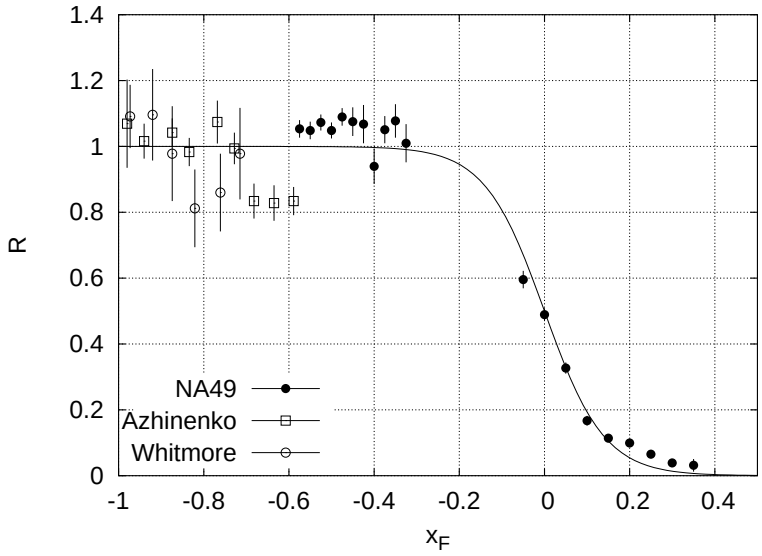

Figure 39: Ratio of proton density, measured with pion and proton beam.

The conclusions of this experimental study can be summarized as follows:

- The baryon number transfer is built up from two factorizing components, associated to target and projectile. This is supported by the independence of the target component from projectile isospin and particle type.

- The two components overlap in the center. The feedover from the target component rapidly approaches zero in the forward hemisphere, decreasing by a factor of three at x_F=0.1. These measurements limit the transfer of baryon number to about 4.5 units in rapidity (1.5 units backward, up to x_F=0.25) in p+p collisions, and gives constraint on theoretical models, e.g. the junction picture [11][6].

8.5 Results on charged pions in p+p

In the previous sections the results on baryon production were presented. Further detailed studies of baryon production mechanisms will reveal a strong connection between baryon and meson production: this chapter aims to provide a compilation of the inclusive particle distribution results with the measurement on charged pion production.

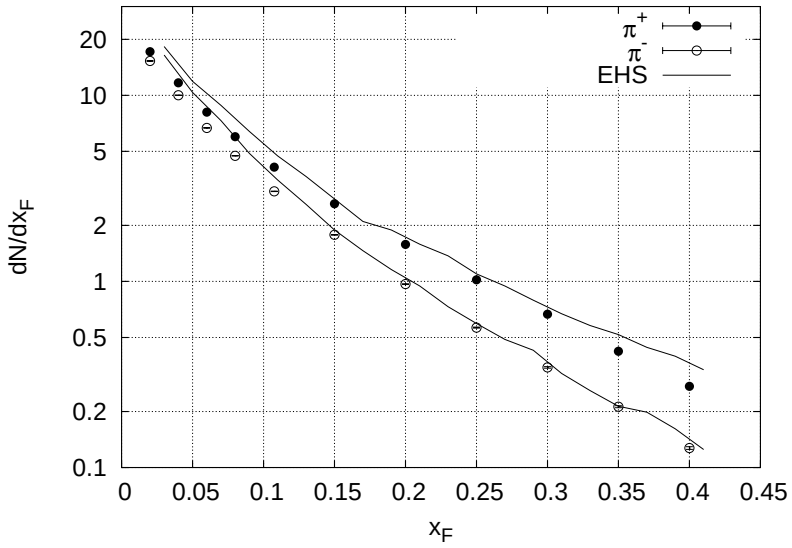

Figure 40: p_T integrated yield of charged pions in p+p interaction

The p_T integrated number density of the charged pions in p+p interactions at 158 GeV

[6]The junction picture of Ref [11] predicts a flat projectile baryon distribution in rapidity for double stopping process and exp($-y/2$) for single baryon stopping process; the above discussed result favours a more steep, exp($-y$) or even steeper distribution (x_F=0.1 means y≈0.8). One has to note however, that the junction picture is valid for very high $\sqrt{s}$, and the SPS energy range may not yet show the asymptotic behaviour.

beam is shown in Figure 40. As a function of x_F, the yield is steeply falling, π^- is steeper than π^+.

Figure 40 shows a comparison to EHS [5] measurements. The EHS data is taken at 400 GeV beam energy, and the increase of the yield at low x_F can be due to energy dependence (the Feynman-scaling holds also for pions in the high x_F regions, whereas the central area shows a steady increase with $\sqrt{s}$).

The differential cross section for π^- at fixed p_T values of 0.2, 0.4 and 0.8 GeV is shown in Figure 41, compared to earlier bubble chamber measurements (Mirabelle [3], Whitmore [2]). In the bubble chamber, the majority of negative particles are pions; the estimated K^- and antiproton contribution can be subtracted, which presents additional uncertainty. The results from NA49 are consistent with these measurements.

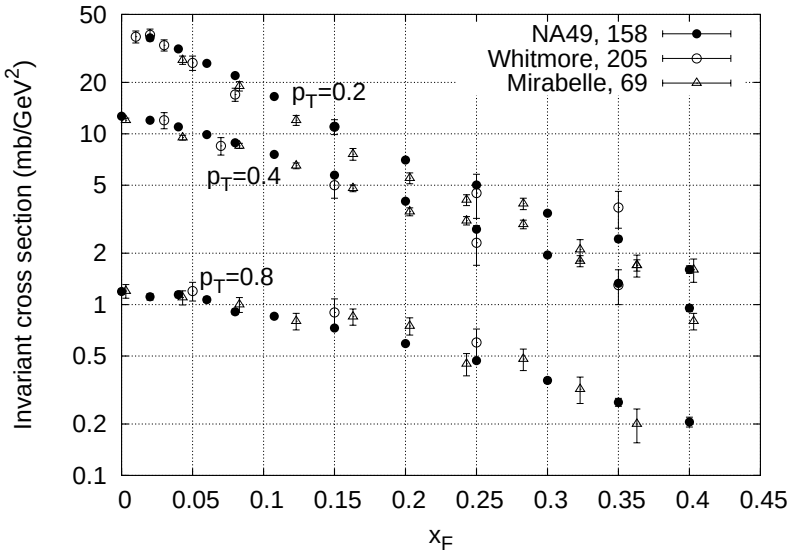

Figure 41: Comparison of the negative pion production to earlier measurements: x_F distribution at fixed p_T of 0.2, 0.4 and 0.8 GeV.

9. Results on correlations with final state baryons

9.1 Introduction

In the previous chapter, the results on inclusive particle distributions were discussed, which revealed the factorization of the baryon transfer in the two hemispheres. The conclusions restrict the possible model predictions, but still a variety of the phenomenological models are able to describe the actual data. In order to distinguish between these model predictions, one has to go beyond the inclusive surface: since the particle correlations contain a lot more information, they provide a tool to get a deeper insight in the particle production mechanisms.

In this chapter, the results on correlations with the final state baryon are presented. The basic motivation is again the study of baryon transfer, from the point of view of correlations.

A number of previous measurements studied correlations in general, which may be divided into two groups: short- and long-range correlations. Strong short range (in rapidity, within 2–3 units) correlations are present in the central region of hadronic interactions, predicted by different theoretical models (e.g. the multiperipheral model), but which can not be distinguished from resonance formation. On the other hand, the long range correlations are found to be weak.

A measurement of long range correlations was preformed at the ISR [57]. The results from this double arm spectrometer have shown that the two hemispheres are (statistically) independent at high momentum (for protons x_F >0.4, for pions x_F >0.2), except for the diffractive region (x_F >0.95 for protons). An example of the observed correlation is shown in Figure 42, demonstrating that the factorization of the two hemispheres holds for the regions mentioned above.

On the other hand, bubble chamber measurements [58] [41] suggest that besides the weak correlation between the opposite hemispheres, there is a strong correlation between particles on the same side, shown in Figure 43.

NA49 offers the possibility to study these correlations over a wide range of momentum space with high statistics and particle identification.

A short summary of the basic notations and definitions to be used throughout the chapter will be given in the rest of this section.

Similarly to the inclusive (non-invariant) differential density of particle A, defined as

$$\rho_A = \frac{1}{\sigma_{\text{inel}}} \frac{\mathrm{d}^3\sigma}{\mathrm{d}p_A^3}$$

the double-inclusive differential density for particles A and B can be defined:

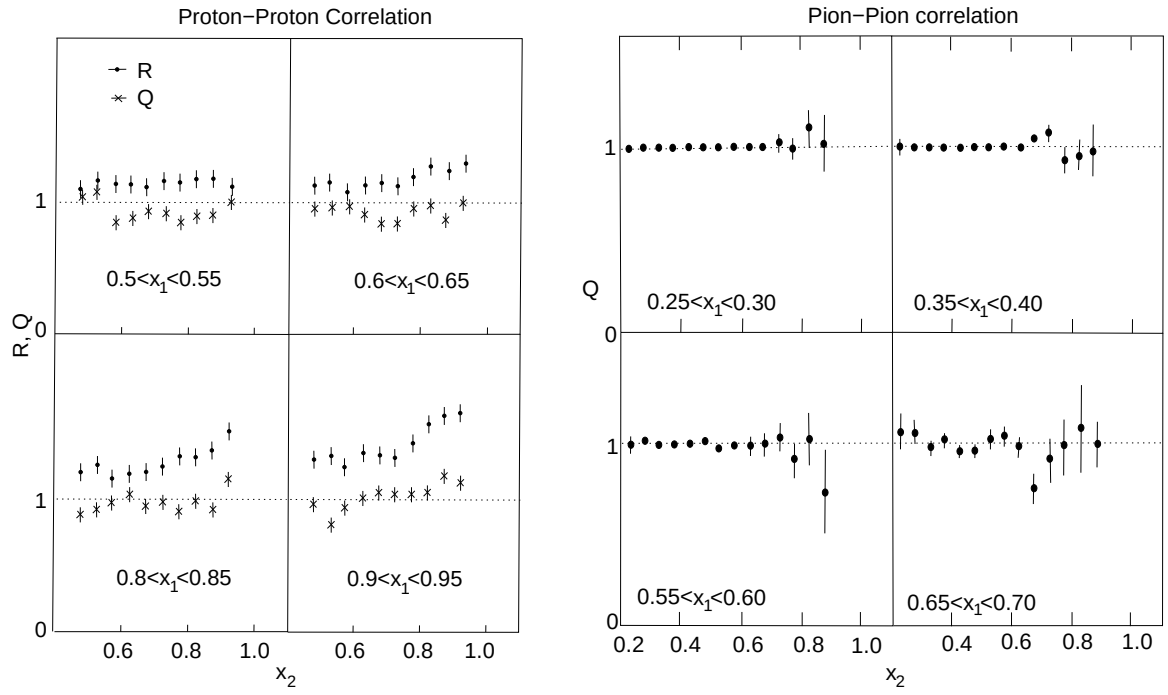

Figure 42: Correlations between the two hemispheres at the ISR in p+p interactions from [57]. The x_F of the trigger particle is x_1, the correlated particle is at x_2. The correlation ratio (R) and the correlation quotient (Q) (both defined in this section) are constant and close to unity, demonstrating that the two hemispheres are independent.

$$\rho_{AB} = \frac{1}{\sigma_{\text{inel}}} \frac{\mathrm{d}^6\sigma}{\mathrm{d}p_A^3 \mathrm{d}p_B^3}$$

where ρ_{AB} depends on the x_F and p_T of the two particles and the difference of the azimuthal angles, $\Delta\phi$ (usually the two p_T and the $\Delta\phi$ variables are integrated over). σ_{inel} is the total inelastic p+p cross section. One of the particles is denoted as "trigger" particle, the one with which the correlation is studied. The other particle is the "correlated" particle.

Instead of the inconvenient ρ_{AB}, the *correlated yield* will be used, defined as the ratio of the double-inclusive density and the inclusive density of the trigger particle:

$$\rho_B^{corr} = \frac{\rho_{AB}}{\rho_A}$$

which can be viewed as the density of the correlated particle, restricted to the event sample with a trigger particle present. Experimentally, the ratio of the correlated yield and the inclusive density of the correlated particle is easily accessible; this *correlation ratio* is defined as:

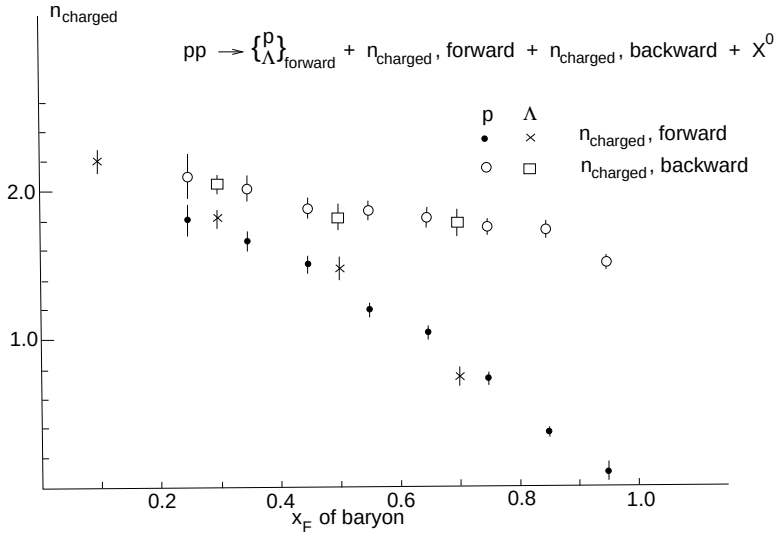

Figure 43: Forward and backward charged multiplicity, associated to a forward proton or Λ^0 in p+p interactions at 19 GeV beam, from [58]. The forward multiplicity is strongly correlated, whereas the backward is closely independent.

$$R = \frac{\rho_B^{corr}}{\rho_B} = \frac{\rho_{AB}}{\rho_A \rho_B}$$

In Figure 42 besides R the correlation quotient, Q is also mentioned. The difference between Q and R is that in Q the densities are normalized to the trigger cross section instead of σ_{inel}.

In the following discussions, the terms *forward* and *backward* will refer to the $x_F > 0$ and $x_F < 0$ regions, respectively. On the other hand, the terms *projectile* and *target* will be used in the context of the two component picture: due to the feedover, some fraction of the projectile component will appear in the backward region.

9.2 Experimental and conceptual problems

The correlation measurements have a number of complications at a counter experiment, including acceptance and identification corrections. The single-inclusive distribution for any particle depends only on two variables, since the collision is symmetric under the rotations around the azimuthal angle. For the double-inclusive distributions, the function has five variables, and the dependence on the relative azimuthal angle complicates the acceptance treatment. An example is the problem of "acceptance holes": at a given relative angle value, there may be no acceptance for the double-inclusive measurement, in a region where the single-inclusive distribution of both particles can be measured. On the other hand, the

presentation of the data requires the integration over two or three of these variables. In the presence of acceptance holes, *assumptions* has to be made for the shape of the correlated distribution.

In the present work, the following assumption is made[7]: the correlated yield at a given x_F, p_T of the trigger particle, and x'_F of the correlated particle can be parametrized as:

$$\rho^{corr}(p'_x, p'_y) = R\rho^{inclusive}(p'_x + T, p'_y)$$

where p'_x and p'_y are the components of the p'_T (transverse momentum) of the correlated particle such that p'_x points in the direction of the trigger particle. The complete correlated distribution is described by two parameters, R and T (both depending on three variables). This assumption means that the shape of the correlated density distribution does not change, but it is scaled up (by R) and transversally shifted against the trigger particle (by T) compared to the inclusive distribution.

Under this assumption, the complicated acceptance correction and the correction for particle identification losses can be treated using the *event mixing technique*. By this method, the correlation ratio (ratio of the correlated density and the single-inclusive density) can be obtained directly, corresponding to the R parameter. The technique is discussed in detail in Appendix 2.

Besides the experimental complications, the correlation studies with baryons has conceptual problems. Close to the center, the presence of pair produced baryons (protons) distort the correlation with the final state net proton. This can be circumvented by measuring the correlation with antiprotons, under the strong assumption, that *the antiproton measures the pair produced proton*. In fact, this is *not* true: the pair production process in a p+p collision is asymmetric [51] [54], preferring the $p\bar{n}$ pairs against the $n\bar{p}$ pairs, therefore the number of pair produced protons is higher than the number of antiprotons. Nevertheless, to first order the correlation with the net proton can be measured by the difference of the double-inclusive yields correlated with proton and antiproton, as it is defined in the following studies.

A further conceptual problem in the central region is the presence of feed-over: the trigger baryon can come either from the target or the projectile, therefore the measured correlation is the mixture of the correlation associated to the target and projectile. In the study of the correlated pion multiplicity, an attempt will be made to clean up this ambiguous region.

[7]The studies has shown that the final result is rather insensitive to the actual assumption, due to the high acceptance of the experiment: the simplest assumption, namely the independence from the relative azimuthal angle, leads to the same physics conclusions.

9.3 Correlation between baryons

The two component picture, as discussed in the previous chapter, assumes the factorization of the produced net baryons in the two hemispheres. This picture suggests, that if in a p+p interaction, the proton is fixed in the forward region, the remaining net proton density corresponds to the target component. The idea is illustrated in Figure 44.

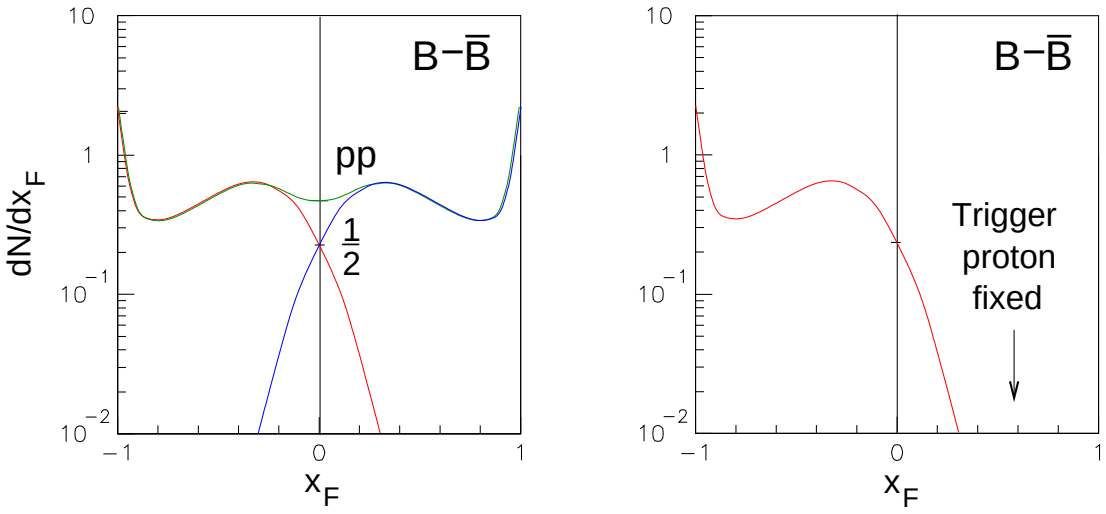

Figure 44: Two component picture: the components of the net proton density (left) can be separated by measuring the correlation between the final state baryons: fixing a proton, the remaining proton density corresponds the target component (right)

Similarly to the argument with pion beams, the two component picture predicts the following features of the density ratio, measured in p+p, comparing the yield with a fixed forward proton and the inclusive reaction:

- In the backward region, the ratio must approach 1.
- The density ratio must be 1/2 in the center by symmetry.
- The measured density ratio must be independent of the position of the forward proton (provided that it is not a pair produced proton, or that it is not from the feedover of the target component).
- The approach of fixing a proton in the final state, or using baryon free projectile must be consistent: the measured target component must be the same as the result of the study of pion beams.

Experimentally, fixing a forward or backward proton involves different regions of the detector, proton tracks with total momentum spanning a range of more than two orders of magnitude. For this reason, the correlation with protons from the two regions are discussed separately. In Figure 45 the density ratio of the correlated and uncorrelated (inclusive) yield of protons is shown, where the correlated yield is measured under the requirement of the presence of a backward proton in the event.

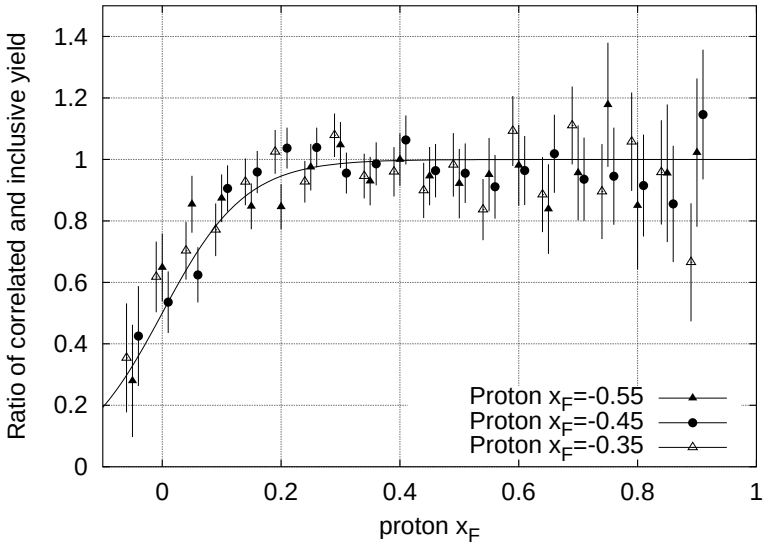

Figure 45: Ratio of the correlated net proton density and the inclusive net proton density, with a fixed backward proton in the x_F regions indicated.

The measurement shows, that within the statistical error on the level of 5-10%, the forward yield is independent of the position of the backward proton, therefore the third prediction is fulfilled. In the center, the ratio passes through 1/2 within errors, and is close to 1 forwards.

The forward proton density correlated with a forward proton is shown in Figure 46. The measured ratio is again 1/2 in the center. The statistical errors are smaller than in the case of backward proton trigger, and even within these limits, the ratio is independent of the trigger position up to x_F=0.8. In the last x_F bin of the trigger proton, x_F=0.85, the yield must depart from the predicted invariance due to energy conservation, but even then, the target component contributes to the yield in the center.

In conclusion, the factorizing two component picture provides an experimentally consistent picture of baryon number transfer. The observations from the pion beam studies can be completed with the following point: the two components are (statistically) independent in the complete momentum space, except for the diffractive region. This also means, that

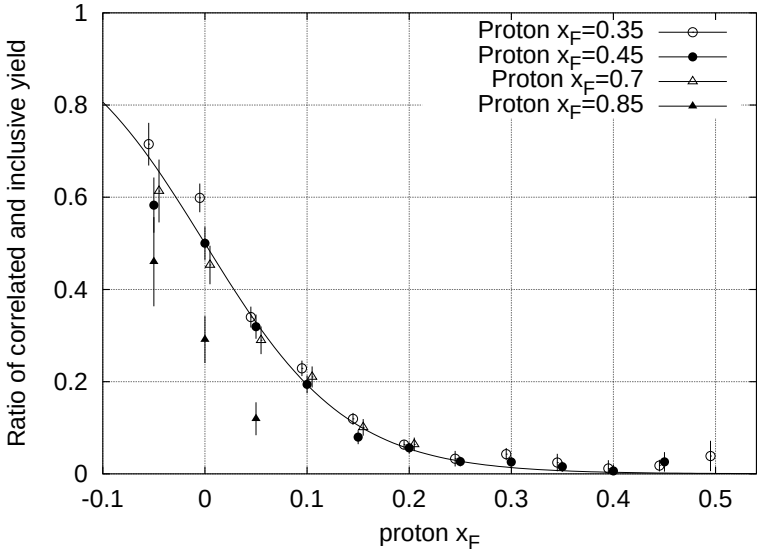

Figure 46: Ratio of the correlated net proton density and the inclusive net proton density, with a fixed forward proton in the x_F regions indicated.

from the point of view of correlations, experimentally there is no difference between the baryons in the center and the baryons in the fragmentation region (e.g. x_F >0.3).

9.4 Associated pion multiplicity

In the previous chapter the correlations between final state baryons were discussed. Now we further proceed with the study of correlations of pions, the most abundantly produced particles, with baryons. The two component picture, which proved to be fruitful for the understanding of baryon number transfer, runs into difficulties with pions: the baryon number conservation, which allowed to separate the components of net protons, does not have an analogy for mesons. On the other hand, as it was discussed in the previous chapter, the two component picture provides definite predictions for the correlations, therefore the possible inconsistencies with this picture can be revealed.

The first observable is the evolution of the pion multiplicity with the baryon transfer. In Figure 47, the forward pion yield (integrated above x_F=0.01 due to experimental reasons) is shown as a function of the x_F of the final state proton (or proton minus antiproton in the right panel).

The correlation with the net proton, defined here as proton minus antiproton ($p - \bar{p}$) as mentioned among the conceptual problems, is measured in two steps: first the correlation is determined separately with the proton and the antiproton, and then the correlated densities are subtracted properly.

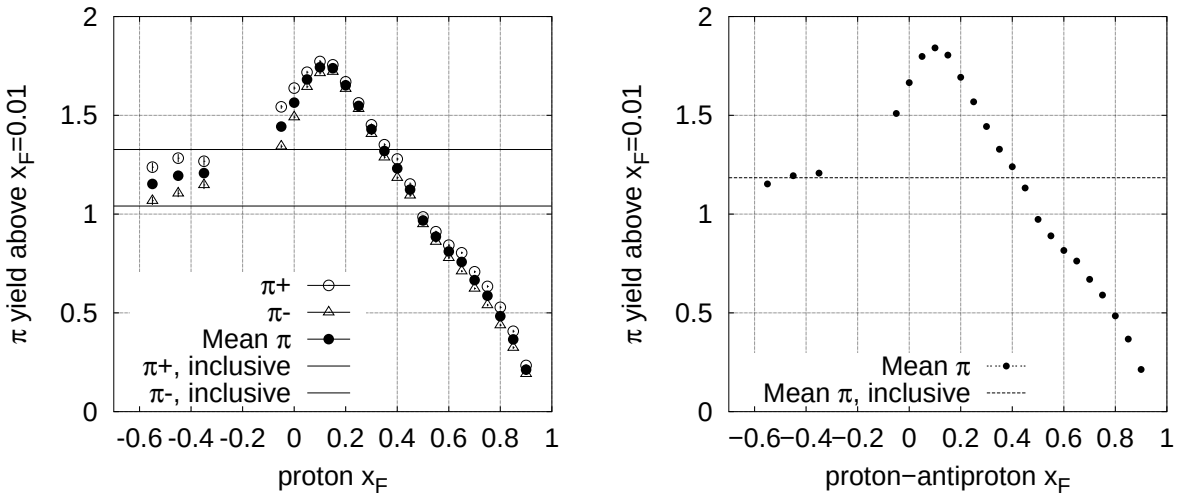

Figure 47: Forward pion yield integrated above $x_F = 0.01$ as a function of the x_F of the final state proton. In the left panel, the two charges (and also the mean) are shown separately. In the right panel, the mean pion multiplicity is shown associated with the x_F of the *net proton* (proton - antiproton).

The main features of this associated pion multiplicity, concluded from Figure 47, are the following:

- There is a strong, to first order linear dependence of the forward pion yield on the x_F of the final state forward proton in the range of 0.2 to 0.8: the yield is lower at high x_F of the proton. This follows the expectation: if the baryon is slow, the energy stored in produced particles must increase, therefore it is natural to expect the increase of multiplicity.

- There is weak dependence of the forward yield on the x_F of the backward proton: the change is less than 3% in the region (-0.55 to -0.35) where there is a 50% change in the other hemisphere.

- In the backward region, the $\pi^+ - \pi^-$ difference approaches the difference of the inclusive yields, also supporting the statement of independence.

- In the forward region, the π^+ is closely equal to π^-, which means that the charge is conserved within the hemisphere of the trigger proton (the total one unit charge is taken up by the proton).

These observations are compatible with the two component picture. It is important to note, that the weak dependence of the forward yield on the backward proton x_F implies, that

the *feedover for pions is small*. Within the two component picture, the measured forward yield receives a contribution from the target component, which is strongly correlated to the backward proton (following the first point of observation), therefore the weak dependence can only be explained by a small target contribution.

The difference between the forward π^+ and π^- yield is small in correlation with a forward proton, indicating charge conservation separately for the forward hemisphere. As a consequence, the difference must be large in correlation with a forward neutron: this effect is demonstrated in Figure 48.

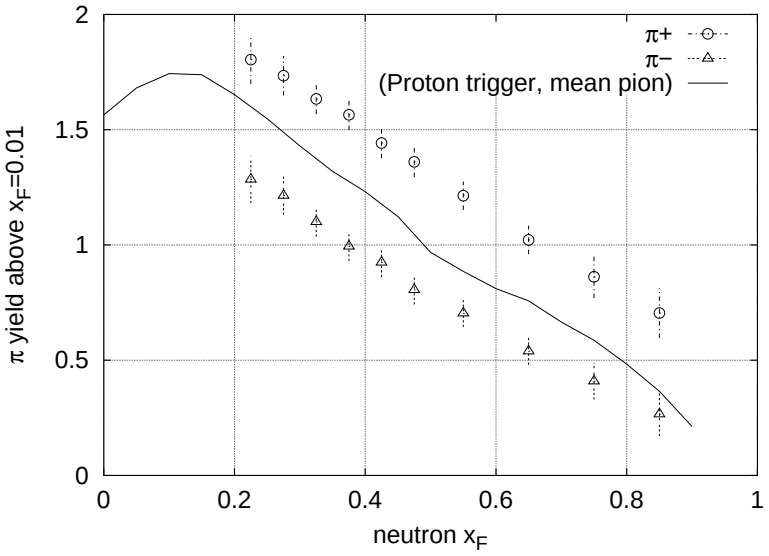

Figure 48: Correlation with neutron: Forward pion yield integrated above $x_F = 0.01$ as a function of the x_F of the final state neutron

The difference of the π^+ and π^- is approximately constant, 0.5 unit. Naively one would expect a difference of 1, which in reality decreases due to a number of reasons. The pion yield is integrated above x_F=0.01, and approximately 20% of the total yield is below this limit due to the steepness of the x_F distribution. A certain fraction of the charge is taken up by charged kaons, and due to the Λ-K^+ associated production, the K^+ has a higher yield than K^-. In addition, the small feedover also reduces the difference.

The correlated mean pion yield falls close for proton and neutron trigger, as shown in Figure 48, which indicates that the correlation can be viewed as the correlation generally with the final state baryon.

The central region for the trigger proton carries ambiguity due to the fact that it can either come from the target or from the projectile[8]. This can explain the behaviour close

[8]The contribution of pair produced protons is taken out to first order by measuring the correlation with

to the center: below x_F=0.1 of the proton, the pion yield decreases with decreasing proton x_F. If the forward proton in reality comes from the target component, the projectile baryon (which determines the forward multiplicity) can be anywhere, which on average delivers less multiplicity.

The ambiguity can be circumvented by a double trigger selection: measuring the pion multiplicity as a function of the x_F of the forward proton, requiring at the same time the presence of a backward proton. The forward trigger proton is assured to come from the projectile in this sample, even at x_F=0. The result is shown in Figure 49.

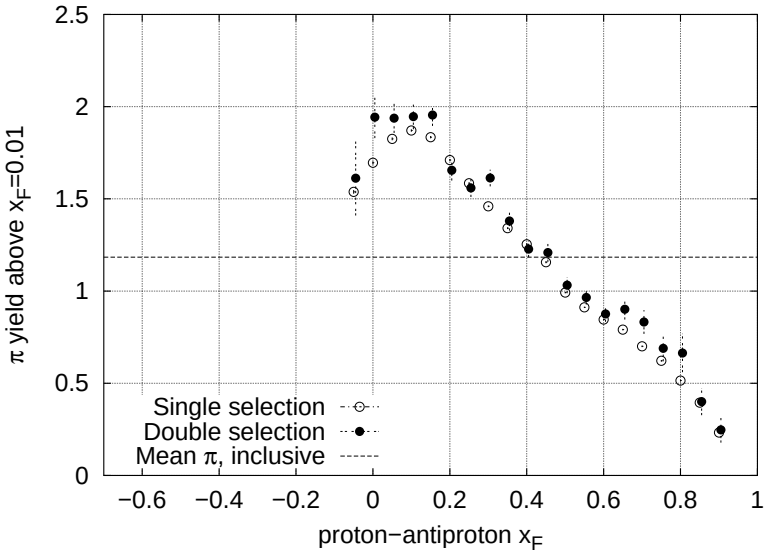

Figure 49: Selection of protons on both sides: the forward pion multiplicity is shown as a function of the x_F of the forward proton for events with a backward proton between x_F=-0.6 and -0.3.

Within the statistical errors, the curve shows a saturation effect: if the projectile proton reaches below x_F=0.1, the continuous rise of the pion yield seems to level off.

The study of the associated pion multiplicity presented above has shown that the two component picture is compatible with the results, and has revealed the fact that the pion yield is strongly correlated to the baryon number transfer. This will have direct consequences in the attempt, to join up elementary and nuclear collisions by an experimental link (see Chapter 9.8).

proton-antiproton, but this can only be done for isospin=0 combination, i.e. for mean pions, as shown in the right panel of Figure 47.

9.5 The distribution of the correlated pion yield and consequences for the baryon production mechanism

In this chapter, the details of the correlation between pions and protons will be discussed: the studies concentrate on the longitudinal distribution of the pions. Regge theory suggests, that the difference of the inclusive proton and neutron distribution in the high x_F region is due to the difference in the exchanged trajectories. The motivation of the following experimental study is the question whether protons and neutrons have differences in their production mechanism.

The correlated pion x_F distribution is shown in Figure 50. The integral increases with smaller x_F of the baryon, but the figure shows that this is to first order a parallel shift: the *slope of the distribution is closely invariant*. This effect is clearly visible for protons: up to the cutoff defined by $1 - x_F^{proton}$ the distributions are parallel. For neutrons, due to the energy smearing of the Calorimeter, the shape at high x_F is distorted such that the superposition of the correlated pion spectra with different cutoff values add up to a steeper distribution.

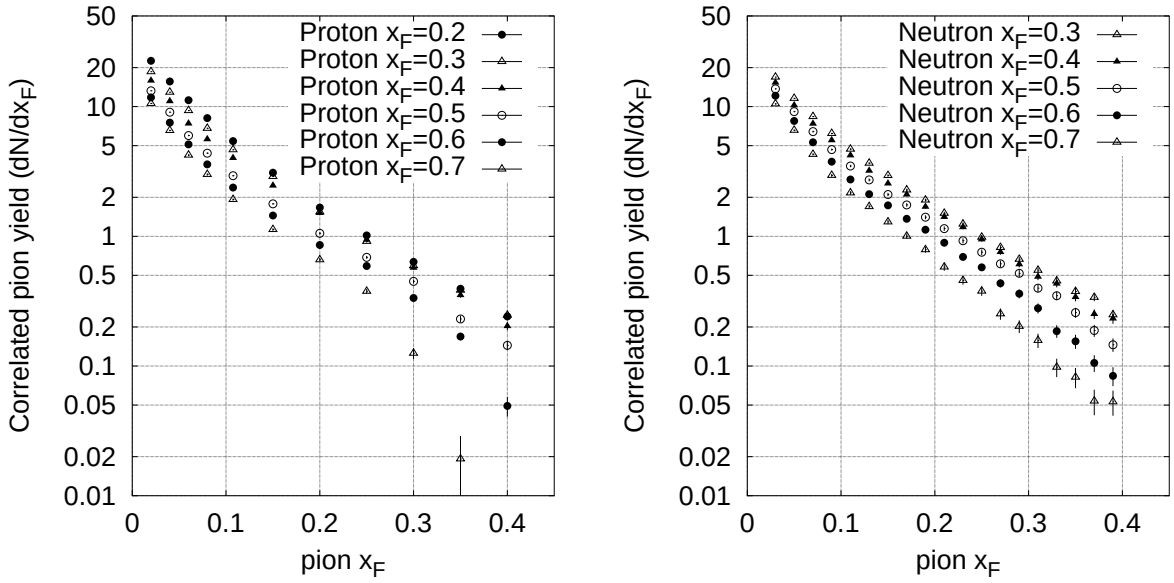

Figure 50: The shape of the pion distribution, in correlation with proton (left) or neutron (right). Note that the weak energy resolution of the Calorimeter can distort the shape in the high-x range.

Low energy measurements suggested that the primary production mechanism of neutron production is pion exchange, which was extended to high energy interactions [59]. Lately the pion exchange process is used to explain the neutron production at HERA [60]. The

"Reggeized" process is depicted in Figure 51. In the standard Regge terminology, the diffractive particle production in the pion-proton vertex is translated to the triple-Regge diagram. The calculated cross section of the process makes up for more than half of the total p+p cross section.

The reaction can be viewed as the splitting of the proton to a neutron (carrying $x_F^{neutron}$ momentum fraction) and to a pion (carrying $1 - x_F^{neutron}$ fraction). The pion subsequently undergoes a hadronic interaction with the other proton (with a total cross section of $\sigma_T^{\pi p}$). This has the consequence (as also pointed out in [61]) that the $\pi^+ + p$ *subsystem behaves similarly to an on-shell* $\pi + p$ *interaction*, i.e. the Feynman scaling will hold with the new scaling variable x_F'=x_F/(1-$x_F^{neutron}$), if the final state neutron is removed from the event.

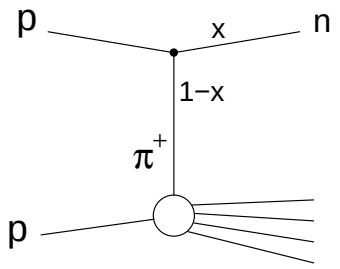

Figure 51: The pion exchange process. The pion, carrying $1 - x_F^{neutron}$ momentum fraction, interacts with the other proton.

Bubble chamber measurements [61] did not contradict this expectation, within the sizeable statistical errors. However, the result shown in Figure 52 proves that the x_F' scaling does not hold: the pion x_F' distribution changes slope with different x_F of the final state baryon.

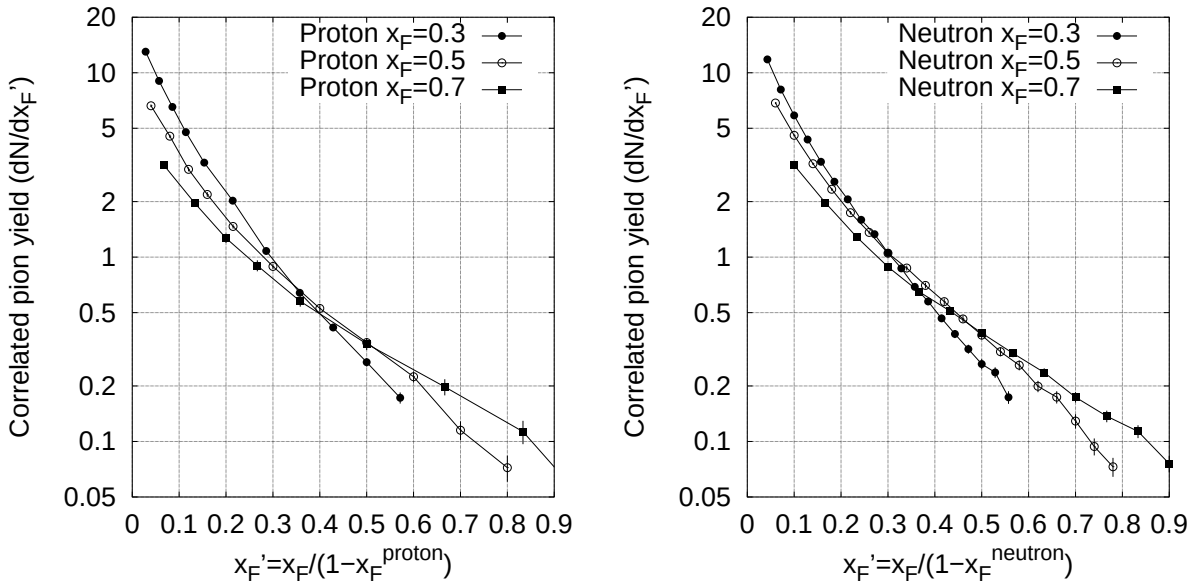

Figure 52: Non-scaling in x_F': the correlated pion yield as a function of x_F' changes slope at different x_F of the final state baryon.

The idea of x_F' scaling was studied by the ACCMOR Collaboration [62], in π^-+p

interaction. There the authors argue that the non-scaling is due to the energy dependence within the subsystem remaining after the removal the leading π^-. However, this would correspond to a very strong non-scaling of the fragmentation function. The x_F' non-scaling found by ACCMOR with pion beam is quite similar to the NA49 result in p+p.

In conclusion, the study of correlations between pions and baryons did not show any difference between proton or neutron in the final state (up to isospin effects) and therefore suggests that the production mechanism is similar. This similarity and the actual scaling behaviour disfavours the pion exchange process.

9.6 Measurement of the pion feedover

In the framework of the factorizing two component picture, the target component feeds over to the forward hemisphere. For protons, we have seen that the feedover is limited to a range of about 0.2 units in x_F (1.5 units in c.m. rapidity). In this chapter, an attempt is made to determine quantitatively the feedover for pions.

The ratio of the correlated and the inclusive (uncorrelated) pion distribution is shown in Figure 53, over the x_F range of the pion from -0.3 to 0.3, at fixed x_F of the forward proton[9].

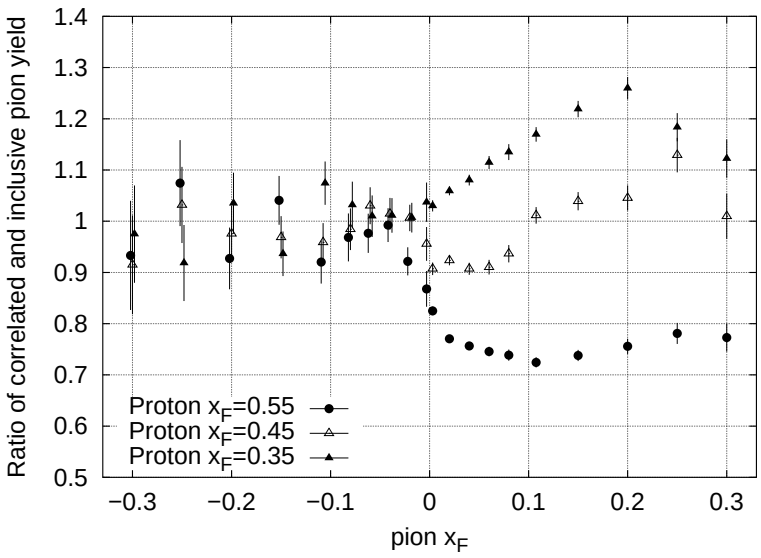

Figure 53: Mean pion distribution relative to the inclusive yield as a function of the pion x_F at different x_F bins of the trigger proton. (The data points at $x_F = 0$ and backward are a bit pulled apart for the sake of clarity.)

[9]Experimentally the forward pion yield is measured under the requirement of the presence of a forward or backward proton, but by symmetry, the distributions may be shown in the same plot as forward and backward pions correlated to a forward proton.

In the forward region, in accordance with the previous observations, the ratio increases with decreasing proton x_F. The increase is to first order a parallel shift, as it was pointed out in connection with the invariance of the slope.

In the backward region, the ratio is 1, and independent of the position of the forward proton, therefore the result is compatible with the two component picture. In the forward region, the three curves are separated, because the pion projectile component is strongly correlated to the forward proton: therefore, the pion feedover is measured by the extent of this separation in the backward region. The statistical uncertainty does not allow us to draw a precise conclusion, but from the figure it is clear, that the pion feedover is reduced already at $x_F = -0.02$, and seems to vanish completely at $x_F = -0.04$. This means, that the range of feedover for pions is more restricted in x_F than for protons.

One remark must be made concerning the experimental credibility of the result. Due to the symmetry of the collision, the correlated yield at $x_F = 0$ must be the same for backward and forward proton. This gives an experimental consistency check of the data. According to Figure 53, the consistency is fulfilled within errors. The analysis has shown, that the proper full-empty normalization and trigger loss corrections are needed to establish this symmetry.

9.7 Comparison to phenomenological models

In this section, examples of the key observations are compared to two phenomenological models, VENUS and HIJING/B$\bar{\text{B}}$.

The two-component picture was supported by the result on correlation between final state protons, presented in Figures 45 and 46. The corresponding correlation within the VENUS and HIJING/B$\bar{\text{B}}$ models are shown in Figure 54.

The VENUS model reproduces the basic features of the measurement: the ratio of the correlated and inclusive proton yield is close to 1 in the forward region; the shape of the curve does not depend on the position of the backward proton, and the actual shape is similar to that of the measurement.

The HIJING/B$\bar{\text{B}}$ predicts a strong correlation between the forward and backward proton: the correlation ratio changes by 20-30% when the backward trigger proton moves from $x_F = -0.55$ to $x_F = -0.35$. The actual measurement excludes correlations of this size[10].

The measurement of the pion feedover was presented in Figure 53. The corresponding model predictions are shown in Figure 55.

Again, the VENUS model reproduces the observations, that the backward pion yield is independent from the forward proton, and that the pion feedover (i.e. the correlated region)

[10]The correlation predicted by the original HIJING model is very similar to the picture presented here.

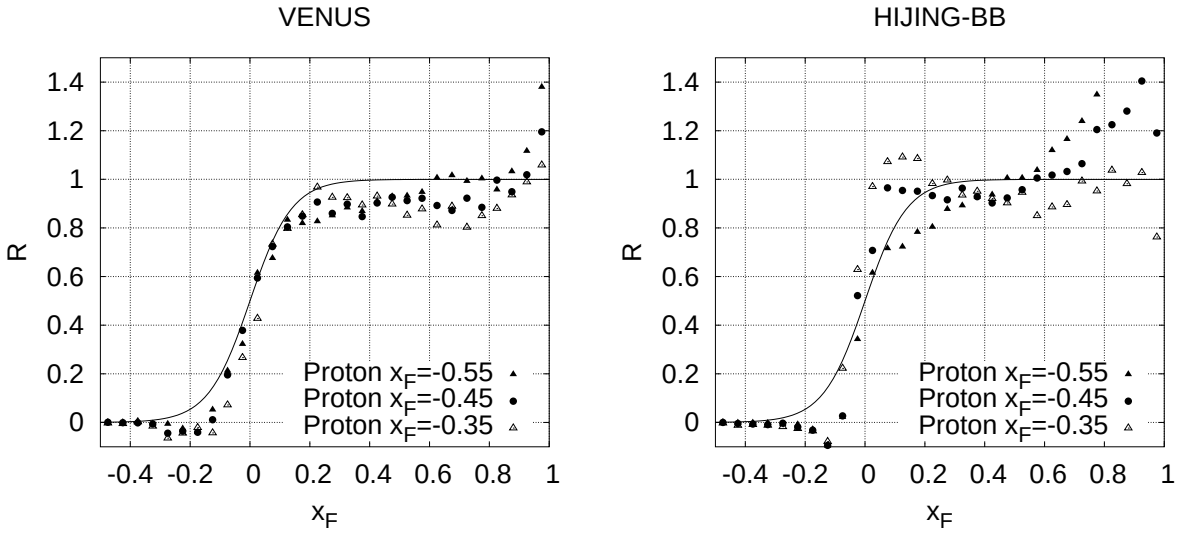

Figure 54: Correlation between two protons in the VENUS (left) and HIJING/B$\bar{\text{B}}$ (right). The trigger proton is fixed in the given backward bins. The continuous line is the curve suggested by the data in Figure 46 and 45

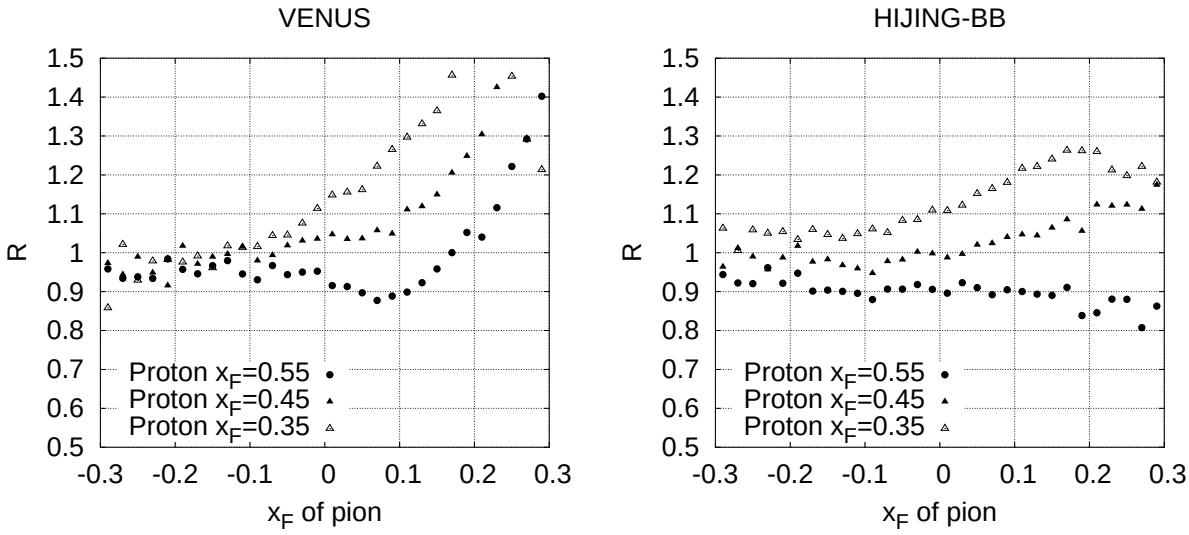

Figure 55: Correlation between pions and a trigger proton in the VENUS (left) and HIJING/B$\bar{\text{B}}$ (right). The trigger proton is fixed in the given forward bins.

extends to a limited range backwards. On the other hand, it overpredicts the correlated yield in the forward region.

The HIJING/B$\bar{\text{B}}$ predicts strong correlation between the forward proton and backward pion, which contradicts both the NA49 and ISR results.

In conclusion, the two component picture and the factorization of the two hemispheres seems to be naturally contained in the string fragmentation model VENUS. The HIJING code, which was designed to study jet production in heavy ion collisions, predicts long-range correlations between baryon-baryon and pion-baryon pairs, the presence of which is not suggested by the data.

The two examples presented above show the potential of the correlation studies to test and distinguish between phenomenological models. In the future, further detailed comparisons will be performed, also extending the scope to strange particles, transverse behaviour, baryon pair production, etc.

9.8 Predictions for nuclear collisions from correlations in elementary interactions

In this section, a model-independent way is proposed to predict the pion multiplicity in nucleus-nucleus interactions [63], based on the observation, that the centrality of the nuclear interactions, p+A and A+A, characterizes the baryon transfer. Under the assumption, that in the elementary collision the baryon number transfer is correlated to the inelasticity, the weighted superposition of the elementary collisions could be compared to A+A interactions.

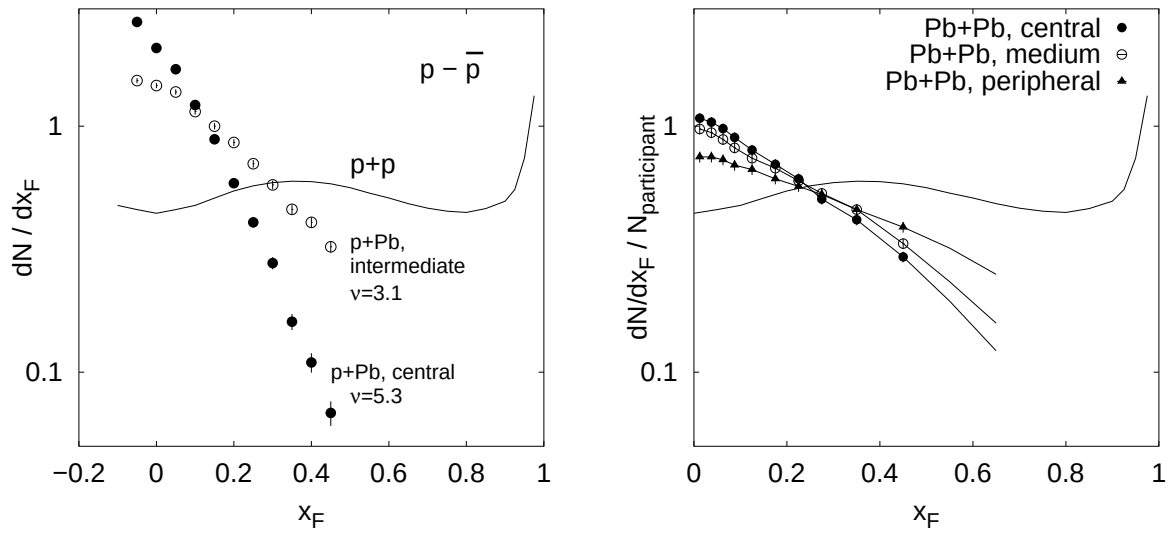

Figure 56: Net proton distribution in p+Pb and Pb+Pb: smooth evolution of baryon transfer with centrality

The net proton distributions in p+Pb and Pb+Pb [64] interactions at different centralities are shown in Figure 56, compared to net protons in p+p. The centrality of the

p+Pb collision is measured using a dedicated detector which determines the multiplicity of the knock-on protons from the nucleus. From this multiplicity, applying Glauber-model calculations and detailed detector simulation, the corresponding number of collisions (ν) is estimated. In case of Pb+Pb interactions, the measured number of spectator fragments of the projectile nucleus provides the scale of centrality. The distributions steepen up at higher centrality due to the baryon stopping phenomenon.

The baryon number transfer in nuclear collisions exhibits a smooth evolution with centrality, both in p+Pb and Pb+Pb. The larger baryon stopping characterizes higher centrality. In the elementary p+p collision there is no reliable definition of the inelasticity (the "centrality" or the effectiveness of the interaction), but on the other hand, the study of the associated pion multiplicity has shown, that the pion production increases with larger baryon transfer, which one can intuitively assign to higher inelasticity.

As a summary, based on the phenomenon of baryon stopping p+A and A+A collisions, and the strong correlation of p+p observables with the final state baryon, the following assumption can be made: *the baryon number transfer characterizes the inelasticity in p+p, p+A and A+A interactions.* This assumption provides a model-independent way to compare minimum bias p+p collisions with central A+A collisions.

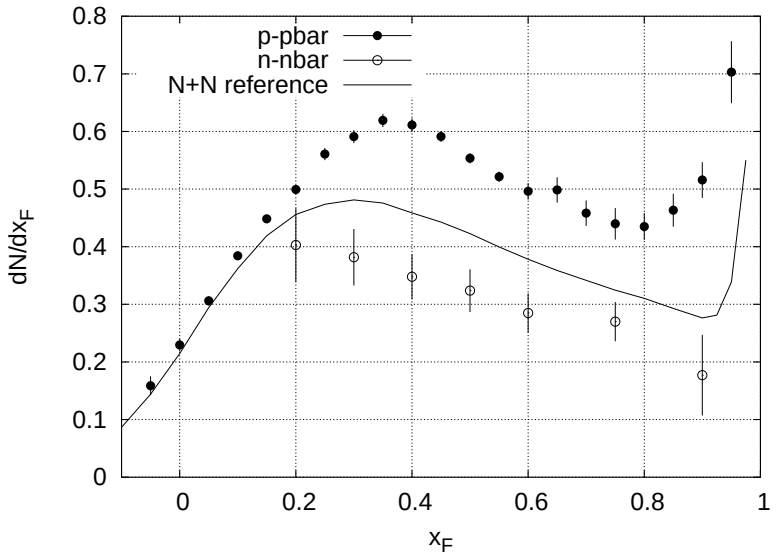

Figure 57: Net proton distribution in the reference nucleon-nucleon collision

Before formulating the prediction, the consequences of the different isospin structure of the proton and the Pb nucleus are discussed. The net proton distribution in a reference N+N collision has to be determined to take care of the neutron content of the Pb nucleus: here $N = 0.4p + 0.6n$. Within the framework of the two component picture the isospin

symmetry holds separately for the two hemispheres, therefore the net forward proton in n+p or n+n is equal to the net neutron in p+p, as it was shown in Figure 37. The net proton distribution in an isospin averaged N+N collision is shown in Fig.57. Experimentally the $x_F < 0.2$ region is not measured for neutrons; the proton measurement in n+p was used to estimate the yield in that range.

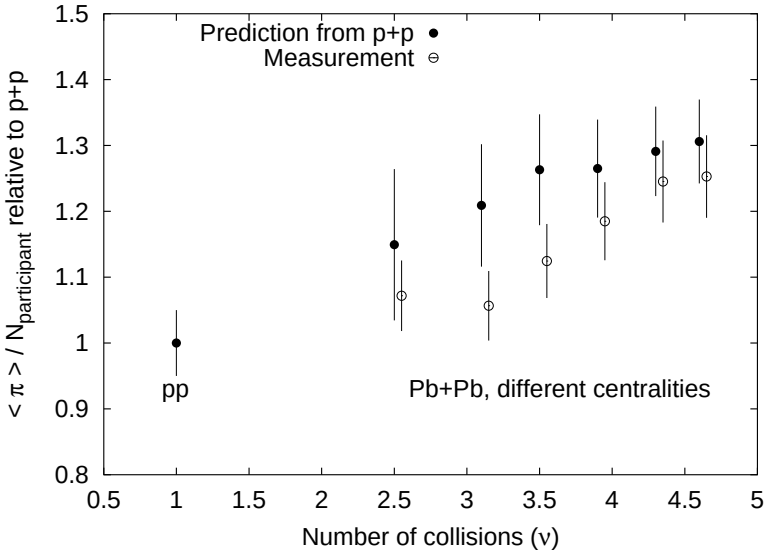

Figure 58: Comparison of the predicted and the measured pion multiplicity in Pb+Pb collisions. The prediction, which assumes that the final state baryon characterizes the inelasticity in p+p interaction gives a good qualitative agreement

In a p+p collision, any quantity, e.g. the pion multiplicity measured as a function of x_F of the final state proton (baryon) defines a correlation function $C(x)$. This correlation function was shown in Figure 49. The pion multiplicity in minimum bias p+p, by definition, can be calculated by weighing $C(x)$ with the net projectile proton distribution; this statement can be expressed in the following way:

$$< \pi >_{pp} = \frac{\int C(x) P_{pp}(x) \mathrm{d}x}{\int P_{pp}(x) \mathrm{d}}$$

where $P_{pp}(x)$ is the net projectile proton distribution in p+p as a function of x_F. In A+A, the stopped net projectile proton distribution can be viewed as protons from a superposition of p+p (or rather N+N) interactions, where events with more stopped final state protons have larger weight; this means that the pion multiplicity in A+A (per participating nucleon) is predicted to be

$$< \pi >_{PbPb} = \frac{\int C(x) P_{PbPb}(x) \mathrm{d}x}{\int P_{PbPb}(x) \mathrm{d}x}$$

In this case, the net projectile proton distribution [11] in Pb+Pb, $P_{PbPb}(x)$, is to be applied. The result of this prediction is presented in Figure 58 in comparison with pion multiplicity measurements from PbPb interactions at different centralities.

The prediction gives a good qualitative description of the measurements. If the assumptions are correct, this means that the full increase of pion multiplicity in central Pb+Pb interaction can be explained with a superposition of elementary collisions, taking proper care of the centrality selection.

One has to note, that the principal idea of weighted superposition can be applied to any quantity observed in elementary and nuclear collisions: this opens up the range of observables for which a prediction can be made. This applies e.g. to the transverse behaviour or strangeness production, both of which are considered as playing a key role in the understanding of nuclear interactions.

[11] The net projectile proton distribution in p+Pb interactions can be measured directly, by comparing π+Pb and p+Pb interactions. In Pb+Pb collisions, assumptions has to be made on the shape of the curve, with the constraint that at x_F=0, the projectile yield is half of the total yield. The questions are discussed in more detail in [63] [65].

A1. Full- and Empty-target subtraction scheme and correction for trigger loss

The basic steps of the cross section determination, as discussed in Section 7, relate the cross section to the observed event rate compared to the incoming beam rate, assuming that the interaction takes place in the target. In reality, the beam interacts with the material surrounding the target, therefore this extra rate must be subtracted. Technically this is realized by emptying the target volume and taking data with the "target empty".

The subtraction of the empty target (ET) dataset increases the statistical error, which can be improved if some fraction of events are removed, which are likely ET events. This removal, the "event cuts" may cause biases in the event sample where the interaction took place in the actual target volume ("hydrogen events"). The bias can be corrected for, but systematic errors may still remain. In the present study, the *conservative approach* is used, which minimizes the systematic errors, and aims to create *no bias due to the event cuts*.

The trigger setup of the Experiment presents a further bias to be corrected for. The "bulls eye" trigger for proton-proton interactions consists of a small scintillator disk, and the event is taken if the beam particle misses the scintillator. This latter condition is an indication that an interaction took place, but it may also be that the scintillator fires in the presence of an interaction, being hit by a produced particle, and the corresponding event is not taken. This trigger loss has to be determined and corrected.

In the first part of this Appendix, the calculation of the cross section determination is discussed in the case when the ET contribution is subtracted and the event cuts reduce the ET rate. In the following parts the reduction of the ET target is described and argued that the applied cuts are bias free. The last sections are dedicated to the correction for the trigger loss.

A1.1 Cross section measurement

The interaction cross section, as discussed in Section 7, is determined by the observed interaction rate (e.g. the occurrence of a particle in a given momentum space region) per incoming beam particles:

$$\sigma_{int} = \frac{1}{n_2 \lambda} \frac{N_{int}}{N_{beam}} = \frac{1}{n_2 \lambda} \frac{N_{trigger}}{N_{beam}} \frac{N_{int}}{N_{trigger}} = \frac{1}{n_2 \lambda} Rf \tag{6}$$

where f is yield per triggered event and R is the trigger rate. This was expressed with introducing the trigger cross section $\sigma_{trigger}$:

$$\sigma_{int} = \frac{N_{int}}{N_{trigger}}\sigma_{trigger} = f\sigma_{trigger} \tag{7}$$

The calculation of the cross section must take into account the empty target (ET) contribution. The full target (FT) dataset contains the sum of the real target (H) events and the ET events:

$$\frac{N^H_{int}}{N_{beam}} = \frac{N^{FT}_{int}}{N_{beam}} - \frac{N^{ET}_{int}}{N_{beam}}$$

or in other terms, expressed with the yields and trigger rates:

$$R^H f^H = R^{FT} f^{FT} - R^{ET} f^{ET} \tag{8}$$

The trigger cross section refers to the real target events, therefore the definition is completed by taking the ET contribution into account:

$$\sigma_{trigger} = \frac{1}{n_2\lambda}(R^{FT} - R^{ET})$$

From the above equations, the interaction cross section:

$$\sigma_{int} = \sigma_{trigger} f^H = \sigma_{trigger}\frac{f^{FT} - \epsilon f^{ET}}{1-\epsilon} \tag{9}$$

where $\epsilon = R^{ET}/R^{FT}$ is the "empty over full" rate or "ET/FT". The cross section determination therefore involves two constants: the trigger cross section and the ET/FT rate.

In the p+p data taking, the full target trigger rate is $R^{FT} = 2.9\%$, (2.9% of the incoming beam particles interact and initiate a trigger). If the target hydrogen is removed, the empty target trigger rate is $R^{ET} = 0.5\%$, so the real target rate is $R^H = R^{FT} - R^{ET} = 2.4\%$. The corresponding ET/FT rate is 18%.

The ET background is reduced by event cuts, which change the empty over full rate (ϵ). From the definition of ϵ the ET/FT rate after cuts (ϵ') can be determined:

$$\epsilon' = \frac{(N^{ET}_{trigger})'}{(N^{FT}_{trigger})'} = \epsilon\frac{(N^{ET}_{trigger})'}{N^{ET}_{trigger}} / \frac{(N^{FT}_{trigger})'}{N^{FT}_{trigger}} \tag{10}$$

where prime refers to the quantities after cuts. The equation has a simple meaning: ϵ' can be calculated from ϵ and the rejection rate in the full and empty target dataset. The value of the $\sigma_{trigger}$ does not change, because the event cuts also apply for the beam particles.

A1.2 Reduction of ET/FT rate by event cuts

Figure 59 shows two examples of the empty target contribution relative to the full target data, without any event cuts. On the left panel, the p_T distribution of positive tracks is shown for the p_Z interval of 15 to 20 GeV. The ET contribution is on the level of 13%. The right plot shows the p_Z distribution of fast, GTPC+VPC tracks for the p_T interval of 0.4 to 0.7 GeV.

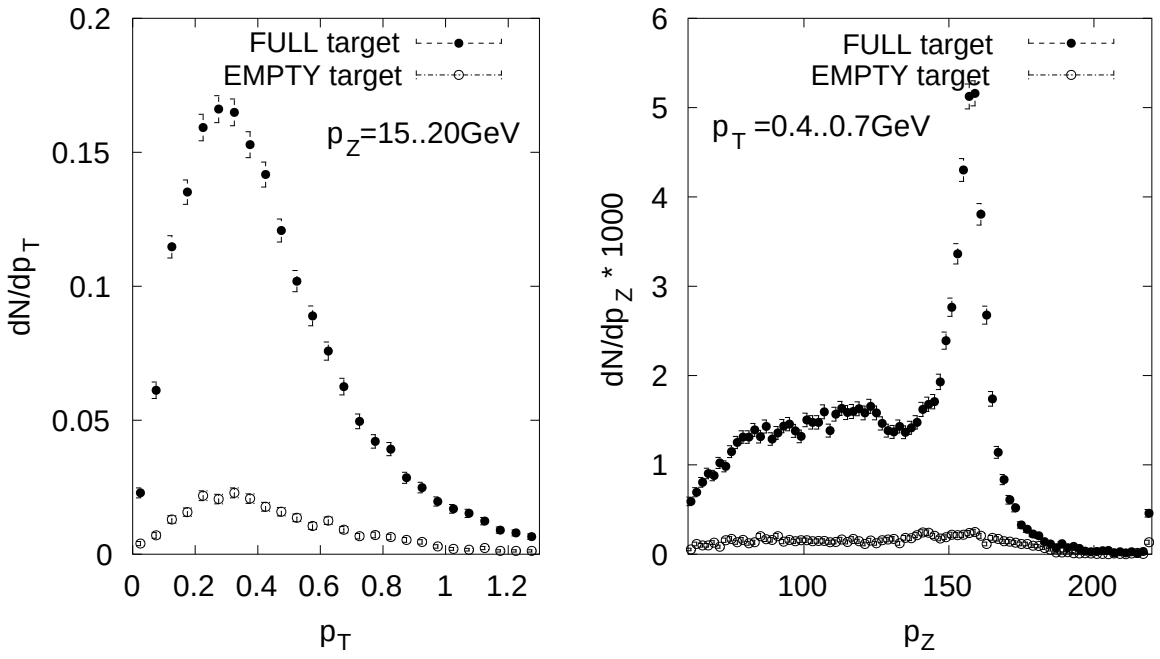

Figure 59: Full and Empty target contribution without cuts. p_T distribution of medium momentum tracks (left panel), and p_Z distribution of high momentum tracks (right panel)

As it was argued in the introduction of this chapter, the reduction of ET contribution reduces the statistical error of the final result. The reduction of the ET/FT rate was performed in two steps. First the Beam Position Detector (BPD) profile was examined. In the second stage an unbiased cut is applied on the fitted vertex z position.

The beam profile on the last BPD (BPD3) is shown in Figure 60. The horizontal profile (left panel) and the vertical profile (right panel) show both the full and empty target distributions (normalized with the ET/FT rate). The tails of the profile observed in the FT sample are due to the ET contribution, so the ET rate can be reduced by applying a cut. The "satellite" peak in the horizontal direction, caused by a special class of downstream interactions, is also rejected by this cut.

The tails appear due to far upstream interactions, producing a low-angle scattered particle traveling down the beamline (faking a beam particle) and passing by the interaction

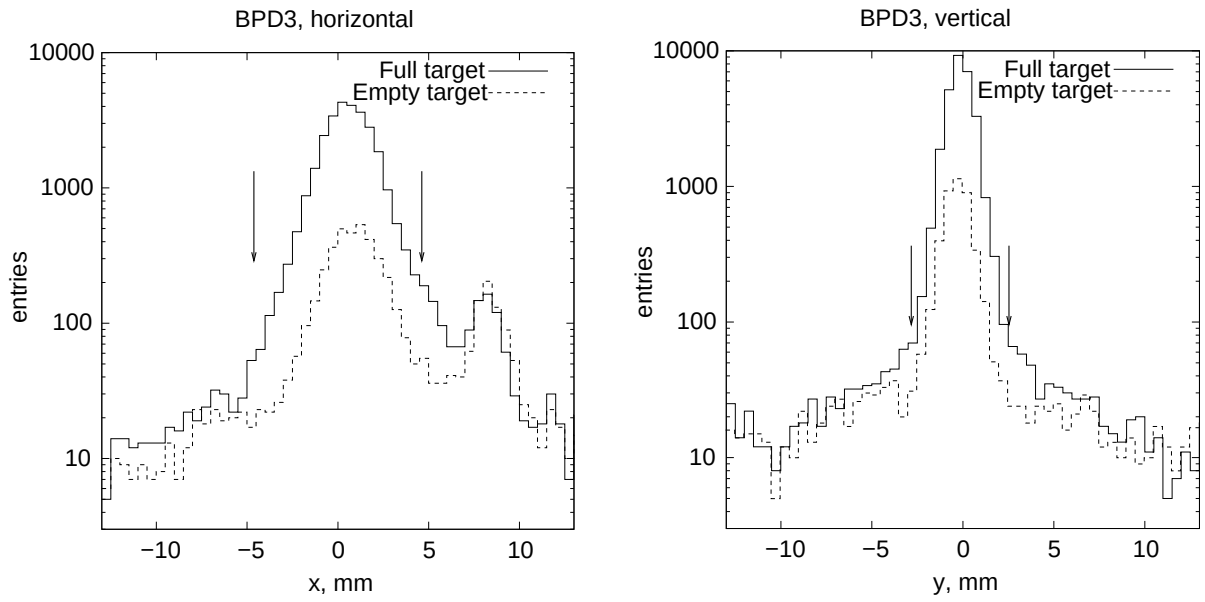

Figure 60: Beam profile on BPD3. The tails and the satellite peak in the horizontal direction is described by the empty target contribution. The cut boundaries are marked by the arrows.

trigger.

The longitudinal (Z) position of the reconstructed vertex provides a further possibility to reduce the ET contribution. However, there are two aspects that has to be taken into account:

- The precision of the vertex reconstruction depends strongly on the event topology.
- In the low multiplicity event sample, the vertex reconstruction may fail completely.

In connection with the latter question, an extensive eyescan-effort was preformed. This lead to the conclusion that most of these events are normal target events, and despite the fact that the main vertex is not reconstructed, the track reconstruction is reasonable.

The precision of the vertex determination improves at higher track multiplicities. On the other hand, the dependence on the event topology means that at the same track multiplicity, different events may have very different vertex precision, e.g. a low momentum track detected close to the vertex gives a much better definition than a fast track with a long arm of extrapolation. In order to achieve a simple classification of events, the following strategy was used: according to a certain set of criteria, tracks which give a good vertex definition ("good" tracks) are selected, and event cuts are applied depending on the multiplicity of these "good" tracks.

Tracks of good vertex determination must have reasonably many points: in the analysis, at least 15 points were required. A further important criteria is that the "good" tracks must be emitted at *nonzero elevation angle* relative to the beam, since if the elevation angle is zero, the tracks run parallel to the beam path without any intersection. The final set of criteria [66] takes into account the track direction and the vertex extrapolation length.

Depending on the multiplicity of these good tracks, a vertex cut is imposed. It is important to note, that if the vertex reconstruction failed, or if the multiplicity of the "good" tracks is zero, *no cut is applied* in order to avoid possible biases. As an example, the distribution of the Z position of the reconstructed vertex [12] for events with four good tracks is shown in Figure 61. Below Z=-650 cm and above Z=-530 cm, the FT distribution is equal to the ET contribution, so a cut placed at these Z values will eliminate some fraction of the ET without rejecting events from the target, ensuring that the cut is bias free.

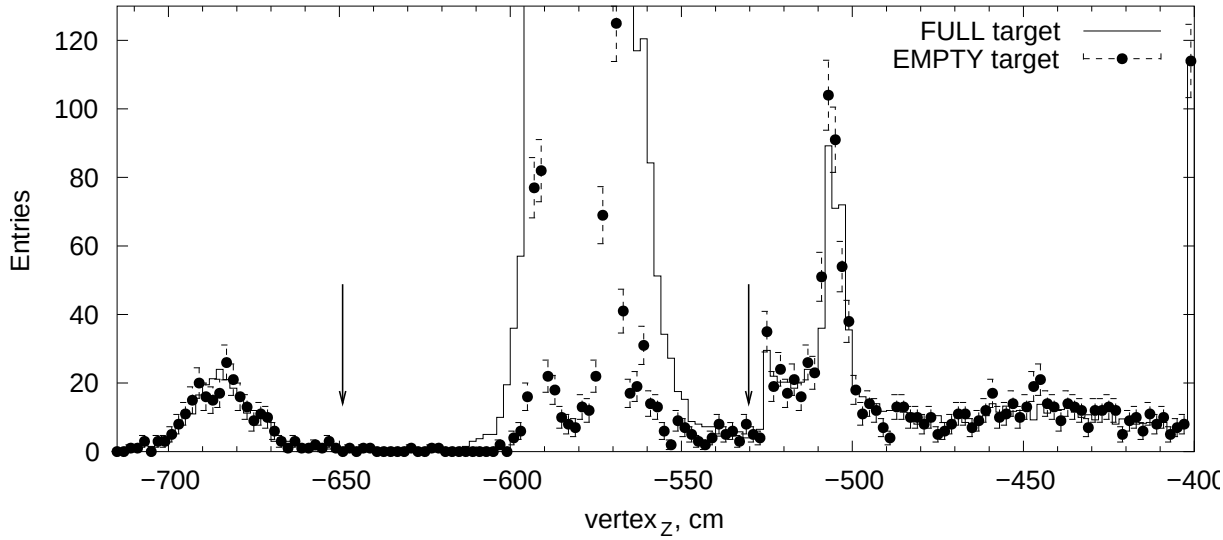

Figure 61: Vertex Z distribution for events with four "good" tracks. The arrows mark the cut boundaries.

By these cuts, the ET contribution is substantially decreased. The improvement for the two examples of Figure 59 is demonstrated in Figure 62. At low momenta, the ET contribution to the particle yield is 5% of the FT.

One can conclude, that the ET contribution is reduced to a reasonably small value for all regions of momentum space. At the same time, the event cuts are not introducing any bias, as argued in the following section.

[12]The visible structures in the empty target are the following: Z=-675: BPD-3 and target vacuum entrance; Z=-590: target holder entrance; Z=-570: target holder exit and target vacuum exit; Z=-525: TPC hut entrance; Z=-505: VTPC-1 entrance.

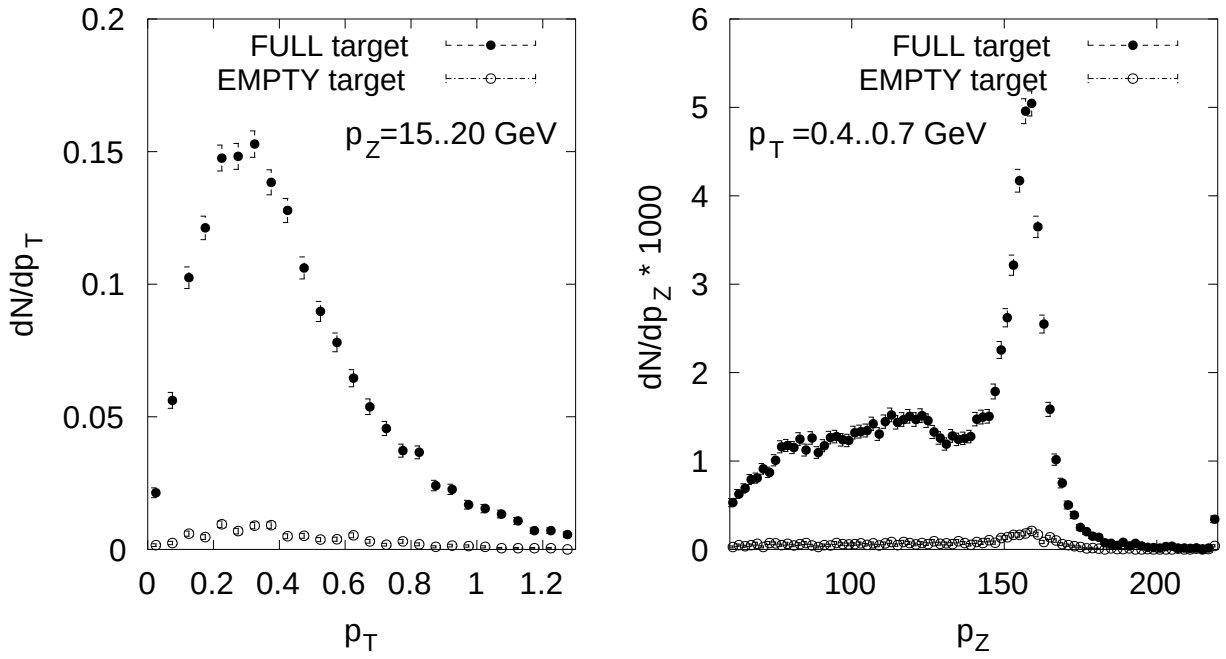

Figure 62: The same regions as in Figure 59, but with application of the BPD and vertex Z cut. The ET contribution is considerably decreased.

A1.3 Biases caused by the event cuts

The event cuts cause no bias, if they fulfill one of the requirements below:

(a) Either the rejection from the *real target interactions* ("hydrogen" events) is random: the rejection does not depend on topology, reconstruction efficiency, etc,

(b) or the cut rejects no hydrogen events at all.

The rejection of the hydrogen events by the BPD cut can only happen due to the natural spread of the beam profile, since the beam particle is detected *before* the target. The cut rejects some part of the tail. This means, that the BPD cut introduces no bias, like in case **(a)**; the only cost is a random loss in hydrogen events of about 5%.

On the other hand, the application of the vertex cut is strongly dependent on event configuration, therefore corresponding to case **(b)** the requirement of being bias free has to be studied, and the bias is to be quantified.

The accepted fraction from target only (H) events can be calculated from the accepted fraction of the FT and ET event sample:

$$\frac{(N^H)'}{N^H} = \frac{\frac{(N^{FT})'}{N^{FT}} - \epsilon\frac{(N^{ET})'}{N^{FT}}}{1-\epsilon} \tag{11}$$

here the subscript "trigger" is suppressed. The vertex Z cut is bias free, if this accepted

fraction is the same before and after the cut. The following table shows the numerical values for different run periods: p+p '99 (00D) and '00 (00R) and p+p '02 with GTPC (02G). For all the three run periods, the vertex cut is bias free within the estimated errors.

Run Period	00D	00R	02G
σ_{Trigger} (mb)	28.28	28.48	27.97
ϵ=ET/FT	0.184	0.181	0.180
ET/FT, with BPD cut	0.135	0.136	0.131
Fraction of hydrogen events (%)	94.14±0.24	95.25±0.19	91.14±0.16
ET/FT, BPD+vertex cut	0.0875	0.0881	0.084
Fraction of hydrogen events (%)	94.33±0.24	95.33±0.19	91.06±0.16

A1.4 Correction for the trigger loss

The trigger setup of the NA49 Experiment for hadron beams, as it was mentioned earlier, consists of a small scintillator counter 4 m downstream from the target. This counter (S4) is of a disk shape with 1 cm radius. Without interaction, the beam passes through the middle of the counter. The event is recorded under the trigger condition that no particle hits S4: this condition rejects the class of the interactions where a produced particle actually reaches S4. The majority of these events contain a fast, low angle scattered particle, characteristic for diffractive events.

In the calculation of the measured cross section, the cross section was expressed in terms of trigger cross section and the observed yield per event, see Eq. 6 in this chapter. The calculation implicitly involved the strong assumption, that the triggered event sample contains all occurrences of the studied interaction, i.e. there is no trigger loss. In reality, there is a loss to be corrected for.

The principle of the correction is the following: the interaction cross section can be measured as a function of the radius of S4. This is a smooth function, therefore an extrapolation to zero radius is possible. This principle is true for any cross section, also for the determination of the trigger cross section. Figure 63 shows the dependence of the trigger cross section on the radius squared of S4. The figure shows an estimate on the elastic contribution, known from previous measurements.

The trigger cross section at $r^2 = 1$ is 28.0 mb, which is far below the total p+p cross section of 38.5 mb. However, a large fraction of this cross section is elastic, which does not contribute to the particle production. According to Figure 63, the inelastic part of the trigger cross section is about 27 mb, which is 14% below the total inelastic cross section of 31.6 mb. The Figure shows the extrapolation to zero: using the measured points at $r^2 = 1$,

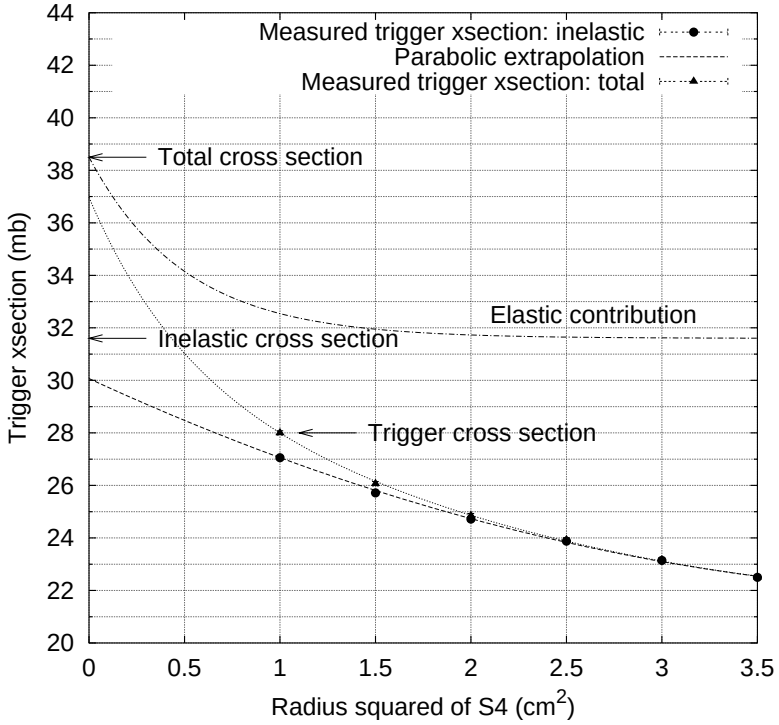

Figure 63: Trigger cross section as a function of the radius of the interaction trigger (S4). After subtracting the elastic contribution, the parabolic extrapolation is shown.

$r^2 = 2$ and $r^2 = 3$, a second order polynomial (parabolic) extrapolation is used for $r^2 = 0$. The extrapolated inelastic cross section at $r^2 = 0$ is 30 mb, about 5% below the table value, but this difference is partially due to the steep diffractive contribution (the agreement can be improved by making an estimation of the diffractive contribution).

It is important to note, that the experimental study of the cross section as a function of S4 radius is feasible only with the application of the Gap-TPC, which cleanly detects the tracks close to S4. The datasets without the GTPC can not be corrected for the trigger loss by this method.

Technically, the extrapolation procedure for every single measured cross section is very difficult: it would be desirable to simplify the procedure such that the correction is "automatically" performed for any measurement. This is feasible by the means of event weighting.

Let us assume that the interaction cross section $\sigma_{int}(r^2)$ is measured at different radii: $\sigma_{int}(1)$, $\sigma_{int}(2)$, $\sigma_{int}(3)$. From the Taylor expansion around $r^2 = 1$, the *first order*, linear approximation (suppressing the subscript "int"):

$$\sigma(0) \approx \sigma(1) + (\sigma(1) - \sigma(2))$$

The correction term $\sigma(1) - \sigma(2)$ is corresponding to the cross section from the class of

events where *there was a particle in the ring r^2=1..2 around S4.* The equation has a simple meaning: on top of the original cross section measured at r^2=1, the events where there was a particle in a ring around S4 represent a particle falling on the surface of S4.

The technical realization of the above correction is very simple: one has to take the original dataset, and the events when there was a particle in the ring has to be repeated twice to account for the correction term. In other words, this is equivalent to assigning an event weight of 2 to these events (since $\sigma(1)$ contains these events already once). The new dataset automatically contains the first order correction.

The second order correction is derived similarly, from the Taylor expansion of $\sigma(r^2)$ around r^2=2:

$$\sigma(0) \approx \sigma(1) + 2\,(\sigma(1) - \sigma(2)) - (\sigma(2) - \sigma(3))$$

Again, the implementation is simple: the correction term contains the contribution from the ring of r^2=1..2 and r^2=2..3 around S4. Taking these events with the weights of 3 and 0 correspondingly, the correction is realized automatically for the new dataset.

The event weighting means that all the particles in the event are weighted up, and at the same time, the event number is counted with taking the weight into account. This means that the trigger cross section of the weighted dataset has to be increased accordingly to account for the increased event number. It is interesting to note that the full-empty subtraction can also be translated to event weighting (taking empty target events with the weight of -1), so one can arrive to a single dataset which includes the full-empty subtraction and the correction for trigger loss. Further details of the procedure are discussed in [67].

The calculated correction for protons is shown in Figure 64. In the forward region the correction is small: if the fast track is detected in the experiment, it must have missed S4; then the loss can be due to a slow track hitting S4, and this process has a low probability. On the other hand, in the backward region, the correction reaches 14%, which is in direct connection to the two-component picture of baryon production: the backward proton can be associated to a fast forward proton, which has a high chance to hit S4. The correction restores the forward-backward symmetry, which is an important experimental cross-check of the results. The correction amounts to about 5% at midrapidity for protons.

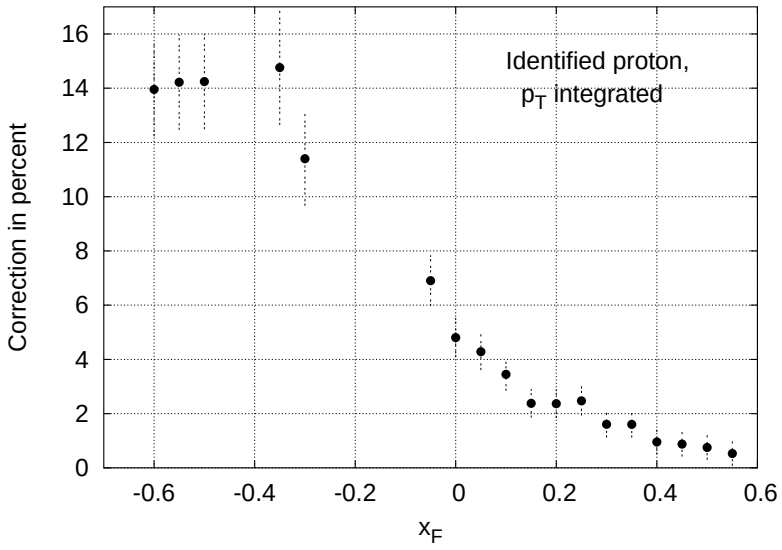

Figure 64: Trigger loss correction for protons in p+p interactions.

A2. Event mixing method in correlation studies

Inclusive particle yields possess the basic symmetry of rotations around the beam axis, or in other words, the inclusive cross section is independent of the azimuthal angle ϕ. The measurement of the yield can therefore be performed with a detector of incomplete acceptance. The situation is more complicated in the case of correlations (or double-differential cross sections). Here the symmetry corresponds only to the simultaneous rotation of both particles around the beam axis, and the cross section has a dependence on the difference of the azimuthal angles, $\Delta\phi$. This has two important experimental consequences. On one hand, there may be acceptance holes in $\Delta\phi$, even in those ranges where the inclusive yield of both particles can be measured. On the other hand, the detection efficiency, which is in this case dominated by dE/dx cut loss, may depend on $\Delta\phi$. To circumvent these problems, *assumptions has to be made* to describe the correlated yield, even if one wants to integrate over some of the kinematic variables (e.g. $\Delta\phi$, p_T). In fact, the problem is rather technical: due to the high number of kinematical variables (five instead of the two in the inclusive channel) the binning of the dataset becomes impossible.

The inclusive (non-invariant) differential particle density ρ_A for particle A depends on two of the kinematical variables, which may be chosen as x_F^A and p_T^A, and independent of the azimuthal angle ϕ^A. The double-differential density ρ_{AB} has five variables, x_F^A, p_T^A, x_F^B, p_T^B and $\Delta\phi = \phi^A - \phi^B$. In the following discussion, particle A will be referred to as trigger particle, B as the correlated particle.

The trigger particle defines a direction in the p_x,p_y plane; let us rotate the p_x^B, p_y^B components of the correlated particle transverse momentum such, that the rotated components, t^B and u^B follow this direction: t^B points in the direction of the trigger particle (see Figure 65). The (t^B,u^B,ϕ^A) parameter set is equivalent to (p_T^B,ϕ^B,ϕ^A) set and can be freely transformed to each other; similarly, (t^B,u^B) is equivalent to (p_T^B,$\Delta\phi$).

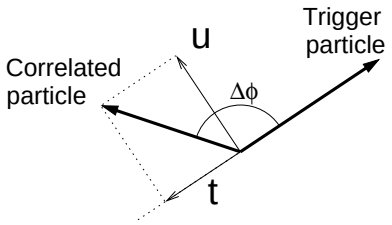

Figure 65: Definition of t^B and u^B: rotated components of p_T^B.

The transverse momentum of the trigger particle has to be balanced by the transverse momentum of the correlated (and also all the other) particles, due to momentum conservation in the transverse directions. One can make the *assumption*, that the distribution of the correlated particle in the (t^B, u^B) plane shifts against the trigger particle, in the direction of t^B, by the amount of T. Besides the transverse shift, the yield of the correlated particle can change relative to the inclusive yield. This change is the analogy of the correlation ratio introduced in Section 9. The transverse momentum of the correlated particle is $(p_T^B)^2 = (t^B)^2 + (u^B)^2$, therefore if the distribution is shifted by T, this corresponds to changing $(p_T^B)^2$ to $(t^B - T)^2 + (u^B)^2$.

The assumption for the correlated distribution can be formulated in the following way:

$$\rho_{AB}(x_F^A, p_T^A, x_F^B, t^B, u^B) = R\rho_A(x_F^A, p_T^A)\rho_B(x_F^B, \sqrt{(t^B - T)^2 + (u^B)^2}) \qquad (12)$$

where $\rho_B(x_F^B, p_T^B)$ is the inclusive distribution of the correlated particle, $\rho_A(x_F^A, p_T^A)$ is the inclusive distribution of the trigger particle and R and T are arbitrary function of (x_F^A, p_T^A, x_F^B).

Technically what we gained is that the five variables of the correlated density reduced to three variables in two functions. The question is now how to measure the value of these functions. In the following discussions, the longitudinal variables (x_F^A, x_F^B) will be suppressed.

Experimentally one counts the number of particle pairs in the given kinematical region; this corresponds to the double-inclusive density, folded with the detection probability (efficiency). The detection efficiency (ϵ) is a function of all the three (x_F,p_T,ϕ) kinematical variables of both particles. ϵ can be viewed as a product of the acceptance, which is 0 or 1, depending on whether the particle is detected or not; and the efficiency of the particle selection (dE/dx cut). The differential counting rate for a pair of particles in a bin of x_F^A, x_F^B, p_T^A, p_T^B, ϕ^A, ϕ^B is:

$$\rho_{AB}(p_T^A, p_T^B, \Delta\phi)\epsilon^A(p_T^A, \phi^A)\epsilon^B(p_T^B, \phi^B)$$

The above formula shows the experimental difficulty: the number of detected pairs depends separately on ϕ^A and ϕ^B and not only on the difference as does the correlated density. To simplify the following calculation, the efficiency factor will be denoted by $\mathcal{E} = \epsilon^A(p_T^A, \phi^A)\epsilon^B(p_T^B, \phi^B)$, but one has to keep in mind that it depends on all the kinematical variables of both particles.

The event mixing technique offers an elegant treatment of the problem. One can take the trigger particle from one event and the correlated particle from an other, therefore the counting rate becomes:

$$\rho_A(p_T^A)\rho_B(p_T^B)\mathcal{E}$$

where instead of the double-inclusive density, the product of the single-inclusive densities appear. This way, comparing to the previous expression, the efficiency will fall out from the ratio, and one does not have to determine that numerically.

Let us apply this in practice. In the normal data sample, one can make bins in p_T^A and t^B (and also in x_F^A and x_F^B), and count the particle pairs in these bins. This corresponds to integrating over ϕ^A and u^B:

$$\int \mathrm{d}\phi^A \mathrm{d}u^B \rho_{AB}(p_T^A, t^B, u^B)\mathcal{E} \equiv I_0(p_T^A, t^B) \tag{13}$$

At this point, one can exploit the assumption formulated in Eq. 12. The Taylor expansion of ρ_B in its second argument (p_T^B) reads:

$$\rho_B(\sqrt{(t^B - T)^2 + (u^B)^2}) = \rho_B(p_T^B) + T\frac{\partial \rho_B}{\partial p_T^B}\frac{t^B}{p_T^B}$$

which can be substituted to Eq. 12; then from the left hand side of 13 one obtains:

$$R\int \mathrm{d}\phi^A \mathrm{d}u^B \rho_A(p_T^A)\rho_B(p_T^B)\mathcal{E} + RT\int \mathrm{d}\phi^A \mathrm{d}u^B \rho_A(p_T^A)\rho_B(p_T^B)\mathcal{E}\left(\frac{1}{\rho_B(p_T^B)}\frac{\partial \rho_B}{\partial p_T^B}\frac{t^B}{p_T^B}\right) \equiv$$

$$\equiv RI_1(p_T^A, t^B) + RTI_2(p_T^A, t^B) \tag{14}$$

The formula appears to be difficult at first look, but the integrals I_1 and I_2 can be calculated in a very simple way by event mixing. Similarly to I_0, I_1 is the counting rate in the given bin of p_T^A and t^B, but now in the mixed sample: the trigger and the correlated particle are taken from two different events. I_2 is a bit more complicated, but in the event

mixing scheme, one has to apply a *weight* on each particle pair, corresponding to the last bracketed term in the formula. The derivative of ρ_B can be calculated numerically.

According to Eq. 13 and 14, I_0 is a linear combination of I_1 and I_2, therefore R and T can be obtained obtained by a fit:

$$\frac{I_0(p_T^A, t^B)}{I_1(p_T^A, t^B)} = R + RT\frac{I_2(p_T^A, t^B)}{I_1(p_T^A, t^B)} \tag{15}$$

One has to note, that R and T does not depend on t^B. This means, that one can check if the original assumption is right, by observing if the t^B dependence of the two sides are the same. The left panel of Figure 66 shows the t_B dependence of the left and right side of Eq. 15: with proton trigger at $x_F^A = 0.25$, p_T^A=0.5 GeV, for correlated π^- at $x_F^B = 0.06$.

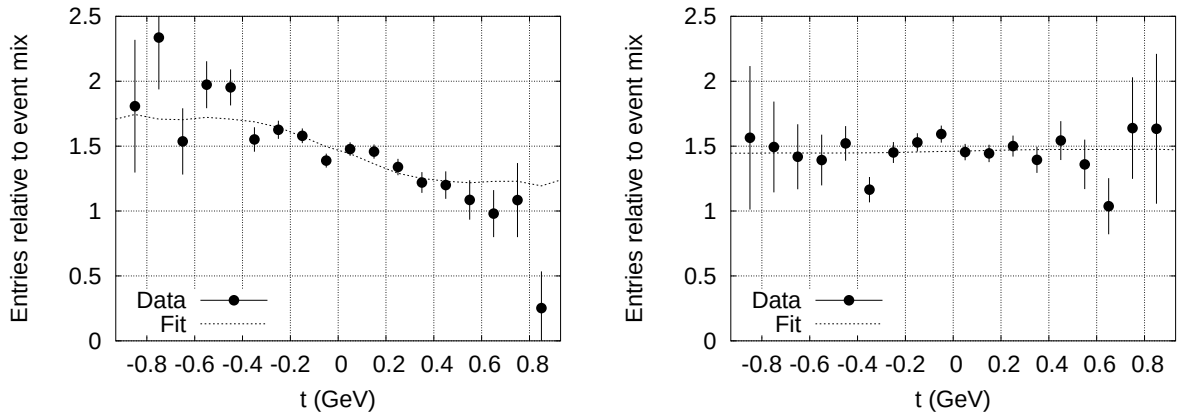

Figure 66: Examples of the t^B dependence of Eq. 15 (left panel). If one replaces t by u, no u dependence can be observed within errors (right panel).

The Figure shows that the left side of Eq. 15 ("Data" on the plot) can be approximated by the right side ("Fit"). (If the original assumption (Eq. 12) would be unreasonable, that would reflect in e.g. the curving down of the correlated data at both ends of the t scale).

The whole analysis can be repeated such that one replaces t by u; then, after integration over t, the u dependence can be studied. The u dependence must be symmetric; at the same time, the original assumption predicts that in the equation analogous to Eq. 15, *there is no u-dependence:* the left hand side must be constant, and the second term of the right side vanishes. This is an other test of the assumption formulated in Eq. 12, shown in the right panel of Figure 66.

The average of R over p_T^A can be calculated, to restrict its variables to x_F^A and x_F^B. In Section 9., this averaged quantity is given as the correlation ratio. The T quantity was not studied within the framework of the present thesis, but it opens up the way towards the

investigation the correlated transverse behaviour and the balance in the transverse direction in hadronic collisions.

A general concluding remark fits at this place, concerning the discussion above. The presented studies has shown, that the final results has weak dependence on the actual assumptions, for the reasons that the detector acceptance is large and that the "irregular" correlations (e.g. $\Delta\phi$ dependence) are relatively small. In fact, the simplest assumption, which could be that the shape of the double-inclusive distribution is factorizing ($\rho_{AB} = R\rho_A\rho_B$ and R would depend only on x_F^A and x_F^B) still gives similar results, and the physics conclusions that one can draw are the same. I still consider the above presented study to be important, since it provided a way to quantify the uncertainties and to show that they are small.

Acknowledgments

I would like to thank my Supervisor, György Vesztergombi for the opportunity that I could participate in an international collaboration, and had the chance to join the communities of our University and the Research Institute in Budapest.

I would like to express my gratitude to Hans Gerhard Fischer, for his continuous scientific and moral support. As the leader of the NA49 Proton Group, he was initiator of the hadron beam program at NA49. He introduced me into the field of experimental high energy physics, taught me the intricacies of detector construction and operation, and made me understand what serious physics analysis means.

I am thankful to my Colleagues from Hungary, Dániel Barna, Zoltán Fodor, Ferenc Siklér and Gábor Veres, for their honest criticism and patience. I directly profited from the discussions with Ferenc who had the infallible intuition to avoid the traps of physics analysis. I am very grateful for Gábor's conscientious comments, all through the previous years and also concerning the present thesis. Dániel's sense for the beauties of Nature was the driving force of our mountain trips which ensured our physical fitness for the pleasures of science. The cheerful company of the three of them made my CERN visits always joyful. Zoltán helped me to solve quickly and effectively all the technical problems I presented to him, could those be connected to hardware or software.

I am grateful to all the other members of the proton group, Helena Bialkowska, Kreso Kadija, Sigfried Wenig, Ondrej Chvála, Michal Kreps, Andrzej Rybicki and Tatjana Šusa, for their devoted work for the success of our physics program, and especially to Latchezar Betev for maintaining key parts of our Experiment, software system and computer hardware. I am thankful to the spokesman of NA49, Peter Seyboth, and to all the other members of the Experiment.

I would like to thank Péter Lévai for his inestimable help and valuable advises at the realization of this thesis.

I enjoyed the hospitality of the Department of Atomic Physics, under the leadership of Prof. Ádám Kiss and Prof. András Patkós to whom I am very grateful. My friends at the Department, Szabolcs Borsányi and Zsolt Szép provided me with immediate assistance whenever I deserved.

Finally I wish to thank my family, especially my grandmother for their love, encouragement and understanding through all these years at the University.

My work was partially supported by the Hungarian Scientific Research Foundation (T032648, T14920, T32293 and F034707) and the Doctorate School of the Eötvös Loránd University.

Bibliography

[1] V. Blobel et al. *Multiplicities, topological cross-sections and single particle inclusive distributions from p p interactions at 12-GeV/c and 24-GeV/c. Nucl.Phys.* **B69** *454. (1974)*

[2] J. Whitmore et al. *Experimental results on strong interactions in the NAL bubble chamber. Phys.Rept.* **10** *273. (1974)*

[3] V.V. Ammosov et al. *A study of pi+, pi- and proton production in pp interactions at 69 GeV/c. Nuo.Cim.* **40A** *273. (1977).*

[4] G. Giacomelli, M. Jacob *Physics at the CERN ISR. Phys.Rept.* **55** *1-132 (1979)*

[5] M. Aguilar-Benitez et al. *Inclusive particle production in 400-GeV/c p p interactions. Z.Phys.* **C50** *405. (1991)*

[6] David Horn and Fredrik Zachariasen *Hadron physics at very high energies. W. A. Benjamin, Advanced Book Program, Series: Frontiers in physics (1973)*

[7] K. Fialkowski, W. Kittel *Parton models of low momentum transfer processes. Rept.Prog.Phys.* **46** *1283 (1983)*

[8] A. Capella, U. Sukhatme, C-I Tan, J. Tran Thanh Van *Dual Parton Model. Phys.Rept.* **236** *225-329 (1994)*

[9] K. Werner *Strings, pomerons, and the VENUS model of Hadronic interactions at ultrarelativistic energies. Phys.Rept.* **232** *87-299 (1993)*

[10] Xin-Nian Wang, Miklos Gyulassy *A systematic study of particle production in p+p (anti-p) collisions via the HIJING model. Phys.Rev.* **D45** *844-856 (1992)*

[11] D. Kharzeev *Can gluons trace baryon number? Phys.Lett.* **B378** *238-246 (1996)*

[12] D.S. Barton et al. *Experimental Study of the A-dependence of Inclusive Hadron Fragmentation. Phys.Rev.* **D27** *2580. (1983)*

[13] W. Busza and R. Ledoux *Energy deposition in high-energy proton nucleus collisions. Ann.Rev.Nucl.Part.Sci.* **38** *119 (1988)*

[14] Z. Fodor, S.D. Katz *Lattice Determination of the critical point of QCD at finite T and Mu. JHEP* **0203** *014 (2002)*

[15] S.A. Bass, M. Gyulassy, H. Stocker, W. Greiner *Signatures of quark gluon plasma formation in high-energy heavy ion collisions: a critical review. J.Phys.* **G25** *R1-R57 (1999)*

[16] M. Gyulassy, I. Vitev, X. Wang, B. Zhang *Jet quenching and radiative energy loss in dense nuclear matter. Quark Gluon Plasma 3, editors: R.C. Hwa and X.N. Wang e-Print Archive:* **nucl-th/0302077**

[17] P. Lévai et al. *Discovery of jet quenching at RHIC and the opacity of the produced gluon plasma. Nucl.Phys.* **A698** *631-634 (2002)*

[18] S. Afanasev et al. *The NA49 large acceptance detector. Nucl. Instr. Meth.* **A430** *210. (1999)*

[19] F. Siklér *Centrality control of hadron nucleus interactions by detection of slow nucleons. e-Print Archive:* **hep-ph/0304065.**

[20] D. Varga *Beam request: d+p datataking in 2002 using online spectator trigger. NA49 Collaboration Meeting, CERN, Oct. 2001.*

[21] F. Siklér *Részecskekorrelációk vizsgálata nagyenergiás nehézion-ütközésekben. PhD. Thesis. ELTE, Budapest. In Hungarian.*

[22] G. Pálla et al. *The Grid-Geometry Time-Of-Flight Detector Used In The Na49 Experiment At The Cern SPS. Nucl.Instrum.Meth.* **A451** *406. (2000)*

[23] C. De Marzo et al. *A Segmented Photon - Hadron Calorimeter Using A Two Colored Wavelength Shifter Optical Readout System. NIM***217** *405. (1983)*

[24] V. Eckardt et al. *A Novel Light Collection System For Segmented Scintillation Counter Calorimeters. Nucl.Instrum.Meth.* **155** *389. (1978)*

[25] C. De Marzo et al. *A Study Of Deep Inelastic Hadron - Hadron Collisions With A Large Acceptance Calorimeter Trigger. Phys.Lett.* **B112** *173. (1982)*

[26] S. Margetis et al. *Transverse energy production in Pb-208 + Pb collisions at 158-GeV per nucleon. Phys.Rev.Lett.* **75** *3814. (1995)*

[27] G.I. Veres *Baryon momentum transfer in Hadronic and Nuclear Collisions at the CERN NA49 Experiment. PhD. Thesis.*

[28] Thomas Sammer *Produktion von K*- und Phi-Mesonen in pp- und PbPb-Reaktionen am CERN SPS. PhD. Thesis. In German.*

[29] F. Siklér *Particle Identification Using dE/dx and its Application for Physics. NA49 Internal Note.*

[30] J. Bracinik *The status of inclusive cross section and particle ratios in p-p and p-pPb. NA49 Collaboration meeting, CERN, Sept. 1998*

[31] M. De Palma et al. *Measurement, Parametrization And Fast Simulation Of Hadronic Showers In Lead. NIM* **219** *87. (1984)*

[32] V. Blobel et al. *Inclusive Neutron And Lambda Production In Proton Proton Interactions At 12-Gev/C And 24-Gev/C. Nucl.Phys.* **B135** *379. (1978)*

[33] K. Jaeger et al. *Characteristics Of V0 And Gamma Production In P P Interactions At 205-Gev/C. Phys.Rev.* **D11** *2405. (1975)*

[34] D. Barna *Strange Particle Production in Proton-Proton Collisions at 158 GeV. PhD. Thesis.*

[35] H. Kichimi et al. *Inclusive Study Of Strange Particle Production In P P Interactions At 405-Gev/C. Phys.Rev.* **D20** *37. (1979)*

[36] B.Y. Oh and G.A. Smith. *Inclusive Study Of Lambda0 And Sigma+- Hyperons Produced In Proton Proton Collisions From 6.6 To 28 Gev/C. Nucl.Phys.* **B49** *13. (1972)*

[37] T. Okusawa et al. *Study Of Baryon Production And Its Features In 405-Gev/C Proton Proton Interactions. Europhys.Lett.* **5** *509. (1988)*

[38] M. Kreps *Feeddown correction for protons and antiprotons. NA49 Internal Note.*

[39] O. Chvála *Corrections due to vertex resolution. NA49 Internal Note.*

[40] R.P. Feynman *Very High-Energy Collisions Of Hadrons. Phys.Rev.Lett.* **23** *1415. (1969)*

[41] J. Whitmore et al. *Invariant cross-section for the inclusive reaction p+p–>p+X at 205-GeV/c. Phys. Rev.* **D11** *3124 (1975)*

[42] J.W. Chapman et al. *The Diffractive Component In P P Collisions At 102-Gev And 405-Gev. Phys.Rev.Lett.* **32** *257. (1974)*

[43] A.E. Brenner et al. *Experimental Study Of Single Particle Inclusive Hadron Scattering And Associated Multiplicities. Phys.Rev.* **D26** *1497. (1982)*

[44] J.R. Johnson et al. *Inclusive Charged Hadron Production In 100-Gev To 400-Gev P P Collisions. Phys.Rev.* **D17** *1292. (1978)*

[45] M.G. Albrow et al. *Inelastic Diffractive Scattering At The CERN ISR. Nucl.Phys.* **B108** *1. (1976)*

[46] J.C. Armitage et al. *Diffraction Dissociation In Proton Proton Collisions At Isr Energies. Nucl.Phys.* **B194** *365. (1982)*

[47] M. Bozzo et al. *Single diffraction dissociation at the CERN SPS Collider. Phys.Lett.***136B** *217 (1984)*

[48] M.R. Whalley et al. *Inclusive Neutron Production. In *Kyoto 1979, Proceedings, 16th International Cosmic Ray Conference, Vol.6*, 34-39. (1979)*

[49] J. Engler et al. *Measurement Of Inclusive Neutron Spectra At The ISR. Nucl.Phys.***B84***70. (1975)*

[50] W. Flauger and F. Monnig *Measurement Of Inclusive Zero - Angle Neutron Spectra At The ISR. Nucl.Phys.* **B109** *347. (1976)*

[51] H. G. Fischer et al. *Baryon number transfer and central net baryon density in elementary hadronic interactions. Acta Phys.Polon.* **B33** *1473. (2002)*

[52] D. Varga *Proton spectator selection in 160 GeV deuteron-proton collisions and related technical studies. NA49 Internal Note. (2001)*

[53] D. Barna et al. *Strange particle production in nuclear collisions at CERN-NA49. Proceedings of 37th Rencontres de Moriond, Les Arcs, France, 9-16 Mar 2002. e-Print Archive:* **hep-ex/0205042**

[54] M. Kreps et al. *Baryon and anti-baryon production in hadron-hadron and hadron-nucleus interactions. Nucl.Phys.* **A715** *502. (2003)*

[55] K. Goulianos *Diffractive Interactions of Hadrons at High Energies. Phys.Rep.* **101** *169. (1983)*

[56] I.V. Azhinenko et al. *Strange and Nonstrange Baryon Production in pi+ p and k+ p Interactions at 250-GeV/c. Z.Phys.* **C44** *573. (1989)*

[57] G.J. Bobbink et al. *Correlations between high momentum secondaries in p p collisions at S**(1/2) = 44.7 GeV and 62.3 GeV. Nucl. Phys.* **B204** *173 (1982)*

[58] H. Boeggild et al. *Some examples of associated charged particle multiplicities in proton-proton collisions at 19 GeV/c. Nucl.Phys.* **B72** *221 (1974)*

[59] M. Bishari *Pion Exchange And Inclusive Spectra. Phys.Lett.* **B38** *510. (1972)*

[60] S. Chekanov et al. *Leading neutron production in e+ p collisions at HERA. Nucl.Phys.* **B637** *3. (2002)*

[61] Y. Eisenberg et al. *Production Of Slow Protons In The Inclusive Reactions P (Pi+) N → P (Slow) X At 195-Gev/C. Nucl.Phys.* **B135** *189. (1978)*

[62] F. Pauss et al. *Forward Particle Production In Pi- P And K- P Collisions At 58-Gev/C And Comparison With Quark Models. Z.Phys.* **C27** *211. (1985)*

[63] D. Varga et al. *Baryon number transfer in hadron+nucleus and nucleus+nucleus collisions: a link between elementary and complex interactions. APH NS. Heavy Ion Phys.* **17** *387. (2003)*

[64] F. Siklér et al. *Hadron Production in Nuclear Collisions from the NA49 Experiment at 158 AGeV/C. Nucl.Phys.* **A661** *45. (1999)*

[65] A. Rybicki *Charged Hadron Production in Elementary and Nuclear Collisions at 158 GeV/c. PhD Thesis. IFJ Krakow, Poland. (2002) CERN Library Record:* **CERN-THESIS-2003-005**

[66] D. Varga *Cross Section Determination Using Full and Empty Target Data Subtraction. NA49 Internal Note. (2003)*

[67] D. Varga *S4 Size Correction. NA49 Internal Note. (2003)*

Összefoglaló

A dolgozat az elemi lágy hadronikus ütközések kísérleti vizsgálatával foglalkozik. Ezeket a folyamatokat az erős kölcsönhatás elmélete, a QCD elvben helyesen írja le; ennek ellenére az elmélet szerkezete miatt az elemi ütközések leírására nem léteznek számolások. A lágy hadronikus fizika napjainkban legdinamikusabban fejlődő ága a nehézion-fizika, ami egy QCD-beli fázisátalakulás nyomait keresi nagy energiás atommag-atommag ütközésekben.

A dolgozatnak két fő motivációja van. Az elemi kölcsönhatások vizsgálatát egyrészt az teszi szükségessé, hogy összehasonlítási alapot adjanak a mag-mag ütközésekben várt jelenségekhez. Másrészt, részecskeelolszlások pontos és nagy kinematikai tartományt lefedő méréseivel valamint ezen túlmenően korrelációs vizsgálatokkal a fenomenologikus részecskekeletkezési mechanizmusok az eddigieknél szélesebb körben tesztelhetővé válnak.

A dolgozatban az NA49 detektorrendszerének rövid bemutatása után részletesen tárgyalom az általam kifejlesztett és alkalmazott módszereket, melyek lehetővé teszik azonosított töltött részecskék és neutronok eloszlásainak mérését. Kitérek egy új építésű, részecskepályák rögzítésére szolgáló detektor adatainak fizikai analízisére, a neutronok mérésére szolgáló detektor kalibrációjára és adatkiértékelésére valamint az eredmények normalizálásának új módszerére.

A dolgozatban bemutatott eredmények két részre tagolódnak: részecskeeloszlások valamint részecskék közötti korrelációk vizsgálatára.

Proton-proton kölcsönhatásban meghatároztam a protonok keltési hatáskeresztmetszetét közel a teljes kinematikai tartományban, szemben a korábbi mérések limitált akceptanciájával. Az eredményeket részletesen összehasonlítottam korábbi mérésekkel. Meghatároztam a neutronok eloszlását; ez utóbbi mérés azért fontos, mert a korábbi eredmények ellentmondásosak voltak. Megmutattam, hogy a barionszám megmaradás kísérletileg teljesül, ami bizonyítja az új eredmények konzisztenciáját. Összehasonlítottam pion-proton és proton-proton ütközésekben a végállapoti protonok eloszlását, amiből arra következtettem, hogy a barionszám-eloszlás két faktorizálódó komponensre bontható: egyik a céltárgyhoz, másik a nyalábrészecskéhez kötődik.

Ez utóbbi kérdést megvizsgáltam a részecskekorrelációk szempontjából is, amiből az derült ki, hogy a két komponens statisztikusan független egymástól. Meghatároztam a pionok és a végállapoti barionok közötti korrelációt. A mérések alapján javaslatot tettem elemi és nukleáris kölcsönhatások összehasonlítására, melyben a nukleáris kölcsönhatások centralitásának analógiáját a végállapoti barion lelassulása jelenti elemi ütközésekben. A jóslat, mely a nukleáris kölcsönhatást elemi kölcsönhatások súlyozott szuperpozíciójával közelíti, helyesen adja a pionok számának mért növekedését Pb+Pb kölcsönhatásban.

Summary

The thesis presents an experimental study of elementary soft hadronic interactions. These processes are in principle described by QCD, the theory of strong interactions, but due to the special structure of the theory, calculations can not be performed for the description of elementary collisions. Unlike other branches of soft hadronic physics, heavy ion physics has been strongly evolving over the past decades, motivated by the search for a QCD phase transition in high energy nucleus-nucleus collisions.

The presented thesis has two main motivations. On one hand, the study of elementary interactions is necessary for the reason that they can provide the basis of comparison with the observations in heavy ion collisions. On the other hand, precise inclusive measurements over large kinematical range, and correlation studies going beyond the inclusive level offer the possibility of testing the current phenomenological descriptions over a wide range of observables.

After a brief description of the NA49 detector setup, the experimental methods are presented allowing the measurement of identified charged and neutral particle distributions, developed by the Author. The construction of a new additional imaging chamber is discussed, along with a detailed description of the physics analysis. The calibration and data reduction process of the neutron detector, and a new normalization method is presented.

The results are arranged in two sections: inclusive distributions and correlation studies.

The cross section of proton production in proton-proton interaction is measured, covering closely the complete kinematical range in contrast to the limited acceptance of previous measurements. The measured neutron distribution is presented; these results are important for the reason that the existing previous measurements are contradictory. The total yield of baryons are shown to fulfill the baryon number conservation, which proves the experimental consistency of the results. The comparison of the net proton distribution in pion-proton and proton-proton collisions leads to a factorizing two component picture of baryon number transfer: one of the components is connected to the projectile, the other to the target.

This latter question is studied from the point of view of correlations. These studies have shown that the components are statistically independent. The correlation between the produced pions and the final state baryon is presented. Based on the observations, a prediction for particle yields in heavy ion collisions is proposed, where the stopping of the final state baryon in elementary collisions measures the inelasticity of the interaction, on the analogy of the centrality in nuclear collisions. The prediction, which approaches the nuclear collisions by a weighted superposition of elementary interactions, gives a good description of the increase of pion yield in Pb+Pb interaction.